The Search for Evidence of Supersymmetry in Trilepton Final States at the LHC

Christina Jane Potter

Department of Physics

Royal Holloway, University of London

A thesis submitted to the University of London for the Degree of Doctor of Philosophy

February 2009

Declaration

I confirm that the work presented in this thesis is my own. Where information has been derived from other sources, I confirm that this has been indicated in the document.

Christina Jane Potter

Abstract

The potential of the ATLAS detector to discover trilepton final state signatures from decays of supersymmetric particles at the LHC is investigated. An inclusive and an exclusive trilepton search have been conducted for a range of different mSUGRA scenarios, in the focus point region, in the bulk region, and at the edge of the current experimental limits on SUSY. The inclusive trilepton plus high transverse momentum jet final state is found to be a clean, simple and robust signature, with a discovery potential of between a few hundred inverse picobarns to a few inverse femtobarns of data, depending on the SUSY scenario considered. The inclusive trilepton channel has the potential to be an excellent candidate for an early physics programme at the LHC. In contrast, an analysis strategy has also been developed for the hadronically quiet trilepton channel from direct gaugino production. Optimised for the focus point region, the exclusive selection relies on stringent lepton track isolation and also includes cuts on variables such as transverse missing energy and on the hadronic activity in the event. This exclusive trilepton channel could yield a discovery with a few tens of inverse femtobarns of data if strongly interacting sparticles are not produced abundantly at the LHC. Studies have been conducted into the expected performance of the ATLAS detector and trigger, in addition to possible data-driven methods to estimate the Standard Model backgrounds to the trilepton signal.

Acknowledgements

First and foremost, I wish to express my deepest gratitude to my supervisor, Dr Antonella De Santo, for her invaluable support, guidance, encouragement and patience throughout my PhD. Thank you for nurturing the researcher in me and making me the scientist I am today.

I would like to thank the Science and Technology Facilities Council (STFC) for their generous financial support during this degree. I am also very grateful to Royal Holloway and the Institute of Physics (IOP) for providing funding for several essential conference trips.

The work presented in this thesis could not have been realised without the help of the Royal Holloway Particle Physics Group and the ATLAS Collaboration, in particular the ATLAS SUSY Working Group. I thank all my colleagues at CERN and at Royal Holloway for their friendship and inspiration. Special thanks must go to Ellie Dobson, Jasna Dragic, Michele Faucci Giannelli, Mike Flowerdew and Sudan Paramesvaran for all the helpful technical discussions.

I am also very grateful to my family and friends, who have had a great influence over me and have helped me fully realise my ambitions. Finally, I would like to thank David for all his sacrifices and for making me so happy.

To my David.

Contents

List of Figures

List of Tables

Chapter 1

Theory and Motivation

Particle physics is the quest to understand the building blocks of the universe and their interactions. The Standard Model is a theoretical framework that explains many of the currently existing observations of fundamental particles and the forces between them. However, the Standard Model is certainly not the last word in particle physics, as it can be seen as only effective at low energy scales and leaves many questions unanswered. Theoretical extensions to the Standard Model, such as Supersymmetry, may provide answers to the problems left unanswered and establish a more complete description of our universe.

1.1 The Standard Model

The Standard Model (SM) [1], [2] has been tremendously successful in describing particles and their interactions. Originally developed in the early 1970's, it has been experimentally probed to very high precision and has made many successful predictions. The SM invokes quantum field theory [3] (where particles are treated as fields) to describe the electromagnetic, weak and strong forces, however, the gravitational force is yet to be incorporated. The elementary particles are divided into two main types according to their spin: fermions (half-integer spin) and bosons (integer spin). Fermionic SM particles are the matter particles, discussed in Section 1.1.1, whilst the bosonic SM particles are the force carrying particles and are presented in Section 1.1.2. The postulated particle associated with the mass generation mechanism, the Higgs boson, is discussed separately in Section 1.1.3.

Generation	1 2 3	Charge	Mass
Leptons	$\begin{pmatrix} e \\ \nu_e \end{pmatrix}, \begin{pmatrix} \mu \\ \nu_\mu \end{pmatrix}, \begin{pmatrix} \tau \\ \nu_\tau \end{pmatrix}$	-1 0	0.511 MeV, 105.7 MeV, 1.78 GeV ~ 0
Quarks	$\begin{pmatrix} u \\ d \end{pmatrix}, \begin{pmatrix} c \\ s \end{pmatrix}, \begin{pmatrix} t \\ b \end{pmatrix}$	$+\frac{2}{3}$ $-\frac{1}{3}$	1.5-3.3 MeV, 1.27 GeV, 171.2 GeV 3.5-6.0 MeV, 104 MeV, 4.2 GeV

Table 1.1: The SM matter particles with their electric charges and masses. Numbers from [4].

1.1.1 Matter

The particles that constitute matter are the spin-$\frac{1}{2}$ particles of the SM. The matter particles are divided into two types; those that interact via the strong, weak and electromagnetic forces, known as quarks, and those that only interact electromagnetically and/or weakly, known as leptons. In total there are six known leptons and six known quarks, which are organised into three generations, where a pattern of increasing masses is seen across generations. The SM matter particles and their properties are shown in Table 1.1. Only the first generation of quarks and leptons are stable and make up ordinary matter. In quantum field theory, the quarks and leptons are treated as massless fermion fields which shall be referred to as ϕ.

Leptons

Leptons interact via the electromagnetic and weak forces, but not via the strong force. The three types of charged lepton are the electron, the muon and the tau, which are all massive. The three types of electrically neutral leptons, called neutrinos, are assumed to be massless, however, recent evidence of neutrino mixing has shown them to have a non-zero mass [5] [6] [7]. For each charged lepton there is an anti-lepton with the same mass but opposite charge. For each neutrino there is an anti-neutrino with opposite chirality (“handedness”).

Quarks

The six types of quark are the up, down, charm, strange, top and bottom, which may interact via the strong, weak and electromagnetic forces. Quarks are fractionally charged and carry an additional quantum number known as “colour”. The colour of a quark may be “red”, “green” or “blue”, or, in the case of oppositely charged anti-quarks, “anti-red”, “anti-green” or “anti-blue”. In nature, quarks are confined to colourless bound states known as “hadrons” (e.g. protons and neutrons), and it is quark colour that allows such states as $\Delta^{++}(uuu)$ to exist without violating the Pauli Exclusion Principle.

Force	Particle	Charge	Mass
Strong	g	0	0
Electromagnetic	γ	0	0
Weak	$W^{\pm}$ Z	±1 0	80.4 GeV 91.2 GeV

Table 1.2: The SM force carrier particles with their electric charges and masses. Numbers from [4].

1.1.2 Forces

The SM describes the electromagnetic, weak and strong forces as the exchange of spin-1 vector bosons, known as "force carriers", between the fermions. The force carrier particles and their properties are shown in Table 1.2. Each force is described by a gauge theory, which is invariant under local transformations. Quantum chromodynamics (QCD) describes strong interactions as the exchange of neutral, coloured particles called gluons. The electromagnetic force is described by quantum electrodynamics (QED), where the force carriers are electrically neutral photons and the weak force is described by the exchange of massive Z and $W^{\pm}$ bosons. The electromagnetic and weak force are described by one unified gauge theory, known as the "electroweak" theory. It is expected that at very high energies ($\sim 10^{16}$ GeV) the strong and electroweak forces are unified into one force, which may be described by a Grand Unified Theory (GUT).

QCD

QCD describes the strong interaction, which is limited to the colour carrying particles in the SM, the six quarks, their antiparticles and the gluon. QCD is the invariance of fermion fields under the $SU(3)_C$ non-Abelian symmetry group (not all the group elements commute), and gives rise to eight massless gluons (due to the 8-dimensional representation of $SU(3)_C$). The conserved quantity of $SU(3)_C$ is colour and the non-Abelian nature of $SU(3)_C$ allows for self-interaction terms in QCD, i.e. gluons may couple to themselves. Neither free quarks nor gluons have been observed directly, leading to the idea of colour "confinement" and QCD provides the mechanism for the binding of quarks into colourless hadrons.

QED

QED is the gauge theory describing the electromagnetic force, which is the interaction between charged fermions and the massless photon. The invariance of fermion fields under $U(1)_Q$ transformations gives rise to a massless exchange boson, the photon, and electric charge Q is the conserved quantity in QED. The Abelian nature of $U(1)_Q$ does not allow any self-interaction terms for photons.

Weak

Massless fermion fields have both left and right-handed components $\phi = \phi_L + \phi_R$ and weak interactions are limited to only the left-handed components of the fermion fields. Since neutrinos experience only the weak interaction, it is assumed that they do not have right-handed components. In treating left-handed and right-handed particles differently, the weak interaction violates parity.

The weak interaction can be described by the invariance of fermion fields under $SU(2)_L$ transformations (the subscript L for left-handed fermion interactions), where the conserved quantity is the third component of weak isospin I_3 (analogous to charge in QED). This gives rise to three gauge bosons, the neutral Z boson that is exchanged in neutral current weak interactions and the charged $W^{\pm}$ bosons that are exchanged in charged current weak interactions. The charged current weak interaction is the only force capable of changing charged leptons into neutrinos and changing quark flavour. Since $SU(2)_L$ is an non-Abelian symmetry group, self-interaction terms arise that allow the weak gauge bosons to couple to each other.

Electroweak

The Electroweak (EW) theory [8], [9], [10] is a unified gauge theory of the electromagnetic and weak forces for energies above $\sim$100 GeV. The EW gauge theory is the invariance of fermion fields under $SU(2)_L \times U(1)_Y$ transformations, where weak and electromagnetic interactions are described by both the $SU(2)_L$ group and the $U(1)_Y$ group (as opposed to $U(1)_Q$ describing only electromagnetic interactions in QED). The conserved quantity of $SU(2)_L$ is the third component of weak isospin I_3 and the conserved quantity of $U(1)_Y$ is hypercharge Y (where $Q = Y + I_3$). The $SU(2)_L$ symmetry group is non-Abelian, thus self-interaction terms are possible for the weak gauge bosons, however, because $U(1)_Y$ is an Abelian group, self couplings for the electromagnetic force carriers are forbidden.

The $SU(2)_L$ symmetry group results in three massless gauge bosons $W_\mu^{1,2,3}$ and the $U(1)_Y$ symmetry group gives rise to just one massless gauge boson B_μ. It is the mixing between these four massless bosons that gives rise to the photon field A_μ via

$$A_\mu = \sin\theta_w W_\mu^3 + \cos\theta_w B_\mu\,, \tag{1.1}$$

the Z boson field Z_μ via

$$Z_\mu = \cos\theta_w W_\mu^3 - \sin\theta_w B_\mu\,, \tag{1.2}$$

and the charged $W^\pm$ boson fields via

$$W_\mu^\pm = \frac{W_\mu^1 \mp iW_\mu^2}{\sqrt{2}}\,, \tag{1.3}$$

where θ_w is the weak mixing angle.

It is important to mention here the idea of quark mixing in the weak sector, which was invoked to allow quark-lepton symmetry. In the SM, the weak interaction quark eigenstates d', s', b' are actually superpositions of the mass eigenstates d, s, b. The mixing of the down-type quark eigenstates affects the strength of the flavour changing weak couplings and is described by the CKM matrix [11]. Weak interaction couplings between same generation quarks are larger than for quarks differing by one generation, and are referred to as Cabibbo favoured weak interactions and Cabibbo suppressed weak interactions respectively. The weak coupling between quarks that differ by two generations is even smaller yet (doubly Cabibbo suppressed). In this manner, the weak coupling between u and d quarks is larger for than u and s quarks, resulting in the decay rate for $\pi^+(u\bar{d}) \rightarrow \mu^+\bar{\nu}_\mu$ to be much larger than the decay rate for $K^+(u\bar{s}) \rightarrow \mu^+\bar{\nu}_\mu$. Recent evidence suggests similar mixing for the three neutrinos, where the neutrino mass eigenstates mix close to maximally [5]. One important consequence of neutrino mixing is that the neutrinos must have finite mass.

At this point, the SM can be described by the invariance of massless fermion fields under $SU(3)_C \times SU(2)_L \times U(1)_Y$ transformations and all the gauge bosons responsible for mediating the forces are also massless. This is not a problem for the gluon and photon, which mediate long range forces and must be massless. However, it is known from precision experiments that three of the gauge bosons, the W^+, W^- and Z have mass, as do the charged leptons and quarks (massive fermions are forbidden under $SU(2)_L$ symmetry). For this to happen, electroweak symmetry must be broken.

1.1.3 Electroweak Symmetry Breaking

In order to give mass to the weak gauge bosons in the SM, electroweak symmetry must be broken from $SU(2)_L \times U(1)_Y$ to $U(1)_Q$. Inserting mass terms into the SM Lagrangian (the function that contains the dynamics of a system) by hand breaks the gauge invariance of the theory, leads to divergences and thus, a non-renormalisable theory. Renormalisation is the recovery of finite quantities (particle masses, coupling constants etc) in a perturbation theory of any order. One approach that offers a solution is the Higgs mechanism [12].

The Higgs Mechanism

The Higgs mechanism allows for a renormalisable theory of electroweak symmetry breaking by the introduction of a scalar field, known as the Higgs field. Unlike other fields, the Vacuum Expectation Value (VEV) of the Higgs field is non-zero. The VEV of the Higgs field is not invariant under gauge transformations and so "spontaneously" breaks the gauge symmetry. The spontaneous electroweak symmetry breaking from the Higgs mechanism results in mass terms in the SM Lagrangian for the $W^{\pm}$ and Z weak gauge bosons and the leptons and quarks. The photon picks up no such mass terms in the Lagrangian and so remains massless.

A massive neutral scalar (spin-0) boson that is self-interacting, the Higgs boson, is predicted as a direct result of the Higgs mechanism. The weak gauge bosons and fermions acquire mass by interacting with the Higgs field, and the mass generated is proportional to the strength of their coupling with the Higgs. Unfortunately, the Higgs mechanism does not allow a direct theoretical calculation of the masses of the Higgs boson, weak gauge bosons or the fermions, due to unknown coupling constants. However, it does predict the ratio of the W and Z boson masses to be $\cos\theta_w$, which has been experimentally verified.

The Higgs mechanism describes the origin of mass in the SM, but the Higgs boson has yet to be discovered. Constraints may be made on the mass of the Higgs boson using both unitarity constraints and experimental results. Unitarity constraints from $W^+W^- \rightarrow W^+W^-$ scattering place an upper limit on the Higgs mass of ~ 1 TeV [13]. Direct searches for the Higgs boson at LEP place a lower limit of 114.4 GeV at 95 % CL [14] and precision fits from electroweak data give an upper limit of 219 GeV at 95 % CL [15]. Recent searches at the Tevatron have excluded a Higgs boson of mass 170 GeV with 95 % CL [16]. These limits suggest that if the Higgs boson does exist, it should be found at the LHC.

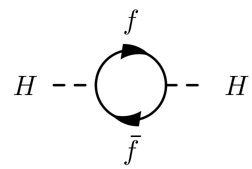

Figure 1.1: Feynman diagram of a fermion loop correction to the SM Higgs mass.

The Hierarchy Problem

The Higgs boson will be subject to large radiative corrections to its mass from loop interactions with fermions and bosons. Such a fermion loop correction is shown in in Figure 1.1, which will yield a correction to the square of the Higgs mass of

$$\delta m_H^2 = \frac{\lambda_f^2}{16\pi^2}\left[-2\Lambda^2 + 6m_f^2 \ln\left(\frac{\Lambda}{m_f}\right)...\right], \tag{1.4}$$

where m_H is the Higgs boson mass; m_f is the fermion mass; λ_f is the coupling between the Higgs boson and the fermion; and Λ is the energy cut-off scale of the theory. If the SM is assumed to be correct for energies up to the Planck scale then $\Lambda \sim \Lambda_{PL} \sim 10^{19}$ GeV, resulting in undesirable quadratic divergences in the corrections to the Higgs mass.

Since evidence suggests a light Higgs boson with a mass on the order of a few hundred GeV, a high level of fine-tuning would need to be introduced to compensate for the quadratic divergences in the Higgs mass, making the theory rather unattractive. This is known as the “hierarchy problem” in the SM. Large corrections to the Higgs mass may be be avoided by setting $\Lambda \sim 1$ TeV, suggesting that the SM is only an effective field theory that is valid below a certain energy and new physics should appear at energies above ~ 1 TeV.

1.2 Supersymmetry

Supersymmetry (SUSY) [17], [18] is a Grand Unified Theory (GUT) that appears to successfully unify the strong, weak and electromagnetic forces at high energies. There are many known symmetries in nature and, as seen earlier in this chapter, symmetry considerations dominate modern fundamental physics. SUSY proposes a new symmetry between fermions and bosons in an attempt to reconcile the Standard Model, GUTs and experimental observations to form a complete set of symmetries. In SUSY, every SM fermion should have a bosonic super-partner of the same

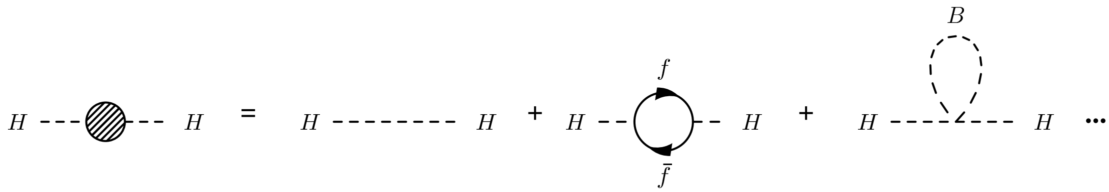

Figure 1.2: Feynman diagrams depicting the contributions to the Higgs mass from the bare Higgs and the fermion and boson loops.

mass and every SM boson should have a fermion super-partner of the same mass.

1.2.1 Theoretical Motivation

SUSY can provide an answer to some of the problems associated with the SM, in particular, the hierarchy problem and the unification of the forces.

A Solution to the Hierarchy Problem

It was seen in Section 1.1.3 that quadratic divergences in the Higgs mass from loop corrections leads to the hierarchy problem, which is one of the most critical shortcomings of the SM. When both fermion and boson loop corrections to the Higgs mass are considered, as shown in Figure 1.2, the Higgs mass can be written in terms of its bare mass, plus loop corrections from fermions, plus loop corrections from bosons as

$$m_H^2 = m_0^2 + \frac{\lambda_f^2}{16\pi^2}\left[-2\Lambda^2 + 6m_f^2 \ln\left(\frac{\Lambda}{m_f}\right)...\right] + \frac{\lambda_B}{16\pi^2}\left[\Lambda^2 - 2m_B^2 \ln\left(\frac{\Lambda}{m_B}\right)...\right] \;...\;, \quad (1.5)$$

where m_H is the Higgs boson mass; m_0 is the Higgs boson bare mass; m_f is the fermion mass; m_B is the boson mass; λ_f is the coupling between the Higgs boson and the fermion; λ_B is the coupling between the Higgs boson and the boson; and Λ is the energy cut-off scale of the theory.

If SUSY particles (also known as "sparticles") exist, they will add more contributions to Equation 1.5, where one extra bosonic contribution will be added for every SM fermion degree of freedom and one extra fermion contribution for each boson degree of freedom in the SM. In this way, two bosonic contributions will be added for each fermion contribution. Since the sign of the Λ^2 term is opposite for fermion and boson contributions, then the quadratic divergences of the Standard Model corrections to the Higgs mass are naturally cancelled if $\lambda_f^2 = \lambda_B$. More importantly, these cancellations will occur for any energy cut-off scale. The logarithmic divergences in the corrections to the Higgs boson mass still remain, but only a relatively small amount

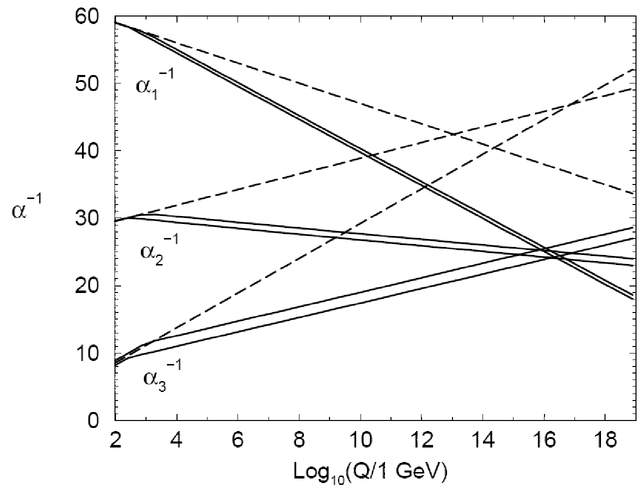

Figure 1.3: The running of the inverse gauge couplings with increasing interaction energy scale for the SM ($SU(3)_C \times SU(2)_L \times U(1)_Y$), where $\alpha_1, \alpha_3, \alpha_3$ are the gauge couplings for hypercharge, the weak force and QCD, respectively. The dashed lines show the SM prediction alone, while the solid bands show the SM prediction with the inclusion of SUSY. The widths of the SUSY bands reflect experimental uncertainties (from [18]).

of fine-tuning is required to remove them. In this manner, SUSY provides a natural and elegant solution to the SM hierarchy problem by preventing the Higgs boson obtaining an immense mass.

Unification of the Forces

It is assumed that the SM is a low energy approximation of a higher energy theory (a GUT). Thus, the SM must be embedded in a higher order symmetry, which is spontaneously broken at a high energy scale. At this scale, the gauge couplings of the SM are expected to unify. Figure 1.3 shows the running of the gauge couplings with increasing energy scale of interactions and it is seen that when the SM is considered alone, the couplings become similar at high energies, but do not precisely unify. SUSY predicts a spectrum of new particles at high energies, the presence of which will affect the running of the gauge couplings. This effect is to bring the gauge couplings into unification at energies $\sim 10^{16}$ GeV. The unification energy is very important as it indicates the cut-off energy of the GUT.

1.2.2 The MSSM

The Minimal Supersymmetric Standard Model (MSSM) is the supersymmetric extension of the SM with the addition of a minimal number of particles. A symmetry between fermions and bosons is proposed so that

$$Q|\Phi_f >= |\Phi_B >, \qquad Q|\Phi_B >= |\Phi_f >, \tag{1.6}$$

where Q is an operator that generates transformations between fermions and bosons; $|\Phi_f >$ is a fermionic state; and $|\Phi_B >$ is a bosonic state. In this way, a supersymmetric fermion is predicted for each boson in the SM and a supersymmetric boson is predicted for each fermion in the SM. These supersymmetric particles have the same masses and quantum numbers as their SM counterparts, except their spin differs by a half-integer.

In the SM only one Higgs scalar field was required to give mass to all the fermions and weak gauge bosons. The SM Higgs field is a doublet, which has four degrees of freedom, three of which are lost in EW symmetry breaking, resulting in just one Higgs boson. However, in the MSSM, two scalar Higgs fields are needed in order to give mass to the super-partners after EW symmetry breaking. The two MSSM Higgs doublets $H_u = \begin{pmatrix} H_u^+ \\ H_u^0 \end{pmatrix}$ and $H_d = \begin{pmatrix} H_d^0 \\ H_d^- \end{pmatrix}$ have eight degrees of freedom, three of which are lost in EW symmetry breaking, resulting in five Higgs bosons H^+, H^-, h^0, H^0, A^0. The lightest MSSM Higgs boson h^0 is considered to be the equivalent of the SM Higgs boson.

Sparticles

SUSY is a natural theory which calls upon the traditional technique of introducing new particles to explain problems in the Standard Model. This predicts a spectrum of sparticles, as seen in Table 1.3. The super-partner of a SM particle is denoted by a tilde and the naming convention is to add the prefix $s-$ for the super-partner of a SM fermion, and to add the postfix $-ino$ for the super-partner of a SM boson. For example, the electron e has a super-partner called a selectron $\tilde{e}$ and the gluon g has a super-partner called a gluino $\tilde{g}$.

In the SM, it was seen that the gauge bosons mixed to give the mass eigenstates $W^{\pm}$, Z and γ. Similarly, in the MSSM, the neutral higgsinos and gauginos $\tilde{H}_u^0$, $\tilde{H}_d^0$, $\tilde{W}^0$, $\tilde{B}$ mix to give four mass eigenstates $\tilde{\chi}_1^0$, $\tilde{\chi}_2^0$, $\tilde{\chi}_3^0$, $\tilde{\chi}_4^0$ called neutralinos. In addition, the charged higgsinos and gauginos $\tilde{H}_u^+$, $\tilde{H}_d^-$, $\tilde{W}^+$, $\tilde{W}^-$ mix to give two mass eigenstates $\tilde{\chi}_1^{\pm}$, $\tilde{\chi}_2^{\pm}$, called charginos. The four neutralinos and two charginos are collectively referred to as gauginos.

R-Parity

Quarks and squarks carry a quantum number called baryon number B, which is $+\frac{1}{3}$ for particles

Particle	Spin	Super-partner	Spin
l q	$\frac{1}{2}$	$\tilde{\ell}$ $\tilde{q}$	0
g W^+, W^-, W^0 B	1	$\tilde{g}$ $\tilde{W}^+, \tilde{W}^-, \tilde{W}^0$ $\tilde{B}$	$\frac{1}{2}$
$H_u^+, H_u^0, H_d^-, H_d^0$	0	$\tilde{H}_u^+, \tilde{H}_u^0, \tilde{H}_d^-, \tilde{H}_d^0$	$\frac{1}{2}$

Table 1.3: The super-partners of the particles in the MSSM.

and -$\frac{1}{3}$ for antiparticles. Leptons and sleptons carry a quantum number called lepton number L, which is +1 for particles and -1 for antiparticles. The MSSM allows both baryon and lepton number violating couplings, which predicts that the proton can decay very quickly to lepton plus meson final states in $\sim 10^{-2}$ s. This is clearly not the case and the lower limit on the proton lifetime has been measured experimentally at 1.6×10^{33} years [19]. The large discrepancy between the MSSM prediction and experiment strongly suggests that baryon and lepton numbers must be conserved in particle interactions.

A new symmetry is introduced, called "R-parity", the conservation of which prevents both baryon and lepton violating couplings. R-parity conservation does, however, allow B violation and L violation if they occur in the same amounts. The R-parity of a particle is defined as

$$R = (-1)^{3(B-L)+2S}, \tag{1.7}$$

where B is the baryon number; S is the spin; and L is the lepton number. The R-parity of a SM particle is +1, whereas SUSY sparticles have R-parity of -1. By requiring that R-parity is conserved, the MSSM prediction for the proton lifetime is increased to $\sim 10^{32}$ years, which is in closer agreement with the measured value.

R-parity conservation has a great influence over the phenomenology of the MSSM. In the pp collisions at the Large Hadron Collider, the sparticles will have to be produced in pairs (sparticle plus anti-sparticle) to conserve R-parity. If R-parity is to be conserved at every interaction vertex, then each sparticle must decay into an odd number of other sparticles. Moreover, the lightest SUSY particle (LSP) must be stable. In this thesis, only R-parity conserving SUSY models are considered.

Dark Matter

If the LSP is indeed stable it may provide a good candidate for the dark matter in the universe. In fact, for many R-parity conserving MSSM models the LSP is the lightest neutralino $\tilde{\chi}_1^0$, which is very weakly interacting, massive and electrically neutral. This combination yields a prime dark matter candidate that is in agreement with cosmological data (see Section 1.3 for further discussion). If sparticles are produced at the LHC and decay to a LSP like the $\tilde{\chi}_1^0$, it will not be possible to detect the LSPs directly, due to their very nature. Instead, their presence will be inferred in the LHC detectors by a significant energy imbalance in the event kinematics.

1.2.3 SUSY Breaking

The symmetry proposed in Section 1.2.2 between fermions and bosons was presented as an exact symmetry, where the masses of the super-partners are equal to the masses of their SM counterparts, and the interaction strengths are also the same. However, all experimental results to date find that there are no two particles with equal mass that differ in spin by one half integer. Therefore, SUSY is assumed to be a spontaneously broken symmetry, which allows the masses of the sparticles to be much larger than their SM partners.

SUSY may be explicitly broken in the MSSM by adding mass terms to the MSSM Lagrangian $\mathcal{L}_{MSSM}$. To ensure that the solution to the hierarchy problem is retained, the mass differences between the SM and SUSY particles must not be too large, thus, the explicitly added mass terms must be "soft". The MSSM Lagrangian then becomes

$$\mathcal{L}_{MSSM} = \mathcal{L}_{SUSY} + \mathcal{L}_{soft}\,, \tag{1.8}$$

where $\mathcal{L}_{SUSY}$ contains the SUSY invariant terms and $\mathcal{L}_{soft}$ contains the SUSY violating terms. The $\mathcal{L}_{SUSY}$ term adds only one mass parameter in addition to the nineteen SM parameters, but $\mathcal{L}_{soft}$ adds another 105 extra parameters (masses, phases and mixing angles) due to the unknown SUSY breaking mechanism. In defining the MSSM Lagrangian as Equation 1.8, SUSY breaking is analogous to EW symmetry breaking, with a Lagrangian density that is invariant under SUSY transformations, but with a vacuum state that is not. Thus, SUSY breaking is said to occur in the "hidden" sector, with no direct couplings to the "visible" MSSM and is instead "mediated" to the MSSM through particles such as the graviton.

The precise mechanism of SUSY breaking is unknown and there are multiple methods that exist to do so. Among the most popular models are minimal SuperGravity (mSUGRA) [20], where SUSY is broken by gravitational interactions, Gauge Mediated Supersymmetry Breaking (GMSB) [21], where SUSY is broken by gauge interactions, and Anomaly Mediated Supersymmetry Breaking (AMSB) [22], where SUSY is broken by the super-Weyl anomaly. In defining the SUSY breaking mechanism, each model greatly decreases the number of additional parameters associated with the MSSM to a relatively acceptable number.

mSUGRA

mSUGRA communicates SUSY breaking from the hidden sector to the MSSM via flavour-blind gravitational interactions and is the SUSY breaking model studied in this thesis. The mediating gravitational interactions are assumed to be from new physics that occurs above the Planck energy scale ($\sim 10^{19}$ GeV).The mSUGRA parameter space is characterised by four parameters and one sign:

$$m_0\,,\ m_{1/2}\,,\ A_0\,,\ \tan\beta\,,\ sign(\mu)$$

where m_0 is the GUT scale unified scalar mass; $m_{1/2}$ is the GUT scale unified gaugino mass; A_0 is the trilinear coupling; β is the ratio of the H_u and H_d VEVs; and sign(μ) is the sign of the higgsino mass parameter. The rich phenomenology offered throughout mSUGRA parameter space is particularly attractive and an in-depth discussion of the phenomenology of some mSUGRA scenarios may be found in Chapter 3. The mSUGRA parameter space may be constrained using precision experimental data, which is the topic of discussion of Section 1.3.

1.3 Experimental Constraints

Precision measurements of temperature anisotropies in the cosmic microwave background radiation (CMBR) from the Wilkinson Microwave Anisotropy Probe (WMAP) show that the universe is made from $\sim$73% dark energy and just $\sim$27% matter. By combining results from WMAP with the distribution of galaxies from Baryon Acoustic Oscillations (BAO) and distance measurements from Type 1a supernovae (SNe), the matter density of the universe is measured to be $\Omega_m h^2 = 0.1358^{+0.0037}_{-0.0036}$ [23]. However, the baryonic matter density is measured to be only $\Omega_b h^2 = 0.02267^{+0.00058}_{-0.00059}$, while the cold dark matter density is much larger and is measured as $\Omega_c h^2 = 0.1131 \pm 0.0034$. This non-baryonic cold dark matter cannot be fully explained by the

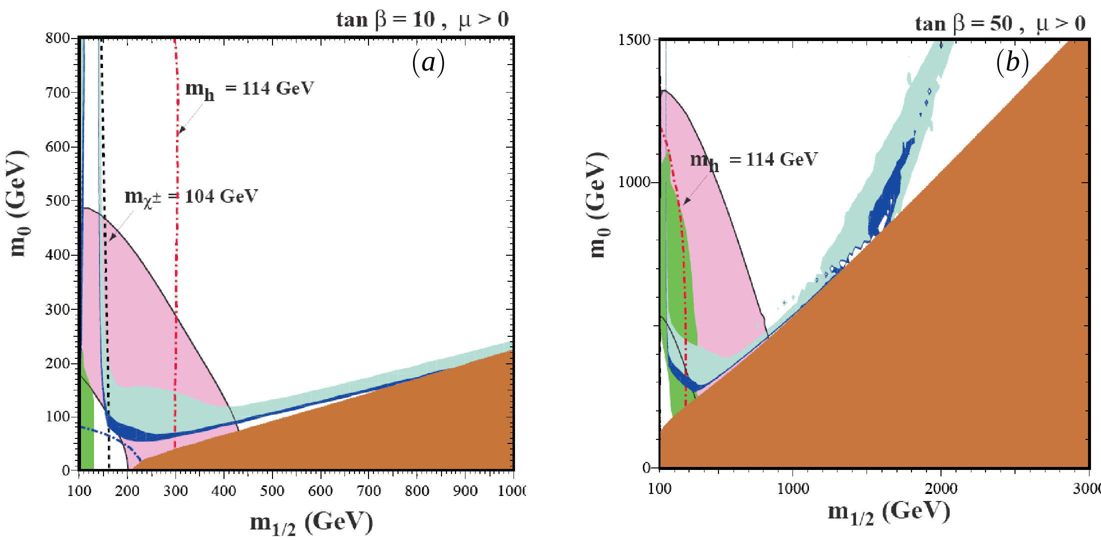

Figure 1.4: The mSUGRA m_0 vs $m_{1/2}$ parameter space for A_0=0, positive sign(μ) and with $\tan\beta$=10, (a), or with $\tan\beta$=50, (b). The brown regions are excluded due to a charged LSP (usually the $\tilde{\tau}_1^{\pm}$) and the green regions are excluded using precision rate measurements of $b \rightarrow s\gamma$. The light blue regions are those consistent with pre-WMAP data, while the dark blue regions are in agreement with the dark matter relic density from WMAP. The pink regions are those favoured by measurements of the anomalous magnetic moment of the muon. Also included are lines showing a MSSM Higgs boson mass of 114 GeV, a $\tilde{\chi}_1^{\pm}$ mass of 104 GeV and for (a) the dashed curved line in the bottom left corner shows the LEP constraint on $\tilde{e}$ (from [25]).

SM, however, R-parity conserving MSSM models may hold the answer. If the MSSM LSP is stable, neutral, weakly interacting and has a mass less than $\sim$ 1 TeV, it provides an ideal candidate for the non-baryonic cold dark matter in the universe.

The results of cosmological measurements may be used to constrain the parameters of MSSM models, such as mSUGRA. At each point in mSUGRA parameter space the SUSY mass spectrum, branching ratios and decay widths may be calculated, which results in a LSP relic density that may be compared to the WMAP cold dark matter density. In Figure 1.4, the constrained mSUGRA parameter space is shown as a function of m_0 and $m_{1/2}$ for constant values of A_0 and sign(μ) and two differing values of $\tan\beta$. The WMAP data tightly constrains the mSUGRA parameter space to a narrow band that is used to direct mSUGRA benchmark scenarios for study [24].

In conclusion, the SM does not provide a sufficient description of particles and their interactions at high energy scales and so new physics, such as SUSY, is predicted at energies above the electroweak breaking scale. Since SUSY is a broken symmetry, it is assumed to be a low energy approximation of an even higher energy theory and although SUSY itself lacks a quantum description of gravity, it may provide a stepping stone towards it. The Large Hadron Collider at CERN is dedicated to probing physics in the TeV region and may soon discover the elusive Higgs boson and a spectrum of massive SUSY particles.

Chapter 2

The ATLAS Experiment at the LHC

Since its beginnings in 1954, CERN (European Organisation for Nuclear Research) has provided countless valuable insights into fundamental physics. It is currently the world's largest scientific laboratory, involving over 10,000 physicists from over 80 different countries. This truly international community of physicists is now embarking on the biggest experiment in scientific history, the Large Hadron Collider.

2.1 The Large Hadron Collider

On the 10^{th} September 2008, the Large Hadron Collider (LHC) at CERN successfully circulated proton beams in both directions around the accelerator ring for the very first time. Constructed in the old LEP tunnel, 100 m under the Swiss-Franco border, the LHC will soon accelerate and collide proton beams at unprecedented centre of mass energies up to 14 TeV in the search for new physics.

Before the protons reach the main LHC ring, they are accelerated in stages by a series of smaller machines. Firstly, protons travel through a small linac and booster. They are then injected into the Proton Synchrotron (PS), where they are accelerated to an energy of 26 GeV. Next, the protons are injected into the Super Proton Synchrotron (SPS), where they are accelerated to 450 GeV. At this stage the protons are ready to be injected into the LHC, which will be capable of accelerating the protons to impressive energies of 7 TeV per beam. In addition to studying pp collisions, the LHC will also study the collisions of heavy ions. Thus, for a few weeks each year, the LHC will accelerate and collide lead ions at energies of 5.5 TeV per nucleus and a luminosity

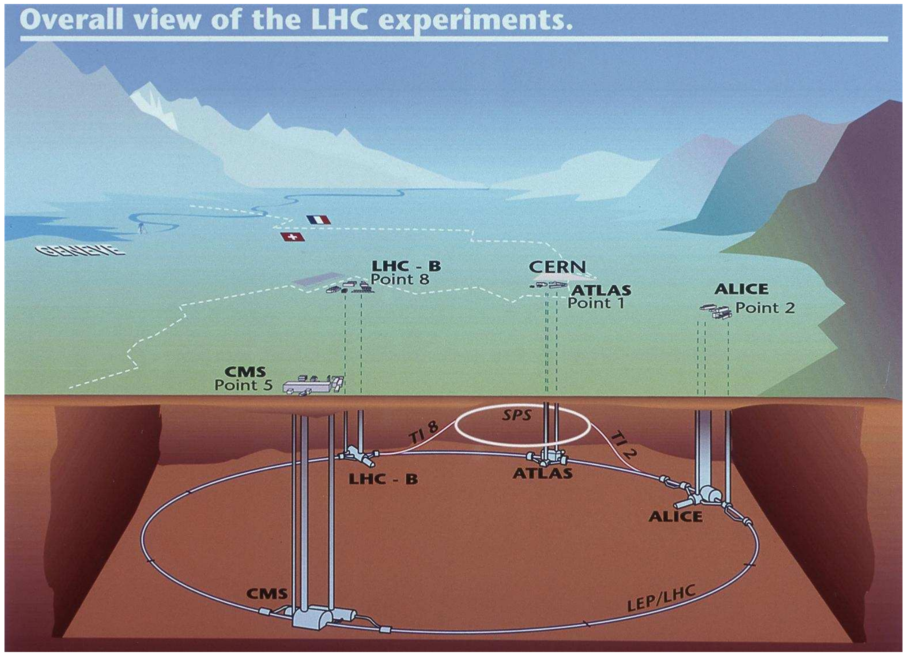

Figure 2.1: A sketch of the Large Hadron Collider and the four main experiments ATLAS, CMS, LHCb and ALICE (from [26]).

of 10^{27} $\text{cm}^{-2}\text{s}^{-1}$.

The proton beams will be collided at the four points around the LHC where the four main experiments are located, as shown in Figure 2.1. Both ATLAS (A Toroidal LHC ApparatuS) and CMS (Compact Muon Solenoid) are large multi-purpose detectors designed to search for new physics beyond the SM in a variety of channels, whereas LHCb (Large Hadron Collider beauty) will specialise in b-quark physics and ALICE (A Large Ion Collider Experiment) will study the physics of strongly interacting matter at extreme energy densities. The centre of mass energy (E_{CM}) of 14 TeV to be achieved at the LHC will be seven times that of the Tevatron and the beam luminosity will be 100 times greater, making the LHC the world's most powerful operational particle accelerator.

To obtain beam energies of up to 7 TeV, superconducting magnets with high field strengths of 8.4 T will be used to bend the proton beams around the 27 km circumference LHC tunnel. In each beam, the protons will be grouped into ~ 2800 bunches of $\sim 10^{11}$ protons each. The time spacing of the proton bunches will be 25 ns, and consequently, the interactions between the two proton beams will occur at discrete intervals. At peak design luminosity there will be 4×10^{7} bunch crossings per second. The high luminosity at the LHC will produce $\sim$23 low energy inelastic

Parameter	Value
Beam energy at collision	7 TeV
Beam energy at injection	450 GeV
Machine circumference	27 km
Power consumption	120 MW
Peak design luminosity	10^{34} cm^{-2}s^{-1}
Number of protons per bunch	1.15×10^{11}
Number of bunches per beam	2835
Time between bunches	25 ns
Bunch frequency	40 MHz
Number of interactions per bunch crossing	$\sim$23
RMS bunch length	7.55 cm
RMS beam size at collision	16 μm
Beam lifetime	22 hours
Circulating beam current	0.53 A
Crossing angle	200 μrad
Magnetic field strength	8.4 T
Cryostat temperature	1.9 K
Number of dipole magnets	1232
Number of quadrupole magnets	400

Table 2.1: LHC machine parameters (from [27]).

pp interactions per bunch crossing. These are known as "pile-up" events and will need to be well-understood if new physics is to be discovered at the LHC. The basic LHC parameters are listed in Table 2.1.

The first LHC proton collisions are scheduled to take place in the last quarter of 2009, at an initial centre of mass energy of $\sim$10 TeV and luminosity of $\sim 10^{31}$ cm^{-2}s^{-1}. A total integrated luminosity of $\sim$200 pb^{-1} is foreseen by autumn 2010 and lead ion collisions could potentially take place later the same year. After a short shutdown, the centre of mass energy and the luminosity are expected to be increased to 14 TeV and 10^{33} cm^{-2}s^{-1} respectively, and eventually the design luminosity of 10^{34} cm^{-2}s^{-1} is anticipated to be reached after three years of running.

2.2 The ATLAS Detector

The ATLAS detector is the largest of the four main detectors constructed around the LHC ring. The detector is a traditional barrel design, as shown in Figure 2.2, with a diameter of 25 m, length of 44 m and total weight of 7,000 tonnes. The ATLAS detector has been designed to detect

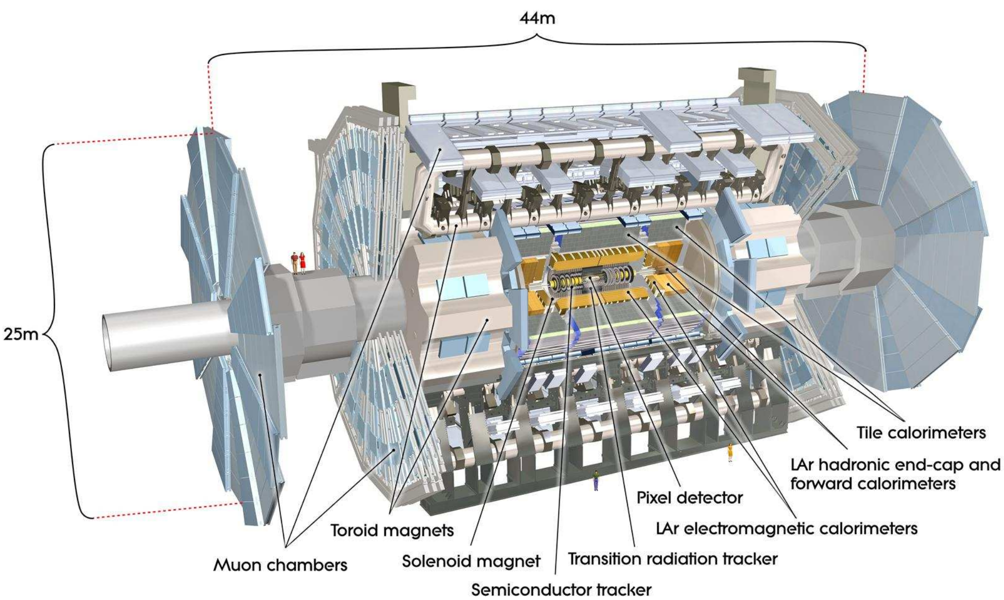

Figure 2.2: A sketch of the ATLAS detector (from [26]).

the charged and neutral particles that will be the decay products of massive unstable particles produced in the high-energy LHC pp collisions.

The geometry of the ATLAS detector is defined with the positive x-axis in the direction of the centre of the LHC ring, the positive y-axis pointing upwards and the z-axis in the direction of the beam line. Since the ATLAS detector is cylindrical, it is also convenient to define r as the transverse radius from the beam pipe, θ as the angle from the beam pipe and ϕ as the azimuthal angle around the beam axis as measured from the x-axis.

The exact momenta of the proton constituents (partons) that interact in pp collisions will be unknown, since momenta sharing amongst the partons will not be equal and instead will follow a parton distribution function [28]. Due to this complicated nature of hadron collisions, the measured momentum and energy of particles along the z-axis is not very useful, because the exact E_{CM} of each parton interaction will not be known. This will make total energy and momentum conservation calculations impossible along the z-axis. Thus, the energy and momentum of measured particles in ATLAS are usually quoted in terms of the transverse plane $x-y$ (the total transverse energy and momentum for each interaction will be zero), where transverse momentum is defined as

$$p_T = \sqrt{p_x^2 + p_y^2}, \tag{2.1}$$

and transverse energy is defined as

$$E_T = \sqrt{E_x^2 + E_y^2}, \tag{2.2}$$

where x and y are the x and y components of the momentum p or energy E. The rapidity of a particle y is a dimensionless quantity that describes the angle of a particle to the beam axis and is defined as

$$y = \frac{1}{2} \ln \left[\frac{E + p_L}{E - p_L} \right]. \tag{2.3}$$

where p_L is the longitudinal component of the momentum of the particle. Differences in rapidity ($y_1 - y_2$) are invariant under longitudinal (z) Lorentz boosts and thus useful when the z momenta of the interacting partons is not known. In the relativistic limit, rapidity is approximated by pseudorapidity η, which is defined as

$$\eta = -\ln \left[\tan \left(\frac{\theta}{2} \right) \right]. \tag{2.4}$$

Thus, particles close to the beam pipe have high $|\eta|$ and are described as "forward", while particles with a large angle from the beam pipe have low $|\eta|$ and are described as "central". The ATLAS detector covers a pseudorapidity range of $|\eta| < 5$.

As one of the general purpose detectors at the LHC, ATLAS has defined a broad physics programme to be covered. Precision measurements of the top quark and the other SM particles will be very important, both for the calibration of the detector and to understand the SM at high energies. In addition, the searches for the elusive Higgs boson and any new physics such as SUSY, are considered top priorities at ATLAS.

The ATLAS detector is comprised of multiple sub-detectors, where each has a specific role to play in the accurate measurement and identification of particles. Inner detectors provide accurate momentum and vertexing measurements of charged particles, outer calorimeters measure energy deposits from electromagnetic and hadronic particles, while the largest component, the muon system, will measure the muons that penetrate the entire ATLAS detector. The resolutions for energy and momentum measurements in each subdetector of the ATLAS detector, as well as their η coverage, are shown in Table 2.2. The reconstruction of missing energy in the ATLAS detector requires multiple sub-detectors, and so a discussion of missing energy and its associated

Subdetector	Resolution [GeV]	$\|\eta\|$
Inner Detector	$\frac{\sigma_{p_T}}{p_T} = 0.05\% p_T \oplus 1\%$	<2.5
Electromagnetic Calorimeter	$\frac{\sigma_E}{E} = \frac{10\%}{\sqrt{E}} \oplus 0.7\%$	<3.2
Hadronic Calorimeter		
barrel + end-cap	$\frac{\sigma_E}{E} = \frac{50\%}{\sqrt{E}} \oplus 3\%$	<3.2
forward	$\frac{\sigma_E}{E} = \frac{100\%}{\sqrt{E}} \oplus 10\%$	3.1 - 4.9
Muon Spectrometer	$\frac{\sigma_{p_T}}{p_T} = 10\%$ at $p_T = 1$ TeV	<2.7

Table 2.2: The momentum and energy resolutions of the subsystems of ATLAS, as well as their pseudorapidity coverage. The first terms are due to statistical fluctuations and the second terms are due to detector non-uniformity and calibration uncertainty, where $\oplus$ denotes addition in quadrature. Terms due to electrical noise in readout systems are not considered here.

resolution can be found separately in Section 2.2.5. The ATLAS experiment will also require a sophisticated trigger and data acquisition (TDAQ) system to filter and record the interesting physics events from the one billion collisions per second produced at the LHC. The different subsystems are discussed in the following sections, starting from the centre of detector and moving radially outwards. A thorough report of the ATLAS detector can be found in [29].

2.2.1 The ATLAS Inner Detectors

Every 25 ns, proton bunches will collide at the interaction point within the ATLAS detector, producing over 1,000 particles. The very high density of charged particles passing through the ATLAS detector presents a challenging environment in which precision position and momentum measurements will need to be made. Thus, the inner detector has been designed and built to provide the high performance required for physics searches at the LHC.

The inner detector is made from three separate components, as shown in Figure 2.3: the pixel detector, the semiconductor tracker (SCT) and the transition radiation tracker (TRT), which are immersed in a 2 T magnetic field from the central solenoid. The magnetic field direction is along the beam axis, which bends charged particles in inverse proportion to their momentum. The inner detector aims to provide tracking for charged particles with $p_T > 0.5$ GeV and $|\eta| < 2.5$, with a resolution of $\sigma_{p_T}/p_T = 0.05\% p_T \oplus 1\%$, as seen in Table 2.2. Material thickness has been minimised to ensure the outer detectors can accurately measure particle energies.

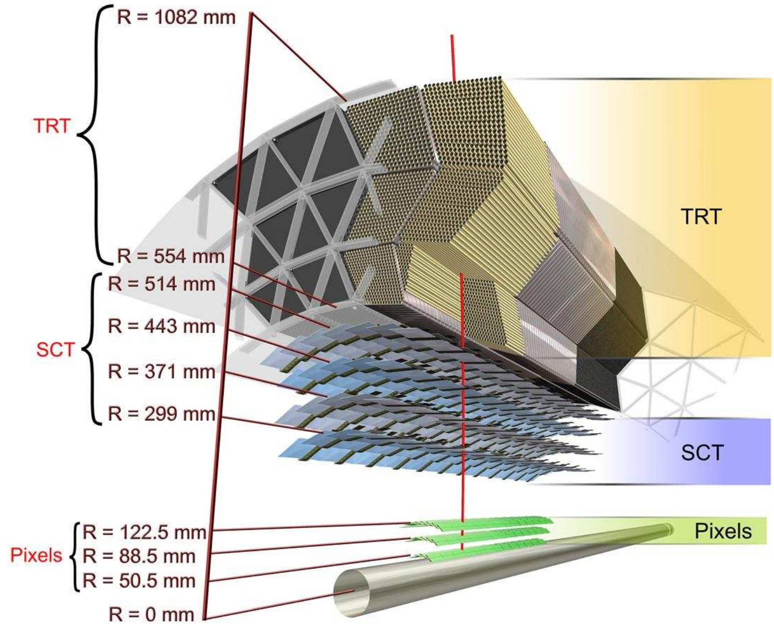

Figure 2.3: The three components of the inner detector. The path of a high energy particle is shown in red (from [26]).

Pixel Detector

The pixel detector is the closest part of the ATLAS detector to the interaction point and will provide the most precise tracking information out of all the inner detectors. Accurate position measurements will enable primary and secondary vertexing and measurement of associated particle decay lengths to identify prompt and short lived particles. This will aid in the "tagging" of particles such as the b-quark and the τ lepton, both essential to many physics searches. Therefore, the innermost barrel layer (B-layer) of the pixel detector is placed as close as possible to the beam pipe, which itself has an outer radius of 30 mm. Despite the fact that the ATLAS detector components are designed to be radiation hard, when the LHC is operational, the B-layer will receive an enormous amount of radiation damage and will need to be replaced every few years.

The pixel detector is comprised of three cylindrical layers in the barrel placed at radii 50.5 mm, 88.5 mm and 122.5 mm, and three disk layers in each of the two end-caps. With this layout, a charged particle will typically pass through three pixel layers. When a charged particle passes through the silicon in a pixel, electron-hole pairs are created. A bias voltage across the pixel causes the electron-hole pairs to drift towards the readout cathode, where a "hit" is recorded if the charge collected exceeds a particular threshold value.

The pixel layers are made from rectangular silicon wafers, roughly 2 cm $\times$ 6 cm in size, with 46,080 pixels each. In total, 80 million pixels of size 50 μm $\times$ 400 μm provide the high granularity demanded for high precision tracking. The pixel detector has an intrinsic accuracy of 10 μm in the $r-\phi$ plane and 115 μm along z in the barrel (or r in the end-caps). The superior performance of the pixel detector is at the limit of current technology, and the high costs of production prohibits the use of pixels throughout the entire inner detector.

SCT

The SCT is the second component of the tracking system and together with the pixel detector, it provides tracking for $|\eta| < 2.5$. The SCT is a cheaper alternative to the pixel detector, since far fewer readout channels are needed due to the lower track density at larger radius. A charged particle passing through a silicon strip leaves a "hit" in the same way as in the pixel detector.

The SCT is composed of four cylindrical layers in the barrel placed at radii 299 mm, 371 mm, 443 mm and 514 mm and nine disk layers in each of the two end-caps. The SCT layers are made from 4,088 two-sided silicon micro-strip modules. Each module consists of four silicon wafers of size 63.6 mm $\times$ 64.0 mm with 80 μm pitch strips, where two wafers are wire-bonded end-to-end. The pairs of silicon strips are glued back-to-back at angles of 40 mrad to allow position measurements in the z direction. The SCT has an intrinsic accuracy of 17 μm in the $r-\phi$ plane and 580 μm along z in the barrel (or r in the end-caps).

TRT

The outermost part of the inner detector is the TRT - a lightweight, low-cost drift tube system that provides tracking up to a radius of 1062 mm and $|\eta| < 2.0$. Due to its large size, the TRT contributes the largest number of tracking measurements in the tracking system and can also provide information for particle identification.

The TRT is made from gas-filled (Xe, CO_2, O_2) "straws" of diameter 4 mm, each containing a 0.03 mm diameter gold-plated tungsten wire. When a charged particle passes through a straw, the gas is ionised and a "hit" is detected in a similar way to the silicon detectors. The TRT is made from a main barrel section comprising 50,000 straw detectors of length 144 cm aligned with the beam axis and two end-caps each with 160,000 radially aligned straws of length 37 cm.

The TRT also has the ability to generate and detect transition radiation. Polypropylene radiator material in-between the straws results in layers of materials with differing dielectric constants. When a charged particle with high-γ (where $\gamma = E/m$) passes through a straw-polypropylene

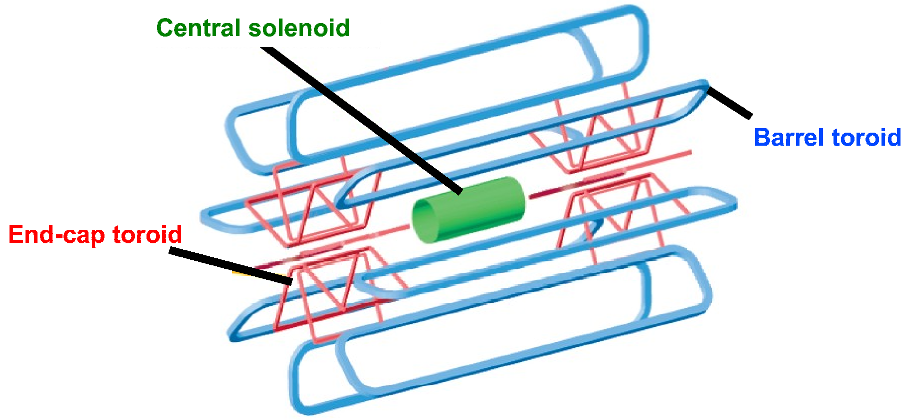

Figure 2.4: The three components of the ATLAS magnet system: the central solenoid *(green)*, the barrel toroid *(blue)* and the two end-cap toroids *(red)* (adapted from [27]).

boundary, it will emit x-rays, known as transition radiation, which will produce a second, higher threshold "hit". In this way, electrons may be differentiated from hadrons, since they will emit transition radiation at energies above $\sim$1 GeV due to their low mass, whereas more massive pions will only emit transition radiation for energies above $\sim$100 GeV. The TRT has an intrinsic accuracy of 130 μm and only provides tracking information in the $r-\phi$ plane.

On average, a charged particle produced at the interaction point will pass through three layers of pixels, four layers of SCT and 36 straws in the TRT. The high-cost silicon pixels and strips provide precision positioning in r, ϕ and z, while the low-cost TRT contributes significantly to accurate momentum measurement. Collectively, the inner detector is an excellent high performance tracking system.

2.2.2 The ATLAS Magnet System

The ATLAS magnet structure is the most visually impressive part of the entire detector and drives the geometry of the surrounding subsystems. Powerful magnetic fields are needed throughout multiple parts of the ATLAS detector to bend the paths of charged particles and provide accurate momentum measurements. The ATLAS magnet system is comprised of three main systems: the central solenoid, the barrel toroid and the end-cap toroids, as seen in Figure 2.4.

The 5 tonne central solenoid is 5.3 m in length, 2.4 m in diameter and provides a 2 T magnetic field along the beam axis in the inner detectors. In order to minimise the amount of material in front of the calorimeters, the central solenoid is very thin in comparison to its overall size, with a thickness of just 45 mm. It has been designed to allow accurate momentum measurements in the inner detectors for particles with momenta up to 100 GeV.

The toroid system generates a 4 T magnetic field in the toroid superconductors, which falls to an average magnetic field of strength 0.5-1 T in the muon spectrometer and allows momentum measurements for muons with momenta up to 6 TeV. The barrel toroids are eight huge superconducting coils of length 25 m and width 5 m, radially positioned within the ATLAS detector and weigh a total of 830 tonnes. The barrel toroid magnets are so large that it was necessary to install them first in the ATLAS cavern and build the rest of the detector around them. Two smaller 240 tonne, 5 m long end-cap toroids, comprising eight coils each, are slotted in-between the barrel coils to complete the toroid magnet system.

The 1,300 tonnes of superconducting NbTi coils in the magnet system are cooled using liquid helium to a temperature 4.5 K. The magnetic field of the barrel toroid dominates for $|\eta| < 1.4$, whereas the end-cap magnetic field dominates for $1.6 < |\eta| < 2.7$. Bending power is lower where the two magnets overlap, for $1.4 < |\eta| < 1.6$.

2.2.3 The ATLAS Calorimeters

The ATLAS calorimetry system is built around the central solenoid and inner detectors and is dedicated to stopping and measuring the energies of photons, electrons and hadronic particles. Unlike the inner detectors, the calorimeters can detect both neutral and charged particles. Fine granularity is required for particle identification and the calorimeters need to be as uniform as possible to allow for good measurements of missing energy. The combination of barrel, end-cap and forward calorimetry, as shown in Figure 2.5, provides a total coverage of $|\eta| < 4.9$.

ATLAS has two calorimeters to measure electromagnetic and hadronic particles, since each interact rather differently with matter. Electromagnetic particles are less penetrating and produce narrower showers than hadronic particles passing through matter. Electrons lose energy via bremsstrahlung, whereas photons lose their energy via electron-positron pair production. Hadronic particles interact with matter via the strong force and produce wide showers in the calorimeters. Since the average nuclear interaction length λ is ten times the average electromagnetic radiation length X_0, hadronic particles penetrate far further into the ATLAS detector than electrons and photons. Indeed, the calorimeters have been designed to absorb as much hadronic

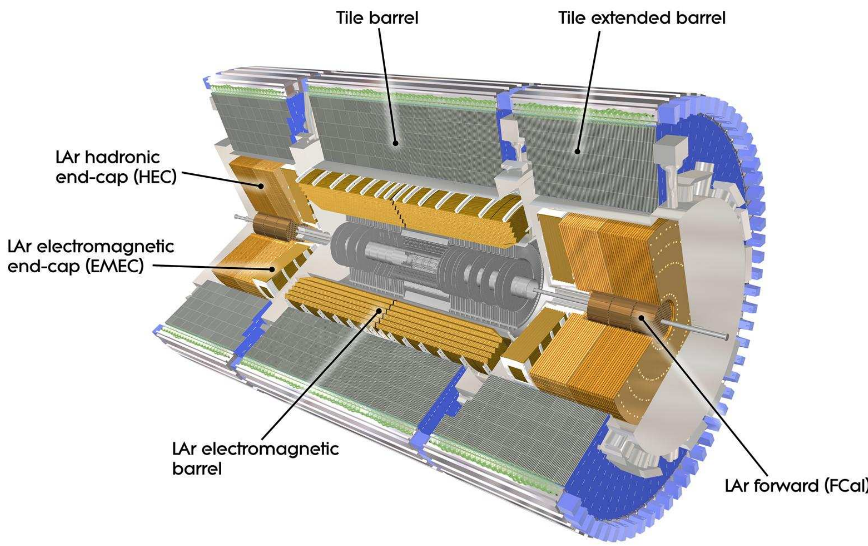

Figure 2.5: A sketch of the calorimeter system of the ATLAS detector (from [26]).

and electromagnetic activity as possible to prevent “punch-through” to the muon system affecting muon measurements. By measuring the energies, shapes and depths of showers in the calorimeters, electrons and photons may be distinguished from hadrons. Collections of hadronic showers in the ATLAS calorimeters are reconstructed as single objects, referred to as “jets”.

The innermost calorimeter is the electromagnetic calorimeter (ECAL), which has the fine granularity required to make precision measurements of electrons and photons. The outer calorimeter, the hadronic calorimeter (HCAL), has a coarser granularity in comparison, but is considered good enough for jet and missing energy measurements at ATLAS. Both are “sampling” calorimeters; using one material to initiate showering and another to measure the energy. By layering the two materials, the total energy of a particle may be measured as it loses its energy in stages through the calorimeters. Due to intrinsic differences in the ECAL and HCAL, they respond differently to electromagnetic and hadronic showers. Understanding this difference is vital, as over or under-correcting the jet energy scale in the offline software can introduce large errors for physics analyses.

Electromagnetic Calorimeter

The ECAL will initiate and detect electromagnetic showers from photons and electrons, as well as any hadronic showers that may begin before the HCAL. It is composed of a barrel and two end-caps. The barrel is made from two identical sections, each 3.2 m long, with inner radii 2.8 m and outer radii 4 m which will provide coverage in $|\eta| < 1.475$. Each end-cap is made from an outer disk giving coverage for $1.375 < |\eta| < 2.5$ and an inner disk covering $2.5 < |\eta| < 3.2$. There is a 4 mm gap where the two barrel sections meet at $z = 0$, and in the coverage at $1.37 < |\eta| < 1.52$ where the barrel and end-caps meet.

The ECAL uses layers of lead sandwiched in-between layers of liquid argon kept at 89.3 K. The lead layers cause the photons and electrons to shower, while the liquid argon layers detect the shower particles. Liquid argon has been chosen as the detector material as it is radiation hard and gives good energy resolution. The ECAL is built using an accordion geometry that gives complete coverage in ϕ, which is essential for missing energy measurements. A thin liquid argon presampler lies between the inner detectors and the ECAL to correct for energy loss in the inner detectors and solenoid by electrons and photons for $|\eta| < 1.8$.

For a good energy measurement of photons and electrons, they need to shower completely within the ECAL, thus, the barrel is over 22 X_0 thick and the end-caps are over 24 X_0 thick. High granularity in the ECAL provides excellent shower position, shape and energy measurements as well as effectively distinguishing electrons and photons from pions. The energy resolution in the ECAL is $\sigma_E/E = 10\%/\sqrt{E} \oplus 0.7\%$, as seen in Table 2.2.

Hadronic Calorimeter

The HCAL will initiate and measure hadronic showers and act as a shield to prevent any hadronic particles reaching the muon spectrometer. It is composed of a barrel system, two end-caps and a forward calorimeter, each of which uses different techniques for calorimetry.

The barrel system of the HCAL is made from a main barrel with two extended barrels, one on each side, as seen in Figure 2.5. The main barrel provides coverage for $|\eta| < 0.8$ and the extended barrels increase this out to $|\eta| < 1.7$. The barrel system is made from alternating layers of steel to cause the hadronic particles to shower, and plastic scintillator tiles to measure the showers.

The two hadronic end-caps are made from two disks each, with coverage of $1.5 < |\eta| < 3.2$. In this forward region, the detector components will be subject to higher levels of radiation from proton remnants than central regions of the detector. With this in mind, radiation hard copper and liquid argon are used to initiate and detect the hadronic showers respectively.

With a coverage of $3.1 < |\eta| < 4.9$, the forward calorimeter will suffer from even higher levels of radiation from proton remnants than the hadronic end-caps. Therefore, liquid argon is used again here to measure the showers, with layers of copper and tungsten to initiate the showering.

The forward calorimeter has a particularly high density in order to prevent leakage into the muon spectrometer and surrounding calorimeters.

The HCAL is $\sim$10 λ thick in the barrel, end-caps and forward calorimeter, to ensure that almost all hadron showers are contained completely within the HCAL and do not punch-through to the muon spectrometer. The energy resolution in the HCAL is $\sigma_E/E = 50\%/\sqrt{E} \oplus 3\%$ in the barrels and two endcaps and $\sigma_E/E = 100\%/\sqrt{E} \oplus 10\%$ in the forward calorimeter, as seen in Table 2.2.

Using the complete arrangement of calorimeters in ATLAS, it will be possible to accurately measure the energies of electrons, photons and jets, infer information for particle identification, make missing energy measurements and limit leakage of electromagnetic and hadronic showers into the muon system.

2.2.4 The ATLAS Muon Spectrometer

The muon spectrometer system is built in and around the toroid magnets surrounding the calorimeters and is the largest sub-detector within ATLAS. Muons are very penetrating, and along with "invisible" particles (i.e. weakly interacting neutral particles), such as neutrinos, will be the only particles capable of passing through the entire ATLAS detector. As muons pass through the detector, they will lose some of their energy in the calorimeters and this energy loss will be corrected for by measuring the calorimeter deposits. The minimum energy that muons need to have to reach and be detected in the muon spectrometer is $\sim$ 3 GeV.

The muon spectrometer is composed of three cylindrical layers of chamber detectors in the barrel at radii of 5 m, 7.5 m and 10 m, covering a range of $|\eta| <$1.0, and four layers of chambers in each of the two end-caps at $|z|$ of 7.4 m, 10.8 m, 14 m and 21.5 m, which cover a range of 1.0$< |\eta| <$2.7. Thus, a muon will typically pass through three layers of chambers. The chambers are arranged to overlap in ϕ to minimise any gaps and an opening at η =0 is left to allow access to the other detectors. The toroid magnets will provide a magnetic field in the muon spectrometer of strength 0.5 T in the central region and 1 T in the end-cap regions.

The muon spectrometer will provide high precision position and momentum measurements of high energy muons that may not have been well measured in the inner detectors. In addition, the muon system includes a separate trigger system used to trigger high energy muon events that will be essential for many physics searches. To meet these two objectives, four different chamber tech-

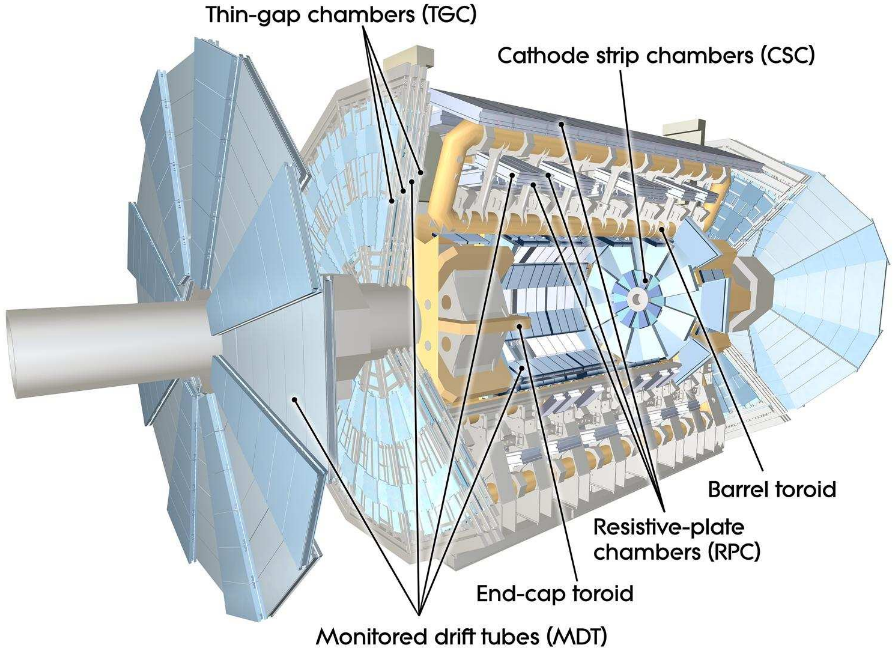

Figure 2.6: A sketch of the muon system of the ATLAS detector (from [26]).

nologies are incorporated into the muon spectrometer system; Monitored Drift Tubes (MDT's) and Cathode Strip Chambers (CSC's) constitute the "precision measurement chambers", while Resistive Plate Chambers (RPC's) and Thin Gap Chambers (TGC's) constitute the "dedicated trigger chambers". A schematic of the muon spectrometer is shown in Figure 2.6, where the locations of the four different chamber technologies are indicated.

Precision Measurement Chambers

The precision measurement chambers make up the tracking system in the muon spectrometer, with both MDT's and CSC's used. The MDT's are gas filled (Ar and CO_2 at a pressure of 3 bar) aluminium tubes, 30 mm in diameter, containing a 50 μm tungsten wire. When muons pass through a tube they ionise the gas and the ions are collected on the wire. In each chamber there are 3-8 layers of tubes varying between 85-650 cm long. The spatial resolution that can be achieved in a MDT chamber is 35 μm.

MDT's are used in the barrel and end-caps for $|\eta| <2.7$, however, CSC's are used for the innermost layer of the muon spectrometer for $2.0< |\eta| <2.7$, as they provide the higher granularity and faster detection rates required in these forward areas. CSC's are multi-wire proportional chambers (MWPC), with closely spaced anode wires in gas (Ar, CO_2, CF_4) and cathode strips placed orthogonally to the wires. In each chamber there are four CSC planes. The two dimensional spatial resolution per CSC chamber is 40 μm in r and 5 mm in ϕ.

Dedicated Trigger Chambers

Many physics signatures rely on the presence of high energy muons to pass the trigger and be recorded. However, the time for muons produced from the pp collisions in the centre of the ATLAS detector to reach the muon spectrometer is longer than the 25 ns proton beam bunch spacing. The precision measurement chambers are too slow for the successful triggering of events with high energy muons, therefore, fast, dedicated trigger chambers are used that can provide the information required within 15-25 ns of a muon passing through. The ATLAS trigger is discussed in detail in Section 2.2.6.

The dedicated trigger chambers cover a total of $|\eta| <2.4$, where RPC's are used in the barrel region with $|\eta| <1.05$ and the higher granularity TGC's are used in the end-caps, covering the $1.05< |\eta| <2.4$ regions. RPC's are made from two resistive plates filled with gas ($C_2H_2F_4$, Iso-C_4H_{10}, SF_6). A passing muon will ionise the gas inside an RPC, initiating ion avalanches along the side of the track towards the anode, which are then readout. TGC's use MWPC technology and are so-called because the gap between the wire and cathode is smaller than the distance between wires. The spatial resolution of the RPC's and TGC's is not as good as the precision measurement chambers, with 10 mm in z and ϕ for the RPC's, and 2-6 mm in r and 3-7 mm in ϕ for the TGC's. However, excellent timing resolutions are achieved of 1.5 ns for the RPC's and 4 ns for the TGC's, allowing for high energy muon events to be triggered.

Using a combination of precision measurement chambers and dedicated trigger chambers, the muon spectrometer will be capable of accurately measuring muons with $p_T > 3$ GeV and will provide vital information quickly for the trigger system. The momentum resolution in the muon spectrometer is $\sigma_{p_T}/p_T = 10\%$ for muons with $p_T = 1$ TeV, as seen in Table 2.2, however, this will be closer to 2-3 % for muons with lower p_T of ~ 20 GeV.

2.2.5 Missing Energy Reconstruction in ATLAS

The total energy of an event is reconstructed in ATLAS in the transverse plane by summing together the energy deposits in the ECAL and HCAL in addition to the tracks in the muon spectrometer. An imbalance in the total transverse energy of an event ΣE_T leads to a value for the missing transverse energy $\not{E}_T$. There are two main approaches to reconstruct the total energy of an event which both yield very similar performances: one that is "cell-based" and the other that is "object-based".

The cell-based method uses all the calorimeter cells and muon tracks as input, in addition to energy corrections from energy deposits in the cryostat between the two calorimeters. The calorimeter cells are weighted using the cell position and energy density. This cell-based method may be refined by modifying the cell weights according to the reconstructed objects the cells are associated with. The object-based method for reconstructing the total energy of an event relies of the reconstruction of electrons, photons, jets and muons. In addition, low-p_T objects that were not reconstructed into physics objects are added as input to the calculation.

There are numerous sources of fake missing energy, such as instrumental effects, noisy or dead calorimeter cells, badly reconstructed high-p_T muons and faked muons from calorimeter leakage, all of which may be understood with the very first ATLAS data. The estimated resolution of the missing transverse energy in ATLAS is $\sigma = a\sqrt{\Sigma E_T}$ where 0.53$<a<$0.57 for ΣE_T values ranging between 20 GeV and 2 TeV.

2.2.6 The ATLAS Trigger and Data Acquisition

When the LHC reaches its design luminosity of 10^{34} cm^{2}s^{-1} the proton bunch crossing rate at ATLAS will be 40 MHz and with multiple pp interactions expected for each bunch crossing, the event rate will be close to 1 GHz. Recording such a large number of events each second is far beyond the capabilities of current technology and disk space availability and so the ATLAS Trigger and Data Acquisition (TDAQ) is dedicated to reducing the event rate to be recorded by identifying "interesting" events. Lists of interesting signatures have been compiled, known as the "trigger menus" and are based on the needs of the physics searches at ATLAS. The definition of the trigger menu is essential to successfully reject minimum-bias events and, at the same time, maintain a high efficiency for any new physics. Items on a trigger menu typically request the presence of single/multiple high energy electrons, muons, photons or jets, or large missing energy, or even a combination of selections.

For any physics process to be accurately measured at ATLAS, it will be very important to understand which trigger it passed and at what rate. For each trigger item there is one or more lower threshold triggers to allow rate measurements. Some items on the trigger menu will result in an overwhelmingly high pass rate and need to be "prescaled", so that only a fraction of the events passing that trigger are actually recorded. It will be possible to manipulate any prescaling

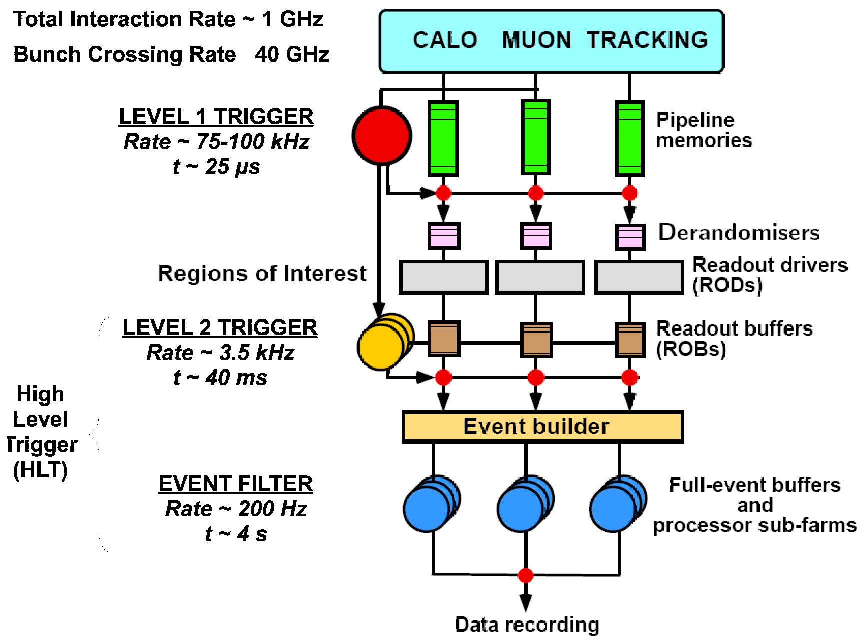

Figure 2.7: The ATLAS trigger system uses three levels to reduce the event rate from 1 GHz to ∼200 Hz (adapted from [26]).

as the LHC luminosity changes, in order to keep the event rate the same. Trigger menus are flexible, in order to allow changes if the unexpected is found at the LHC.

The ATLAS TDAQ system is shown in Figure 2.7 and uses three levels in the trigger chain; Level 1 (L1), Level 2 (L2) and the Event Filter (EF), where L2 and EF are collectively referred to as the High Level Trigger (HLT). Using information from the inner detector tracking, calorimeters and muon spectrometer, a combination of hardware in L1 and software in the HLT will reduce the event rate from 1 GHz to ∼200 Hz, which is just within the limit of technology to be written to disk.

Each event at ATLAS will be sent to the first level in the trigger chain, L1, which is hardware based. L1 will take coarse granularity (0.1×0.1 in $\Delta\eta\times\Delta\phi$) calorimetry information, in addition to information from the dedicated muon trigger chambers (as discussed in Section 2.2.4). No tracking information from the inner detectors will be used at L1, due to the time required to reconstruct the high track density that will be seen at ATLAS. L1 will look for signs of high-energy electrons, photons and jets, as well as significant missing energy using the calorimeter data and high energy muons using the muon trigger chamber data. With the limited information from the ATLAS detector used by L1, the trigger is able to make a decision whether an event should be passed to L2 in just 2.5 μs, and will reduce the event rate to 75-100 kHz.

When an event passes L1, it is sent to the second level in the trigger chain, L2, which is software based. L2 will receive information from L1 about the locations of high energy objects in the ATLAS detector, known as “Regions of Interest” (RoI). Only the RoIs of an event are examined at L2, but using the complete, high precision information from the detector in these areas, including the tracking information. Fine granularity data from the calorimeters, muon spectrometer and inner detector tracking is used within each RoI, which is merely $\sim$2% of the total event data. L2 will probe each RoI in an event, apply the more detailed information available, and make a decision whether the event should be passed to the EF in only 40 ms, thus reducing the event rate to 3.5 kHz.

If an event passes L2, it will be sent to the final level in the trigger system, the EF, which is software based. Unlike L1 and L2, the EF will use the full ATLAS detector information, not just in the RoIs, and include track fitting, vertexing and calculations of missing energy. With access to such detailed information from the whole ATLAS detector, the EF will take $\sim$4 s to decide whether to pass an event and reduce the event rate within the required 200 Hz.

The trigger chain is setup so that an event is only passed to the next level if it has passed the previous level. The depth of detail from the ATLAS detector is increased with each trigger level and if an event passes the EF it is written to disk to be analysed offline. Each ATLAS event recorded will be roughly 1.3 MB in size, so that at an event rate of 200 Hz and assuming a duty cycle of $\sim$40%, ATLAS will be storing around 3-4 petabytes of data each year. A worldwide network of computing sites called the LHC Computing Grid (LCG) has been established in order to store and distribute the huge amounts of data from ATLAS and the other LHC experiments.

When the LHC begins colliding protons in 2009, a new era of physics will begin. The ATLAS detector is devoted to the discovery of the Higgs boson and any new physics at the TeV scale, which is reflected in its design. The combination of precision tracking systems, excellent calorimetry and fast TDAQ should ensure that if new physics is present in the LHC collisions, ATLAS will not miss it.

Chapter 3

Phenomenology of SUSY Scenarios and Standard Model Backgrounds

The typical SUSY signature includes multiple jets and leptons from cascade decays of sparticles with large $\not{E}_T$ from massive escaping LSPs. The SUSY signature of topic in this thesis is a three lepton (electron or muon) final state, which will be more significant in certain areas of mSUGRA parameter space than others, due to varying phenomenology.

Section 3.1 introduces the points in mSUGRA parameter space that have been chosen for a trilepton analysis and describes the different phenomenology exhibited for each scenario. The SM processes that could possibly represent backgrounds to a trilepton SUSY signal are identified in Section 3.2 and, finally, a discussion of the generation of signal and background physics processes for study is presented in Section 3.3.

3.1 mSUGRA Benchmark Scenarios

In Section 1.3 it was seen that measurements of the CMBR can provide a value for the relic dark matter density of the universe and constrain mSUGRA parameter space. In the WMAP compatible areas of mSUGRA parameter space, a number of benchmark scenarios have been identified in order to address the discovery potential for SUSY at ATLAS [24]. Three benchmark scenarios are considered for the SUSY trilepton analyses presented in this thesis that vary slightly from those described in [24] but retain many of the same characteristics: SU2 (“focus point” region), SU3 (“bulk” region) and SU4 (“low mass” region). The mSUGRA parameters introduced in Sec-

Benchmark Point	SU2	SU3	SU4
mSUGRA Parameters			
m_0	3550	100	200
$m_{1/2}$	300	300	160
A_0	0	-300	-400
$\tan\beta$	10	6	10
sign(μ)	+	+	+
Cross Sections			
σ_{tot} [pb]	7.18	27.68	402.19
$\sigma_{3\ell}$ [pb]	0.07	0.30	2.49

Table 3.1: The mSUGRA parameter values and cross-sections [31] for the three SUSY benchmark points considered in this study: SU2, SU3 and SU4 (see text). Energy units are in GeV. The NLO total cross-sections and the integrated cross-sections for trilepton events have been computed with Prospino 2.0.6.

tion 1.2.3 for these benchmark scenarios can be seen in Table 3.1, together with the corresponding total and trilepton cross-sections (calculated using Prospino 2.0.6 [30]).

SUSY proposes that a left and a right-handed sfermion exists for every SM fermion, thus, twelve squarks, six charged sleptons and three sneutrinos are expected amongst the spectrum of sparticles. The three mSUGRA benchmark scenarios all exhibit different phenomenology in addition to the large variations seen in their cross-sections. Branching ratios and mass spectra have been computed for the benchmark points using Isajet 7.71 (SU2 and SU4) and Isajet7.64 (SU3), with a top-quark mass $m_t = 175$ GeV. Different versions of Isajet [32] were used for consistency with the versions used to generate the different Monte Carlo benchmark samples. The focus point region is characterised by multi-TeV masses for squarks and sleptons, a relatively light gluino, and gauginos with masses in the range of a few hundred GeV. In contrast, the bulk region yields a low mass SUSY spectrum, where all sparticles are well within the LHC energy reach. This results in SUSY events that are typically characterised by long decay chains through squarks, gauginos and sleptons. The low mass region presents even lower SUSY particle masses than for the bulk region and slightly different orderings in the mass spectrum. For all three scenarios studied, R-parity conservation is assumed and the LSP is the lightest neutralino $\tilde{\chi}_1^0$. Detailed discussions of the phenomenology at each of the three mSUGRA benchmark points can be found in Sections 3.1.1-3.1.3.

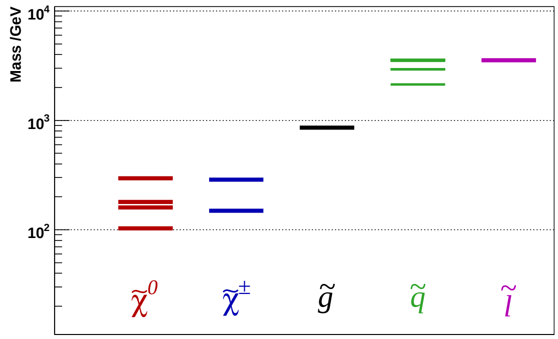

Figure 3.1: SU2 sparticle mass hierarchy (from Isajet 7.71).

	Mass [GeV]		Mass [GeV]
$\tilde{g}$	857		
$\tilde{u}_L$	3563	$\tilde{u}_R$	3574
$\tilde{d}_L$	3564	$\tilde{d}_R$	3576
$\tilde{b}_1$	2925	$\tilde{b}_2$	3501
$\tilde{t}_1$	2131	$\tilde{t}_2$	2935
$\tilde{\ell}_L$	3548	$\tilde{\ell}_R$	3548
$\tilde{\tau}_1$	3520	$\tilde{\tau}_2$	3534
$\tilde{\nu}_L$	3546	$\tilde{\nu}_\tau$	3532
$\tilde{\chi}_1^0$	103	$\tilde{\chi}_2^0$	160
$\tilde{\chi}_3^0$	180	$\tilde{\chi}_4^0$	295
$\tilde{\chi}_1^\pm$	149	$\tilde{\chi}_2^\pm$	287

Table 3.2: SU2 sparticle masses (from Isajet 7.71), where $m_{\tilde{u}} \sim m_{\tilde{c}}$, $m_{\tilde{d}} \sim m_{\tilde{s}}$, $m_{\tilde{e}} \sim m_{\tilde{\mu}} = m_{\tilde{\ell}}$ and $m_{\tilde{\nu}_e} \sim m_{\tilde{\nu}_\mu} = m_{\tilde{\nu}_L}$.

3.1.1 The Focus Point Region (SU2)

In the focus point region, a large value of m_0 generates squarks and sleptons that are too heavy to be produced at the LHC, while a moderate value of $m_{1/2}$ produces gaugino masses around a few hundred GeV. A relatively heavy gluino results in gaugino-dominated phenomenology at the focus point. The sparticle mass hierarchy for SU2 is shown in Figure 3.1 and the masses of the sparticles can be found in Table 3.2. By considering the branching ratios shown in Table 3.3, it can be seen that gaugino production at the LHC for this scenario will generally result in low-p_T multi-jet/lepton final states, due to small mass differences between the gauginos. However, if gluinos are produced at the LHC for this scenario, the typical SUSY signature of high-p_T jets will be produced in the final state.

Sparticle	Decay	BR	Sparticle	Decay	BR
$\tilde{\chi}_2^0/\tilde{\chi}_3^0$	$\tilde{\chi}_1^0 q\bar{q}$	52%	$\tilde{g}$	$\tilde{\chi}_1^\pm qq'$	4%
	$\tilde{\chi}_1^0 b\bar{b}$	14%		$\tilde{\chi}_1^\pm tb$	24%
	$\tilde{\chi}_1^0 \ell^+\ell^-$	7%		$\tilde{\chi}_2^\pm qq'$	7%
	$\tilde{\chi}_1^0 \tau^+\tau^-$	3%		$\tilde{\chi}_2^\pm tb$	20%
	$\tilde{\chi}_1^0 \nu_\ell\bar{\nu}_\ell$	13%		$\tilde{\chi}_2^0 t\bar{t}$	9%
	$\tilde{\chi}_1^0 \nu_\tau\bar{\nu}_\tau$	7%		$\tilde{\chi}_3^0 t\bar{t}$	11%
$\tilde{\chi}_4^0$	$\tilde{\chi}_1^\pm W^\mp$	82%		$\tilde{\chi}_4^0 t\bar{t}$	5%
	$\tilde{\chi}_3^0 Z$	11%			
$\tilde{\chi}_1^\pm$	$\tilde{\chi}_1^0 qq'$	67%	$\tilde{\chi}_2^\pm$	$\tilde{\chi}_2^0 W^\pm$	38%
	$\tilde{\chi}_1^0 \ell^\pm\nu$	22%		$\tilde{\chi}_3^0 W^\pm$	18%
	$\tilde{\chi}_1^0 \tau^\pm\nu_\tau$	11%		$\tilde{\chi}_1^\pm Z$	30%

Table 3.3: Dominant SU2 branching ratios for the sparticles within reach of the LHC (from Isajet 7.71).

Process	σ_{NLO} [fb]	N_{3lep} [/10 fb^{-1}]
$\tilde{\chi}_2^0\tilde{\chi}_3^0$	191.0	5
$\tilde{\chi}_3^0\tilde{\chi}_4^0$	26.4	5
$\tilde{\chi}_2^\pm\tilde{\chi}_2^\pm$	200.4	40
$\tilde{\chi}_1^\pm\tilde{\chi}_2^\pm$	46.9	5
$\tilde{\chi}_2^0\tilde{\chi}_1^\pm$	1278.7	197
$\tilde{\chi}_3^0\tilde{\chi}_1^\pm$	770.7	119
$\tilde{\chi}_4^0\tilde{\chi}_1^\pm$	43.0	6
$\tilde{\chi}_2^0\tilde{\chi}_2^\pm$	54.3	8
$\tilde{\chi}_3^0\tilde{\chi}_2^\pm$	56.5	9
$\tilde{\chi}_4^0\tilde{\chi}_2^\pm$	373.2	95
TOTAL		489

Table 3.4: SU2 NLO cross-sections for gaugino pair production (Prospino 2.0.6) and corresponding numbers of trilepton events for 10 fb^{-1}. Only gaugino pair processes with sizable contributions to a trilepton final state are given.

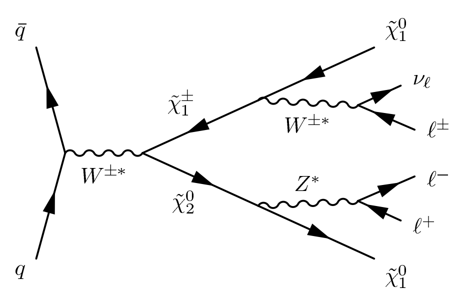

Figure 3.2: Feynman diagram of a trilepton event via direct chargino-neutralino pair production.

The focus point has a very small cross-section in comparison to the bulk and low mass regions of 7.2 pb. Direct gaugino production is responsible for 4.9 pb of the total cross-section, with gluino and gaugino-gluino production constituting the remainder. Gauginos produced directly in the LHC pp collisions may decay to trilepton final states and the leading contributions with their NLO cross-sections are shown in Table 3.4. Also listed are the expected numbers of events with trilepton final states for an integrated luminosity of 10 fb^{-1}. The dominating process for trilepton final states at SU2 is clearly direct chargino-neutralino production, for which a Feynman diagram is shown in Figure 3.2.

Recent searches for direct chargino-neutralino production and decay to trilepton final states at the Tevatron have found no excess of events compared to SM expectations. Using 2.0 fb^{-1} of data, the CDF experiment has excluded charginos with masses up to 145 GeV [33], whereas, the DØ experiment has set a lower limit of 138 GeV at 95 % CL for the chargino mass using 2.3 fb^{-1} of data [34]. Unfortunately, a direct comparison of these experimental limits with the SUSY benchmark scenarios considered in this thesis is not simple, since the mSUGRA parameter values considered by both CDF and DØ are rather different to the values chosen for study within ATLAS. For example, CDF and DØ exclude chargino masses in scenarios with tanβ = 3, whereas the ATLAS scenarios have tanβ = 6-10. A larger value of tanβ increases the branching ratio of $\tilde{\chi}_1^{\pm}$ into τ (rather than e or μ), thus reducing the theoretical $\sigma(\tilde{\chi}^0\tilde{\chi}^{\pm})\times$BR(3 leps) to a value that could be below the observed limit. Furthermore, CDF and DØ exclude chargino masses below $\sim$145 GeV for m_0 <170 GeV (m_0 for SU2 and SU4 is larger) and $m_{1/2}$ <250 GeV ($m_{1/2}$ for SU2 and SU3 is larger). All three scenarios considered here are outside of this region, and so a scenario like SU4 with a $\tilde{\chi}_1^{\pm}$ mass below that of the CDF and DØ exclusion limits cannot be ruled out.

3.1.2 The Bulk Region (SU3)

Moderate values for both m_0 and $m_{1/2}$ result in the entire spectrum of sparticles at SU3 being within the reach of the LHC. The sparticle mass hierarchy for SU3 is shown in Figure 3.3 and the masses of the sparticles can be found in Table 3.5. The bulk region offers an increased number of sparticles accessible at the LHC compared to the focus point. Consequently, the cross-section for SU3 is 27.7 pb, which is approximately four times larger than for SU2.

Direct gaugino production is not as important in the bulk region as was seen for the focus

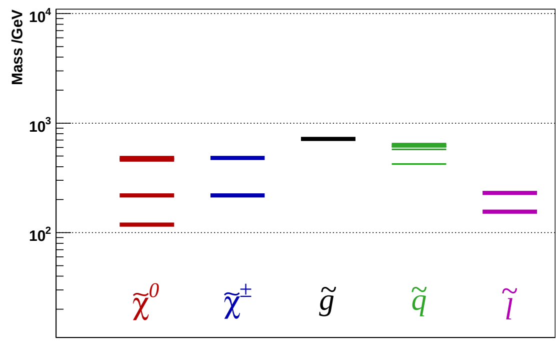

Figure 3.3: SU3 sparticle mass hierarchy (from Isajet 7.64).

	Mass [GeV]		Mass [GeV]
$\tilde{g}$	717		
$\tilde{u}_L$	632	$\tilde{u}_R$	612
$\tilde{d}_L$	636	$\tilde{d}_R$	611
$\tilde{b}_1$	575	$\tilde{b}_2$	611
$\tilde{t}_1$	424	$\tilde{t}_2$	651
$\tilde{\ell}_L$	230	$\tilde{\ell}_R$	155
$\tilde{\tau}_1$	150	$\tilde{\tau}_2$	232
$\tilde{\nu}_L$	217	$\tilde{\nu}_\tau$	216
$\tilde{\chi}_1^0$	118	$\tilde{\chi}_2^0$	219
$\tilde{\chi}_3^0$	464	$\tilde{\chi}_4^0$	481
$\tilde{\chi}_1^{\pm}$	218	$\tilde{\chi}_2^{\pm}$	480

Table 3.5: SU3 sparticle masses (from Isajet 7.64), where $m_{\tilde{u}} \sim m_{\tilde{c}}$, $m_{\tilde{d}} \sim m_{\tilde{s}}$, $m_{\tilde{e}} \sim m_{\tilde{\mu}} = m_{\tilde{\ell}}$ and $m_{\tilde{\nu}_e} \sim m_{\tilde{\nu}_\mu} = m_{\tilde{\nu}_L}$.

Sparticle	Decay	BR	Sparticle	Decay	BR	Sparticle	Decay	BR
$\tilde{\chi}_2^0$	$\tilde{\ell}_R \ell^\pm$	18%	$\tilde{\chi}_1^\pm$	$\tilde{\chi}_1^0 W^\pm$	29%	$\tilde{\ell}_L$	$\tilde{\chi}_1^0 \ell$	82%
	$\tilde{\tau}_1 \tau^\pm$	75%		$\tilde{\tau}_1 \nu_\tau$	68%		$\tilde{\chi}_2^0 \ell$	6%
	$\tilde{\nu}_L \nu_\ell$	2%	$\tilde{\chi}_2^\pm$	$\tilde{\chi}_1^0 W^\pm$	6%		$\tilde{\chi}_1^\pm \nu_\ell$	11%
	$\tilde{\nu}_\tau \nu_\tau$	2%		$\tilde{\chi}_2^0 W^\pm$	28%	$\tilde{\ell}_R$	$\tilde{\chi}_1^0 \ell$	100%
$\tilde{\chi}_3^0$	$\tilde{\chi}_1^\pm W^\mp$	61%		$\tilde{t}_1 b$	8%	$\tilde{\tau}_1$	$\tilde{\chi}_1^0 \tau^\pm$	100%
	$\tilde{\chi}_1^0 Z$	10%		$\tilde{\nu}_L \ell$	2%	$\tilde{\tau}_2$	$\tilde{\chi}_1^0 \tau^\pm$	81%
	$\tilde{\chi}_2^0 Z$	25%		$\tilde{\nu}_\tau \tau^\pm$	1%		$\tilde{\chi}_1^\pm \nu_\tau$	12%
$\tilde{\chi}_4^0$	$\tilde{\chi}_1^\pm W^\mp$	56%		$\tilde{\ell}_L \nu_\ell$	6%	$\tilde{\nu}_L/\tilde{\nu}_\tau$	$\tilde{\chi}_1^0 \nu$	100%
	$\tilde{\ell}_L \ell^\mp$	3%		$\tilde{\tau}_2 \nu_\tau$	3%	$\tilde{q}_L$	$\tilde{\chi}_2^0 q$	32%
	$\tilde{\tau}_2 \tau^\mp$	2%		$\tilde{\chi}_1^\pm Z$	25%		$\tilde{\chi}_1^\pm q'$	65%
	$\tilde{\nu}_L \nu_\ell$	6%	$\tilde{t}_1$	$\tilde{\chi}_1^0 t$	25%	$\tilde{q}_R$	$\tilde{\chi}_1^0 q$	99%
	$\tilde{\nu}_\tau \nu_\tau$	3%		$\tilde{\chi}_2^0 t$	10%	$\tilde{b}_1$	$\tilde{\chi}_2^0 b$	26%
$\tilde{g}$	$\tilde{q}_L q$	23%		$\tilde{\chi}_1^\pm b$	65%		$\tilde{\chi}_1^\pm t$	36%
	$\tilde{q}_R q$	36%	$\tilde{t}_2$	$\tilde{\chi}_1^\pm b$	27%		$\tilde{t}_1 W^\pm$	35%
	$\tilde{b}_1 b$	15%		$\tilde{\chi}_2^\pm b$	13%	$\tilde{b}_2$	$\tilde{\chi}_1^0 b$	44%
	$\tilde{b}_2 b$	9%		$\tilde{t}_1 Z$	37%		$\tilde{\chi}_1^\pm t$	12%
	$\tilde{t}_1 t$	16%		$\tilde{\chi}_2^0 t$	11%		$\tilde{t}_1 W^\pm$	32%

Table 3.6: Dominant SU3 branching ratios (from Isajet 7.64).

point region, since many more SUSY pairs may now be produced. Squarks and sleptons may now be directly produced in pp collisions as well as gauginos and gluinos. Indeed, a trilepton signal at SU3 typically originates from long coloured SUSY decay chains, where the production of intermediate sleptons is now possible. The dominant branching ratios of the sparticles at SU3 are presented in Table 3.6, where it is seen that leptons are generally produced from slepton decays, which may in turn be produced from higher gaugino, squark and gluino decays.

3.1.3 The Low Mass Point (SU4)

The SU4 benchmark point in the low mass region is defined by an even lower value for $m_{1/2}$ than SU3, but with a slightly higher value for m_0. As was seen for the bulk region, all the sparticles are within the reach of the LHC at the SU4 point. The sparticle mass hierarchy for SU4 is shown in Figure 3.4 and the masses of the sparticles can be found in Table 3.7. The SU4 scenario is rather similar to the SU3 scenario, nevertheless it is important to study since it is on the edge of current experimental limits on SUSY and could provide very early SUSY discovery channels at ATLAS.

The low mass region exhibits the largest cross-section of the mSUGRA scenarios studied of

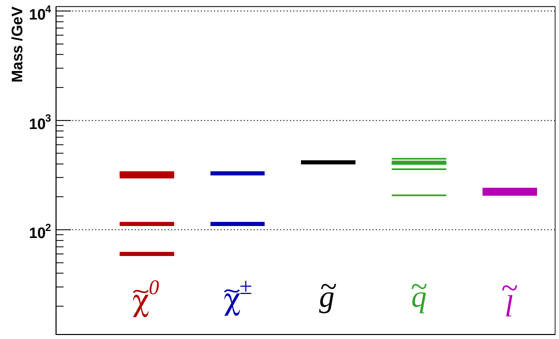

Figure 3.4: SU4 sparticle mass hierarchy (from Isajet 7.71).

	Mass [GeV]		Mass [GeV]
$\tilde{g}$	413		
$\tilde{u}_L$	412	$\tilde{u}_R$	405
$\tilde{d}_L$	420	$\tilde{d}_R$	406
$\tilde{b}_1$	358	$\tilde{b}_2$	399
$\tilde{t}_1$	206	$\tilde{t}_2$	445
$\tilde{\ell}_L$	232	$\tilde{\ell}_R$	213
$\tilde{\tau}_1$	201	$\tilde{\tau}_2$	236
$\tilde{\nu}_L$	218	$\tilde{\nu}_\tau$	216
$\tilde{\chi}_1^0$	60	$\tilde{\chi}_2^0$	113
$\tilde{\chi}_3^0$	309	$\tilde{\chi}_4^0$	328
$\tilde{\chi}_1^\pm$	113	$\tilde{\chi}_2^\pm$	327

Table 3.7: SU4 sparticle masses (from Isajet 7.71), where $m_{\tilde{u}} \sim m_{\tilde{c}}$, $m_{\tilde{d}} \sim m_{\tilde{s}}$, $m_{\tilde{e}} \sim m_{\tilde{\mu}} = m_{\tilde{\ell}}$ and $m_{\tilde{\nu}_e} \sim m_{\tilde{\nu}_\mu} = m_{\tilde{\nu}_L}$.

402.2 pb. The small differences between the sparticle mass hierarchies at SU3 and SU4 produce some variation in the open decay channels at SU4, as reflected in the branching ratios given in Table 3.8. Trilepton events from direct gaugino pair production again constitute a small fraction of the total trilepton signal for SU4, and instead will be produced predominantly by long decays through gluinos, squarks, sleptons and gauginos.

The cross-sections and expected number of trilepton events for three SUSY scenarios studied are very different. Not surprisingly, the scenario with the largest cross-section, SU4, also has the largest number of trilepton events. Direct gaugino production is the dominant process for three lepton final states for SU2, however, the branching ratio for gauginos decaying leptonically is low (on the order of a few percent). The low cross-section for SU2 combined with the low leptonic branching ratios are responsible for the smaller number of trilepton events. Although it was seen that both SU3 and SU4 share similar phenomenology, a very interesting difference in the source

Sparticle	Decay	BR	Sparticle	Decay	BR	Sparticle	Decay	BR
$\tilde{\chi}_2^0$	$\tilde{\chi}_1^0 q\bar{q}$	58%	$\tilde{\chi}_1^\pm$	$\tilde{\chi}_1^0 qq'$	65%	$\tilde{\ell}_L$	$\tilde{\chi}_1^0 \ell$	10%
	$\tilde{\chi}_1^0 b\bar{b}$	19%		$\tilde{\chi}_1^0 \ell^\pm \nu$	23%		$\tilde{\chi}_2^0 \ell$	34%
	$\tilde{\chi}_1^0 \ell^+\ell^-$	6%		$\tilde{\chi}_1^0 \tau\nu_\tau$	12%		$\tilde{\chi}_1^\pm \nu_\ell$	55%
	$\tilde{\chi}_1^0 \tau^+\tau^-$	7%	$\tilde{\chi}_2^\pm$	$\tilde{\chi}_1^0 W^\pm$	4%	$\tilde{\ell}_R$	$\tilde{\chi}_1^0 \ell$	99%
	$\tilde{\chi}_1^0 \nu_\ell\bar{\nu}_\ell$	6%		$\tilde{\chi}_2^0 W^\pm$	20%		$\tilde{\chi}_2^0 \ell$	1%
$\tilde{\chi}_3^0$	$\tilde{\chi}_1^\pm W^\mp$	62%		$\tilde{t}_1 b$	43%	$\tilde{\tau}_1$	$\tilde{\chi}_1^0 \tau^\pm$	72%
	$\tilde{\chi}_1^0 Z$	11%		$\tilde{\ell}_L \nu_\ell$	3%		$\tilde{\chi}_2^0 \tau^\pm$	11%
	$\tilde{\chi}_2^0 Z$	20		$\tilde{\tau}_2 \nu_\tau$	2%		$\tilde{\chi}_1^\pm \nu_\tau$	17%
$\tilde{\chi}_4^0$	$\tilde{\chi}_1^\pm W^\mp$	60%		$\tilde{\chi}_1^\pm Z$	16%	$\tilde{\tau}_2$	$\tilde{\chi}_1^0 \tau^\pm$	21%
	$\tilde{\nu}_L \nu_\ell$	5%	$\tilde{t}_1$	$\tilde{\chi}_1^\pm b$	100%		$\tilde{\chi}_2^0 \tau^\pm$	31%
	$\tilde{\nu}_\tau \nu_\tau$	3%	$\tilde{t}_2$	$\tilde{\chi}_1^\pm b$	25%		$\tilde{\chi}_1^\pm \nu_\tau$	48%
$\tilde{g}$	$\tilde{b}_1 b$	47%		$\tilde{\chi}_2^\pm b$	13%	$\nu\ell$ / ν_τ	$\tilde{\chi}_1^0 \nu$	19%
	$\tilde{b}_2 b$	4%		$\tilde{t}_1 Z$	43%		$\tilde{\chi}_2^0 \nu$	23%
	$\tilde{t}_1 t$	42%		$\tilde{\chi}_1^0 t$	3%		$\tilde{\chi}_1^\pm \ell^\pm/\tau^\pm$	58%
$\tilde{q}_L$	$\tilde{\chi}_2^0 q$	32%		$\tilde{\chi}_2^0 t$	8%	$\tilde{b}_2$	$\tilde{\chi}_1^0 b$	27%
	$\tilde{\chi}_1^\pm q'$	64%	$\tilde{b}_1$	$\tilde{\chi}_2^0 b$	28%		$\tilde{\chi}_2^0 b$	9%
$\tilde{q}_R$	$\tilde{\chi}_1^0 q$	98%		$\tilde{\chi}_1^\pm t$	22%		$\tilde{\chi}_1^\pm t$	8%
	$\tilde{\chi}_2^0 q$	2%		$\tilde{t}_1 W^\pm$	46%		$\tilde{t}_1 W^\pm$	52%

Table 3.8: Dominant SU4 branching ratios (from Isajet 7.71).

of the trileptons is found for SU3. About 80% of the trilepton events for SU3 contain at least one $\tilde{\tau}$ and this is attributed to the slightly varying mass spectra in the two scenarios ($m_{\tilde{\chi}_2^0} > m_{\tilde{\chi}_1^\pm} > m_{\tilde{\tau}_1}$ in SU3, $m_{\tilde{\tau}_1} > m_{\tilde{\chi}_2^0} \simeq m_{\tilde{\chi}_1^\pm}$ in SU4) allowing different decay modes for SU3. At the focus point, the allowed decays are very different since only the gluino and gauginos will be within reach of the LHC.

Two different definitions of a trilepton signal will be considered for the SUSY trilepton analysis presented in this thesis: an inclusive trilepton signal, where all trilepton final state SUSY events are counted as “signal”; and an exclusive trilepton signal, where only direct gaugino production and decay to a trilepton final state will be counted as “signal”. Since direct gaugino production does not constitute sizable components of the cross-sections at SU3 and SU4, only the SU2 benchmark scenario will be studied for the exclusive trilepton analysis. All three SUSY benchmark scenarios presented in this chapter will be studied for the inclusive trilepton analysis.

3.2 Standard Model Backgrounds

A variety of processes exist in the SM that can produce three or more leptons in the final state and will all be regarded as backgrounds to a SUSY trilepton signal. The SM processes considered as backgrounds for the trilepton SUSY analyses presented in this thesis are $t\bar{t}$, Zb, $Z\gamma$, ZW, ZZ and WW. Examples of Feynman diagrams for each SM background process are presented in Figure 3.5, and the cross-sections for each SUSY and SM sample used for the trilepton analyses in this thesis are listed in Table 3.9. SM backgrounds that produce zero or one lepton final states have not been considered as potential backgrounds, as the probability for two or more leptons to be faked in the event is negligible. Further details concerning data samples and analysis procedure can be found in Appendix A.

The cross-section for $t\bar{t}$ production is the highest of all the SM backgrounds considered for a trilepton SUSY analysis. Top-quark pairs may produce two prompt leptons via leptonic t and $\bar{t}$-quark decays, as shown in Figure 3.5(a). A third lepton may be produced from a leptonic b or $\bar{b}$-quark decay, or may be a faked by one of the numerous jets in the event. The $t\bar{t}$ sample used for the trilepton analyses in this thesis has been filtered at generator level to ensure at least one of the t-quarks decays leptonically.

The SM process Z+jets has been considered as a background to the trilepton signal, however, the official ATLAS sample includes unsuitable generator level filters (at least four jets having $p_T >$ 80, 40, 40, 40 GeV and $\not{E}_T$ >80 GeV) and so could not be used for a trilepton analysis. Since leptonically decaying b-quarks will be a larger source of fake leptons than light quarks, a sub-sample of Z+jets events with b-quark production is deemed to be a suitable substitution. It is reasonable to assume that the level of background to a trilepton SUSY signal from Z+jets will be roughly the same order as the background from Z+b-quark jets, since the dominating source of fake leptons is from the b-quark jets. The cross-section for Z+b-quark jets production, referred to here as Zb, will be large at the LHC and the b-quark may be either a fragment of the incoming event or from the hard process itself [35]. In Zb events, two leptons are produced via a leptonic Z decay, while the third lepton may either be from a leptonic b-quark decay as shown in Figure 3.5(b), or faked by a jet. The Zb sample used for the trilepton analyses in this thesis has been filtered at generator level to ensure the presence of at least one electron or muon in the final state with p_T >10 GeV and $|\eta|$ <2.8.

Diboson SM process have much smaller production cross-sections in comparison to $t\bar{t}$ and

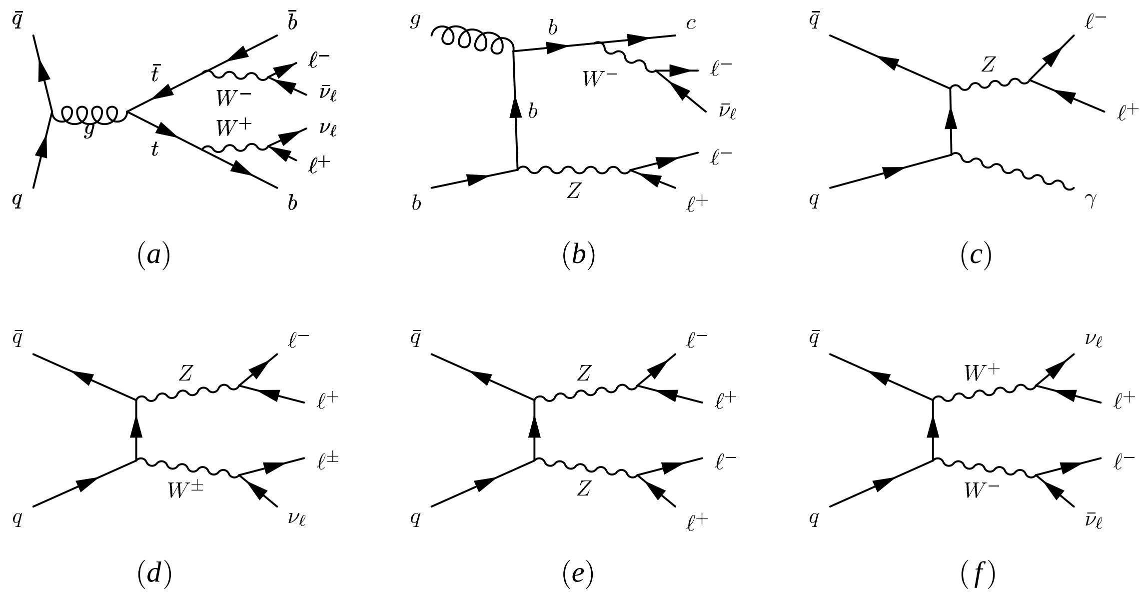

Figure 3.5: Feynman diagrams of SM processes with possible trilepton final states; $t\bar{t}$ (a), Zb (b), $Z\gamma$ (c), ZW (d), ZZ (e) and WW (f).

Process	Generator	σ_{LO} [pb]	$\sigma_{LO} \times \varepsilon_F$	k	$\sigma_{NLO} \times \varepsilon_F$ [pb]	$\int \mathcal{L}dt$ [fb^{-1}]
SU2	Herwig	5.2	5.2	1.39	7.2	6.9
SU3	Herwig	20.9	20.9	1.33	27.7	17.1
SU4	Herwig	294.5	294.5	1.37	402.2	0.5
$t\bar{t}$	MC@NLO	833.0	449.8	1.00	449.8	1.0
Zb	AcerMC	205.0	153.8	1.00	163.9	0.8
ZZ	Herwig	11.0	2.1	1.88	3.9	12.7
ZW	Herwig	27.0	7.8	2.05	16.1	3.0
WW	Herwig	70.0	24.5	1.67	40.9	1.2
$Z\gamma$	Pythia	3.8	2.6	1.30	3.4	3.0

Table 3.9: The SUSY and SM samples used for the trilepton analyses along with their Monte Carlo generators. The LO total cross-sections, with and without taking into account the generator filter efficiency ε_F as well as the NLO k-factors used to rescale the cross-sections are shown (for the SUSY samples, both LO and NLO numbers are from Prospino 2.0.6) (from [31]). Samples with k =1 correspond to samples that were generated to NLO. The NLO cross-sections with filter efficiency applied are shown in the $\sigma_{NLO} \times \varepsilon_F$ column. The integrated luminosities corresponding to the total statistics in each sample are given in the last column.

Zb, however, they are regarded as very important SM backgrounds to a SUSY trilepton signal as they can produce multiple prompt leptons in the final state. Feynman diagrams for $Z\gamma$, ZW, ZZ and WW production at the LHC are presented in Figures $3.5(c)-(f)$ respectively. The Z bosons may decay to two prompt leptons, the W bosons may decay to a prompt lepton and its associated neutrino and the γ may pair-produce two leptons or be misidentified as a lepton. In this manner, ZZ production may produce four lepton final states, ZW production may yield three lepton final states and $Z\gamma$ production yield at least two lepton final states. There is a striking similarity between ZW and direct gaugino SUSY trilepton events in Figure $3.5(d)$ and Figure 3.2, suggesting ZW could be a dangerous background for the exclusive SUSY trilepton signal. Although WW production may at most produce only two prompt leptons, it has been considered as a background to a trilepton signal, since a third lepton could be faked by the proton remnants. The $Z\gamma$ background sample has been filtered at generator level to include a γ with $p_T >$25 GeV and $|\eta| <$2.7. It is noted that this filter could exclude a small number of $Z\gamma$ events which may contribute to a trilepton signal, although this is unlikely to change the conclusions of the trilepton analyses presented in this thesis. The ZZ, ZW and WW background samples include contributions from off-shell-mass bosons and are all filtered at generator level to include at least one electron or muon in the final state with $p_T >$10 GeV and $|\eta| <$2.8. The k-factors applied to the diboson samples in Table 3.9 take into account interference with the photon pole [31].

All SUSY and SM processes required for the trilepton analyses presented here have been prepared using various Monte Carlo generators (see Section 3.3 for further details) followed by the application of the full ATLAS detector description to yield samples that are "fully simulated". The events have been simulated assuming no overlapping proton collisions ("pile-up").

3.3 Monte Carlo Generators

The simulation of high-energy particle physics events is performed by Monte Carlo (MC) generators, which use random numbers to compute the results of a particle interaction or decay. An assortment of MC generators currently exist for LHC physics simulation and are chosen according to their suitability for the physics process in hand. The MC generators used for the MC samples used in this thesis are listed in Table 3.9. These were generated centrally within the ATLAS Collaboration as part of the the ATLAS Computing System Commissioning (CSC) data challenge.

MC generators use a parton model of the proton, where the momentum sharing amongst the partons follows a pdf. Random numbers are used as inputs to the parton model (or any initial state) to describe the hard process required by the user. Most MC generators will also include in their simulation a description of the initial state radiation (ISR), the underlying event (everything except the two outgoing hard scattered jets), resonance decays, soft processes, final state parton showers and hadronisation. A few MC generators can calculate the NLO description of a physics process.

PYTHIA [36] is a widely used MC generator that is capable of describing the hard physics process of an event as well as all the currently known surrounding behaviours. PYTHIA provides very detailed and complete events of physics processes and was used to generate the $Z\gamma$ background sample.

The SUSY samples were made using a series of MC programs that are able to calculate the weak-scale parameters from the mSUGRA parameters of the benchmark points. Isajet [32] includes dedicated subroutines that find the phenomenology of a point in SUSY parameter space. The SUSY masses and branching ratios of the three mSUGRA benchmark points were obtained using Isajet (different versions according to when the benchmark point was defined). PROSPINO [30] is a LO and NLO SUSY production cross-section calculator. Using the SUSY masses and branching ratios obtained from Isajet as input, the LO and NLO cross-sections for the three SUSY benchmark points were obtained using PROSPINO.

HERWIG (Hadron Emission Reactions With Interfering Gluons) [37] [38] was used to generate the main events for the SUSY signal samples and the ZZ, ZW and WW samples. In the case of the SUSY samples, the sparticle masses and branching ratios found from Isajet were used as input for HERWIG. The LO cross-sections as calculated from HERWIG were used for the diboson samples and rescaled to NL0 cross-sections using k-factors. For the SUSY samples, however, the NLO cross-sections as calculated from PROSPINO were used instead. HERWIG alone does not describe the entire event and so JIMMY [39] is also used for the description of the underlying event and multiple parton scattering events.

To generate $t\bar{t}$ events, MC@NLO (Monte Carlo At Next to Leading Order) [40] [41] was used. MC@NLO makes use of the HERWIG and JIMMY event generators to generate events with full QCD NLO corrections. A dedicated MC program for the generation of SM background processes in pp collisions at the LHC, AcerMC [42] was used to make the Zb sample. AcerMC only generates the hard physics process and so the entire event is completed for the Zb sample by ISR, hadronisation and decays from PYTHIA. To take into account the possibility of destructive interference, the $t\bar{t}$ and Zb samples contain events with both positive and negative weighting. This weighting has been appropriately treated in the analysis.

It should be noted that the diboson samples generated by HERWIG are unlikely to accurately represent the true behaviour of diboson events if high-p_T jets are required in an analysis (as in Section 5.2), since Herwig generates these events to leading order only, using parton showers. A more suitable MC generator for diboson events with high-p_T jets would be MC@NLO, which has an improved description of jets from the underlying event. Unfortunately, the official ATLAS diboson MC@NLO samples were unsuitable, as the bosons were all on-shell-mass and the irreducible background to SUSY trilepton events is likely to originate from off-shell-mass bosons. Therefore, the use of diboson samples with the full Zγ interference structure is necessary, which is provided by HERWIG and not by MC@NLO.

The resulting events from MC generators are as would be seen by a “perfect” detector. To provide more realistic models of what may be seen in the ATLAS detector, a simulation of the interactions of the final state particles with matter is performed by GEANT [43]. Thus, fully simulated physics processes may be studied by following MC event generation with a full detector simulation. Fully simulated events may then be used within the Athena software framework of the ATLAS Collaboration [44], where physics objects and event variables are reconstructed by dedicated algorithms.

Chapter 4

Particle Reconstruction in the ATLAS Detector

4.1 Physics Object Definitions

Each subsystem of the ATLAS detector described in Chapter 2 has a key role to play in particle identification. The criteria used here to define relevant particle objects (electrons, muons, photons and jets) are those recommended by ATLAS for the CSC exercise [31] and are summarised in Table 4.1. All these criteria will be collectively referred to as the "preselection" in the following. The 10 GeV threshold for the lepton transverse momentum p_T is a compromise between the need to have reasonable lepton acceptance at relatively low p_T values, which is of importance for the trilepton analysis, and the requirement to keep the contamination from non-prompt leptons to an acceptable level. The format of data used here is "Analysis Object Data" (AOD), where particle objects are loosely reconstructed and grouped into "containers". The same object may be reconstructed by two or more particle identification algorithms, and so be present in more than one container within the AOD (e.g. an object may be loosely reconstructed as an electron and a jet, and so be in both the electron and jet containers). To avoid double counting an object, "overlap removal" is performed for containers in the AOD. More details on object selections and the procedure for overlap removal between object containers are given below.

Tracks

As charged particles move through the inner detector they ionise the surrounding material, re-

	Muon	Electron	Jet
Collection Key	`StacoMuon-Collection`	`Electron-Collection`	`Cone4Tower-ParticleJets`
p_T	$>$10 GeV	$>$10 GeV	$>$10 GeV
η	$\lvert\eta\rvert < 2.5$	$0 < \lvert\eta\rvert < 1.37$ or $1.52 < \lvert\eta\rvert < 2.5$	$\lvert\eta\rvert < 2.5$
Calorimeter Isolation	$\lvert E\rvert <$10 GeV in ΔR =0.2	$\lvert E\rvert <$10 GeV in ΔR =0.2	-

Table 4.1: Summary of criteria used to define particle objects relevant for the trilepton analysis. Technical details are discussed in main text.

sulting in several "hits" in the tracking subsystems. These hits within the multiple layers of the tracking system are associated to each other by tracking algorithms to reconstruct the path of the charged particle as a track.

Clusters

Clusters are energy deposits in the electromagnetic and hadronic calorimeters. The algorithm used to build calorimeter clusters is the "sliding-window" algorithm [45], which sums calorimeter cells within fixed size rectangular windows. Firstly, calorimeter towers are built in bins of size $\Delta\eta \times \Delta\phi = 0.025 \times 0.025$ in the ECAL, and size $\Delta\eta \times \Delta\phi = 0.1 \times 0.1$ in the HCAL and the energy deposits are summed longitudinally within the towers. The sliding window is moved in the tower grid to find a local maximum in E_T and a precluster is formed. These preclusters act as seeds to a cluster, where the cluster size is dependent on the location of the cluster and the hypothesis of the particle type.

Muons

A muon passing through the entire detector will leave its mark in all of the subsystems: in the inner detectors, in the electromagnetic and hadronic calorimeters, and in the muon spectrometers. The identification and measurement of muons incorporates information from each of the subsystems, where for each stage of the muon reconstruction there are multiple algorithms that may be used. The details of each individual algorithm will not be discussed here, instead a broad overview will be given that will summarise the stages of muon reconstruction.

The first stage of muon identification is to find a track in the muon spectrometer. A track is found from segments in the separate muon spectrometer modules using segment pattern recognition and global spectrometer track tracing through the magnetic field. Track fitting is performed to extract a first rough measurement of the momentum. The track is back propagated to the inner detector to check the track points roughly towards the interaction point. The second stage of muon identification is to find a track in the inner detector. This is done using the same algorithms as discussed earlier in track reconstruction.

The third stage of muon identification is to combine the muon spectrometer and inner detector tracks. As previously stated, there are multiple ways to combine the tracks. The algorithm used here is STACO (STAtistical COmbination) [46], which statistically merges the independently found tracks to obtain a chi-squared value that can be used to assess the success of the matching. The fourth and final stage of muon identification is to correct for energy losses in the calorimeters (usually at least 3 GeV), which causes the the measured momentum in the spectrometer to differ from the initial momentum of the muon. For "low-p_T" muons ($\lesssim$ 100 GeV) the better momentum measurement is found using the inner detector, whereas the muon spectrometer is used for "high-p_T" ($\gtrsim$ 100 GeV) momentum determination. In general, combining the measurements yields the best momentum measurement.

Muons are taken from the `StacoMuon` container in the AOD and in this analysis, only muons with $p_T > 10$ GeV and $|\eta| < 2.5$ reconstructed by the `HighPt` algorithm, are used. All candidate muons must be combined tracks from muon spectrometer and inner detector tracks (`combinedMuon`), with the χ^2 of the track-matching fit taking values smaller than 100. The muons are required to be isolated, such that the total transverse energy in a cone of radius $\Delta R = \sqrt{(\Delta\eta)^2 + (\Delta\phi)^2} = 0.2$ in the calorimeter around the muon is required to be less than 10 GeV. The isolation of $E_T < 10$ GeV in a cone of $\Delta R = 0.2$ is a standard lepton isolation cut and achieves reasonable lepton identification efficiencies and fake rates [31]. It should be noted that lepton isolation could be optimised for future leptonic SUSY searches.

Electrons

An electron will pass through the first two main layers of the ATLAS detector: leaving a track in the inner detector and an energy deposit in the electromagnetic calorimeter. The identification and measurement of electrons is performed by two main algorithms. The first is the standard electron algorithm which is optimised for the reconstruction of isolated, high-p_T electrons and is seeded by a cluster in the electromagnetic calorimeter. The second is a low p_T algorithm which is optimised for reconstructing the non-isolated, low-p_T electrons originating from a b-quark and is seeded by a track in the inner detector. The standard algorithm is used for electron reconstruction in this thesis.

The first stage of electron identification is to find a cluster in the electromagnetic calorimeter using the sliding window algorithm. The second stage is to match the cluster to a track in the inner detector. This matching is performed in two steps: firstly the η, ϕ and energy/momentum ratio E/p of the track and cluster are compared and must satisfy $\Delta\eta < 0.05$, $\Delta\phi < 0.1$ and $E/p < 10$. Then the inner detector track is extrapolated to the calorimeter position of each compartment in depth and the η and ϕ comparisons at each depth must satisfy $\Delta\eta < 0.025$ and $\Delta\phi < 0.05$. The larger $\Delta\phi$ constraints compared to the $\Delta\eta$ are to take into account any possible effects from emission of photons (bremsstrahlung).

Electron identification makes use of a number of variables which can distinguish between electrons and background hadrons. These discriminating variables are both from the calorimeters and the inner detector and are optimised for multiple bins in η, as seen in Table 4.2. Electrons will deposit very little of their energy in the HCAL compared to jets and so hadronic leakage (the ratio of the energy deposited in the first compartment of the HCAL to the energy of the electron) is a good discriminator against jet background. The lateral shower shape of the electron in the second compartment of the ECAL can be used to discriminate against high energy pions and jets with wide showers. The first compartment of the ECAL has very fine granularity and can be used to identify any substructure within the shower coming from isolated pions or photons. The inner detector is used to require constraints on the electron track which reduces the remaining background from photon conversions and jets containing high-p_T pions. The track must be of good quality and point towards a ECAL cluster, in addition to having a good energy-momentum match to the considered cluster. All electrons must pass these series of identification cuts based on the shower shape properties in different compartments of the calorimeter as well as variables combining inner detector and calorimeter information. The result of the combination of all these cuts is contained in the `isEM` flag of the egamma algorithm, where different levels of electron identification may be chosen by a user e.g. "tight", "medium", "loose".

In this analysis, electrons are taken from the `Electron` container, with $p_T > 10$ GeV and $|\eta| < 2.5$ and only electrons reconstructed by the standard algorithm are used. Candidate electrons must fulfil the "medium" electron shower shape quality requirements. Electrons must be isolated, with the total transverse energy in a cone of radius $\Delta R = 0.2$ around the electron required to be less than 10 GeV. Events with electrons that pass the p_T, η and isEM constraints in the "crack region" (the ECAL barrel-end-cap transition, where $1.37 < |\eta| < 1.52$) are rejected.

Description	Variable	Cut
Hadronic Leakage		
Ratio of E_T in the 1^{st} sampling of the hadronic calorimeter to E_T of the EM cluster	$R_{had} <$	0.015-0.045
First Layer of EM Calorimeter		
Ratio of 1^{st} sampling energy to the EM cluster energy	$f_1 <$	0.005
2^{nd} largest energy deposit normalised to the cluster energy	$\Delta E_{max2} <$	0.25-0.53
Difference between energy of second largest energy deposit and energy of minimal value between the 1^{st} and 2^{nd} maxima	ΔE [GeV] $<$	0.10-0.30
Total shower width	$\omega_{tot} <$	1.40-4.00
Shower width using three strips around the one with the maximal energy deposit	$\omega_{3strips} <$	0.60-0.80
Fraction of energy outside core of three central strips but within seven strips	$F_{side} <$	0.20-0.48
Second Layer of EM Calorimeter		
Ratio in η of cell energies in 3×7 versus 7×7 cells	$R_\eta(37) >$	0.60-0.91
Lateral shower width	$\omega_2 <$	0.0125-0.0200
Track Quality		
Number of hits in b-layer	$N_{BL} >=$	1
Number of hits in pixel-layer	$N_{Pi} >=$	1
Number of hits in pixel+SCT	$N_{Si} >=$	9
Transverse impact parameter	d_0 [cm] $<$	0.1
Difference between the cluster η and the η of the track	$\Delta\eta <$	0.005
Difference between the cluster ϕ and the ϕ of the track	$\Delta\phi <$	0.02
Ratio of the cluster energy and the track momentum	E/p min	0.9
	E/p max	2.5-3.5

Table 4.2: Electron identification cuts used in this thesis. Ranges are given for variables that are optimised for seven bins in η (from [47]).

This is due to a feature in the reconstruction software used in the data presented here where the isolation variable is known to perform poorly in the crack region.

Jets

Hadronic particles will pass through the first three main layers of the ATLAS detector, leaving tracks in the inner detectors if charged and energy deposits in the electromagnetic and hadronic calorimeters. Jet constituents are identified using calorimeter tower signals in bins of size $\Delta\eta \times \Delta\phi = 0.1 \times 0.1$, where energy deposits are summed longitudinally within the towers.

The identification and measurement of jets is performed by two main algorithms, the "cone algorithm" and the "Kt algorithm" [31], whose role is to take the jet constituents and associate clusters of them into jets. The Kt jet finder algorithm is an “aggregative” algorithm, adding jet constituents together to form a jet. However, the cone algorithm is used here, which is a geometric jet finder algorithm that uses high-E_T particles in the event as the starting points to seed jets. Cone jets are simply a collection of particles within a cone of given radius ($\Delta R = 0.4$ is used here), where the cone axis must be aligned with the four-momentum of the jet. The cone finder algorithms require and use a “split-merge” procedure to define non overlapping exclusive jets, thus preventing situations where a single particles belong to more than one jet.

In the analysis presented here, jets are taken from the `Cone4Tower` collection in the AOD, with $p_T > 10$ GeV and $|\eta| < 2.5$. Jets overlapping with electrons within a cone of radius $\Delta R = 0.2$ are removed from the jet list (while the overlapping electrons are kept).

Missing Transverse Momentum

The Missing Transverse Momentum is calculated from the energy deposited in all of the calorimeter cells and from the tracks in the muon spectrometer, with a correction made for the energy lost in the cryostat, as discussed in Section 2.2.5. A refined calibration of the $\not{E}_T$ is used in this dissertation where calorimeter cells are associated with an identified object. In this manner the $\not{E}_T$ reconstruction is improved, since the calibration of identified objects will be known more accurately than a global calibration.

Further Object Identification/Discrimination Issues

To reduce the number of electron and muon pairs from backgrounds such as low-mass Drell-Yan or low-mass hadron decay, “Same Flavour Opposite Sign” (SFOS) lepton pairs that give an invariant mass M_{SFOS} smaller than 20 GeV are removed from the electron/muon candidate lists. Leptons originating from heavy quark decays will naturally be produced geometrically close to a jet, or within the jet itself. In order to suppress the contribution from non-primary leptons, electrons and muons within $\Delta R < 0.4$ of a jet are removed from the respective candidate lists. Because electrons are chosen to take precedence over jets in the case of an ambiguous particle identification, while no muon-jet overlap removal is applied at the preselection level, the overall effect of this additional cut is to suppress more muons than electrons when the lepton originates from a b-quark. This asymmetrical treatment of electrons and muons is one of the main causes of the differences seen in electron and muon fake rates, which is discussed in the following section.

4.2 Lepton Efficiencies and Fake Rates

Any analysis that looks for leptonic final states will require a good understanding of lepton reconstruction efficiency and identification. Indeed, the high lepton multiplicity required for the trilepton analysis increases the need for a high lepton reconstruction efficiency as well as a high purity for lepton identification.

The efficiencies and fake rates for electrons and muons have been studied for the preselection described in Section 4.1, using "fully simulated" MC samples of the three SUSY benchmark points discussed in Section 3.1 and the $t\bar{t}$ production with semi-leptonic and fully leptonic top decay modes. The $t\bar{t}$ sample is studied as it is the dominant background for many leptonic SUSY analyses, hence the reduction of lepton-jet misidentification will be important. The $t\bar{t}$ sample also provides a good benchmark scenario for non-isolated leptons.

Methods have been developed with the ATLAS experiment to obtain lepton efficiencies and fake rates from data (e.g."Tag and Probe" [31], [48]). However, in this study, generator level information is used to study how the lepton reconstruction algorithms perform for the ATLAS detector across physics samples. Generator leptons are found with $|\eta| < 2.5$ and $p_T > 12$ (8) GeV for the efficiency (fake rate) calculation. A 2 GeV difference is used for the p_T of the generator level leptons compared to reconstructed leptons to take into account any momentum resolution effects. Since the lepton reconstruction algorithms are tailored to primary leptons from high-mass decays, only stable generator leptons from $W^{\pm}$, Z, τ or SUSY decays are considered. Generator level isolation is calculated by summing the transverse energies of the stable, interacting particles in a cone around a generator level particle. For consistency with the isolation requirement for reconstructed leptons, generator level isolation of $E_T < 10$ GeV in a cone of $\Delta R = 0.2$ is required for the generator leptons in the efficiency calculation. Isolation is not required for the generator leptons in the fake rate calculation, since non-isolated leptons are not considered a source of lepton fakes. In order to compare the reconstructed and generator level leptons, geometrical matching is performed between the two objects with a maximum separation of $\Delta R = 0.02$.

The definitions for lepton efficiency (ε_{lep}) and lepton fake rate (f_{lep}) given below are consistent with those recommended by the ATLAS performance groups [31]. Lepton efficiency is defined as:

$$\varepsilon_{lep} = \frac{N_{MC}^{m}(lep)}{N_{MC}^{all}(lep)}, \tag{4.1}$$

	Efficiency (%)		Fake Rate($\times 10^{-3}$)	
	Electrons	Muons	Electrons	Muons
SU2	66.6±0.5	76.7±0.5	2.12±0.10	0.51±0.05
SU3	69.1±0.2	71.8±0.1	2.23±0.03	0.24±0.01
SU4	67.0±0.2	72.1±0.2	3.02±0.05	0.88±0.03
$t\bar{t}$	68.4±0.1	74.2±0.1	4.32±0.04	1.61±0.02

Table 4.3: Lepton efficiencies and fake rates for the three benchmark SUSY samples and $t\bar{t}$ events.

and lepton fake rate is defined as:

$$f_{lep} = \frac{N_{rec}^{no-m}(lep)}{N_{MC}^{all}(jet)}, \tag{4.2}$$

where $N_{MC}^{m}(lep)$ is the number of generator level leptons matched to a reconstructed lepton; $N_{MC}^{all}(lep)$ is the total number of generator level leptons kinematically consistent with the reconstruction algorithms; $N_{rec}^{no-m}(lep)$ is the number of reconstructed leptons that do not have a match to a generator level lepton; and $N_{MC}^{all}(jet)$ is the total number of generator level jets with $|\eta| < 2.5$ and $p_T > 10$ GeV.

The global lepton efficiencies and fake rates obtained for the SUSY and $t\bar{t}$ samples are shown in Table 4.3 for electrons and muons separately, while the differential efficiencies and fake rates as a function of p_T and $|\eta|$ are presented in Figure 4.1 and Figure 4.2 for electrons and muons, respectively. It is seen in Figures 4.1$(a)-(b)$ and Figures 4.2$(a)-(b)$ that the electron and muon differential efficiencies are degenerate across all samples, however, this is not the case for the global lepton efficiencies in Table 4.3. Many reasons exist for the discrepancies observed in the global lepton efficiencies, one being that the lepton p_T or η spectra in each sample could tend towards different regions with intrinsically higher or lower efficiency. In comparing Figure 4.1(a) with Figure 4.2(a) it is seen that the electron efficiency as a function of p_T increases with p_T, whereas the muon efficiency appears to decrease. As discussed in Section 4.1, tracks in the muon spectrometer are relied upon for the measurement of very high p_T muons, which are less accurate than using tracks in the inner detector, and so the efficiency falls slightly for high-p_T muons. The electron and muon efficiencies also display different behaviours as a function of $|\eta|$, as seen in Figure 4.1(b) and Figure 4.2(b). Electron reconstruction efficiency experiences a drop for $1.37 < |\eta| < 1.52$ due to the ECAL barrel-end-cap transition and at high $|\eta|$ because of worse tracking performance in the forward regions. In contrast, muon reconstruction efficiency rises steadily with increasing $|\eta|$, as detector coverage is poor at low $|\eta|$.

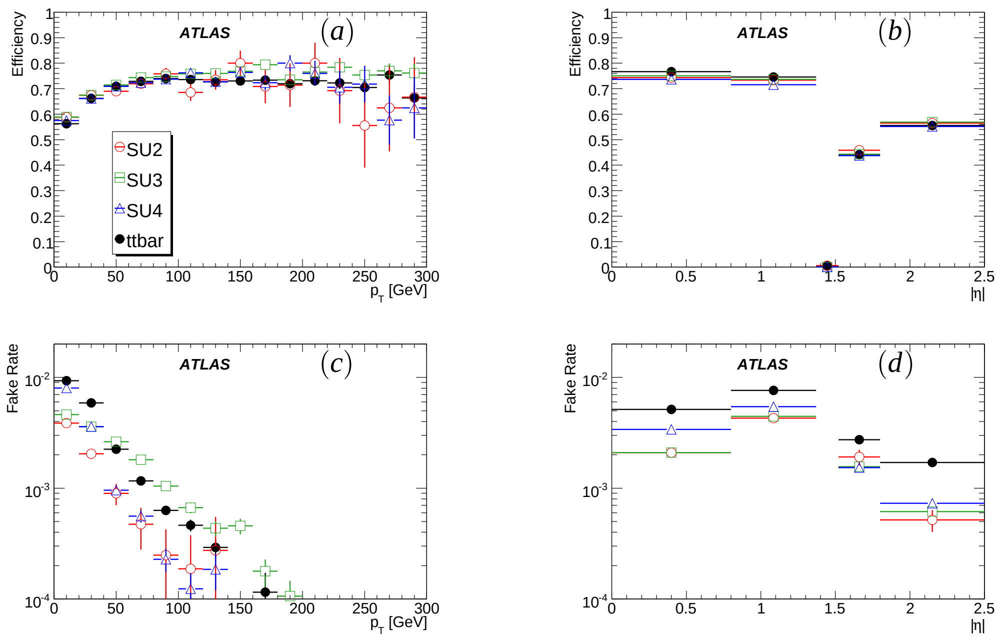

Figure 4.1: Electron reconstruction efficiencies (vs p_T (a), vs $|\eta|$ (b)) and fake rates (vs p_T (c), vs $|\eta|$ (d)) for SU2 *(open circles)*, SU3 *(open squares)*, SU4 *(open triangles)*, and $t\bar{t}$ *(solid circles)*.

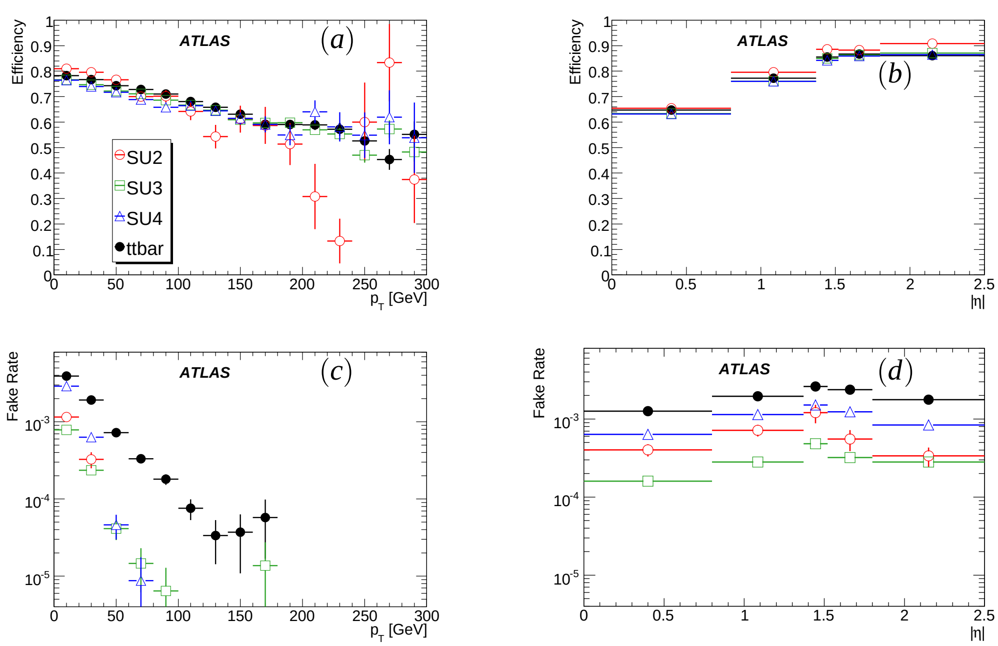

Figure 4.2: Muon reconstruction efficiencies (vs p_T (a), vs $|\eta|$ (b)) and fake rates (vs p_T (c), vs $|\eta|$ (d)) for SU2 *(open circles)*, SU3 *(open squares)*, SU4 *(open triangles)*, and $t\bar{t}$ *(solid circles)*.

	% of 3-lep events with				% of 3-lep events where		
	N_l^{fake}=0	N_l^{fake}=1	N_l^{fake}=2	N_l^{fake}=3	$1^{st}\ell$ is fake	$2^{nd}\ell$ is fake	$3^{rd}\ell$ is fake
SU2	87.7	12.3	0.0	0.0	1.3	3.8	7.2
SU3	84.4	10.8	0.8	0.0	1.6	3.3	7.5
SU4	69.9	27.5	1.9	0.6	2.7	8.0	22.5
$t\bar{t}$	1.5	79.4	18.9	0.2	6.9	29.8	81.1

Table 4.4: Proportions of fake leptons in trilepton events for the three benchmark SUSY samples and $t\bar{t}$ events, where N_l^{fake} is the number of fake leptons amongst the three leading leptons, as defined by Equation 4.2.

Both SU2 and SU3 exhibit similar behaviour in their global fake rates, while SU4 and $t\bar{t}$ display higher values, as seen in Table 4.3. This is attributed to the higher average number of b-quark jets in SU4 and $t\bar{t}$ (∼1.6 and ∼1.8 b-quark jets per event, respectively) compared to the SU2 and SU3 samples (∼0.4 and ∼0.6 b-quark jets per event, respectively). It is also observed that SU3 displays a lower muon fake rate than seen for SU2, although the SU3 muon fake rate as a function of p_T plotted in Figure 4.2(c) does not look too different from SU2. This is because the p_T spectra of the b-quark jets in the SU3 sample is shifted towards higher values compared to the other samples. Since lepton fake rate drops off with increasing p_T, higher p_T jets are less likely to fake leptons and so the overall muon fake rate for SU3 is reduced. Muons are more affected by this difference in b-quark jet p_T spectra since the muon fake rate vanishes far more rapidly with increasing p_T than for electrons, as seen when comparing Figure 4.2(c) with Figure 4.1(c). The general trend for muon fake rates to be roughly an order of magnitude lower than those for electrons is attributed to the asymmetrical treatment of electrons and muons as discussed in Section 4.1.

It is important to measure lepton fake rates in both SUSY and SM background events so that the contribution of "faked trilepton" events from both sources can be understood. The percentage of trilepton events with fake leptons is presented in Table 4.4, where it is seen that ∼70-90% of SUSY trilepton events are comprised of three real leptons, depending on the benchmark scenario considered. In contrast, only ∼2% of $t\bar{t}$ trilepton events are comprised of three real leptons, with nearly 70% of the trilepton events involving one faked lepton. Also included in Table 4.4 are the percentage of events where the first (leading in p_T), second, or third leptons are fake leptons. Across all samples it is seen that it is the third lepton that is responsible for the majority of "faked trilepton" events. In Figure 4.1(c) and Figure 4.2(c) it was seen that the largest fake rates for electrons and muons respectively were in the low p_T regions, which is supported by the higher percentage of trilepton events with a fake third lepton rather than a fake first or second lepton.

In conclusion, the object reconstruction algorithms for ATLAS should perform well enough for a SUSY trilepton analysis. The high lepton reconstruction efficiencies, in addition to the excellent suppression of fake leptons observed for both SUSY and SM samples, should aid in the development of a solid analysis aimed at selecting high lepton multiplicities in the final state. In the following chapters, the strategy and results for an inclusive and an exclusive trilepton analysis will be presented.

Chapter 5

Trileptons at ATLAS and Analysis Strategy

5.1 General Strategy for a Trilepton Analysis

To develop a good working strategy for a trilepton analysis, it is necessary to consider some important kinematic variables of SUSY events for comparison to the SM backgrounds. All the distributions shown in this chapter are after the object preselection described in Section 4.1 has been applied and also after at least three leptons have been requested to be present in the event.

In many new physics searches with leptonic final states, the common practice is to require high-p_T leptons [31]. However, due to small differences in the SUSY particle masses, the leptons in trilepton events have a tendency to be “softer” (have lower p_T) in comparison to those from lower lepton multiplicity events. This is confirmed in the p_T distributions of the leading three leptons in trilepton events, seen in Figure 5.1$(a)-(c)$, where both the SUSY and SM distributions display very similar shapes. The p_T spectra of the third lepton is observed to be particularly soft for all the SUSY benchmark points considered here and is the driving need behind the low-p_T threshold of 10 GeV used for leptons in these analyses. A more detailed study of the lepton p_T threshold can be found in Section 7.3.

The requirement of large hadronic activity in an event is a common discriminatory tool in the search for SUSY. The jet multiplicity is plotted in Figure 5.1(d) for both SUSY and SM trilepton events, where it can be seen the distributions for SU2, SU3 and SU4 are shifted towards higher values than the SM backgrounds. In addition to high jet multiplicity, SUSY events also display high-p_T jets, as seen in Figure 5.1(e), where the leading jet p_T is plotted for SUSY and SM trilepton events. The p_T distributions of the hardest jet for SU2, SU3 and SU4 trilepton events all display long tails at high-p_T, whereas the tails for the SM distributions vanish rapidly for p_T^{jet1} larger than $\sim$ 200 GeV. Therefore, taking into account the high jet multiplicity and leading jet p_T in SUSY events, the hadronic activity of the event may be a useful way to control the SM background to SUSY trilepton events that also have final state jets. Therefore, it has been decided to require a high-p_T jet signature as part of the inclusive trilepton selection

The jet multiplicity and leading jet p_T distribution are also plotted for the $\tilde{\chi}\tilde{\chi}$ component of the SU2 signal in Figure 5.1(d) and Figure 5.1(e) respectively. In contrast to what is observed for the inclusive SUSY trileptons signals, the SU2 $\tilde{\chi}\tilde{\chi}$ signal displays a lower jet multiplicity which is comparable to the SM background distributions. The p_T distribution of the leading jet in SU2 $\tilde{\chi}\tilde{\chi}$ trilepton events is also seen to exhibit a rather soft spectrum. The low hadronic activity associated with the SU2 $\tilde{\chi}\tilde{\chi}$ signal could be used for background discrimination by invoking a jet veto as part of the exclusive trilepton selection.

As discussed in Section 3.1, R-Parity conserving SUSY scenarios will always produce two LSPs per event, which will escape detection and be indirectly measured as missing transverse energy. Large $\not{E}_T$ is a characteristic SUSY signature and is seen in Figure 5.1(f), where the $\not{E}_T$ of the SUSY and SM background events is plotted. Both the SU3 and SU4 SUSY samples display a significant excess of events at large $\not{E}_T$ in comparison to the SM backgrounds, whereas this excess is less prominent for the SU2 SUSY sample, due to the lower cross-section for SUSY production in the focus point region. The $\not{E}_T$ distribution for SU2 $\tilde{\chi}\tilde{\chi}$ trilepton events is also shown in Figure 5.1(f), where it can be seen that the $\tilde{\chi}\tilde{\chi}$ component of the SU2 signal has a lower $\not{E}_T$ distribution compared to the full SUSY samples. Nevertheless, this distribution is still peaked at slightly higher values than the SM backgrounds, which could be used to discriminate against SM processes, like ZZ events, that have little or no $\not{E}_T$.

This first overview of the kinematic variables for trilepton events already shows that the inclusive and exclusive trilepton analyses will have to adopt very different strategies, with one associated with large hadronic activity and the other being characterised by a hadronically quiet environment. The full strategy for the inclusive analysis is discussed below in Section 5.2, while the exclusive analysis described in Section 5.3. For the inclusive analyses, the integrated lumi-

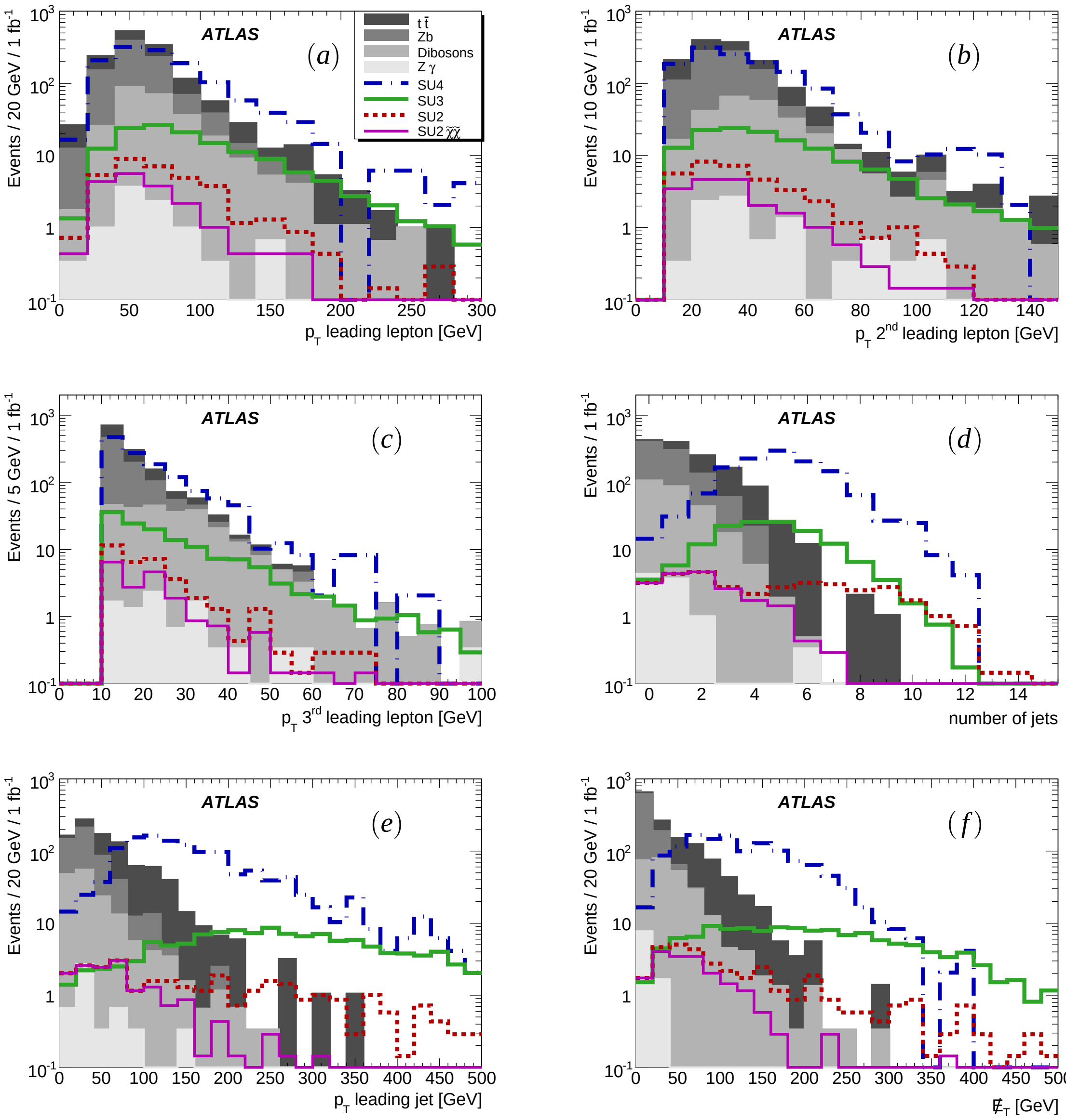

Figure 5.1: Distributions of some interesting kinematic variables for SUSY and SM samples. All distributions are after the three lepton requirement has been made and are normalised to 1 fb^{-1}.

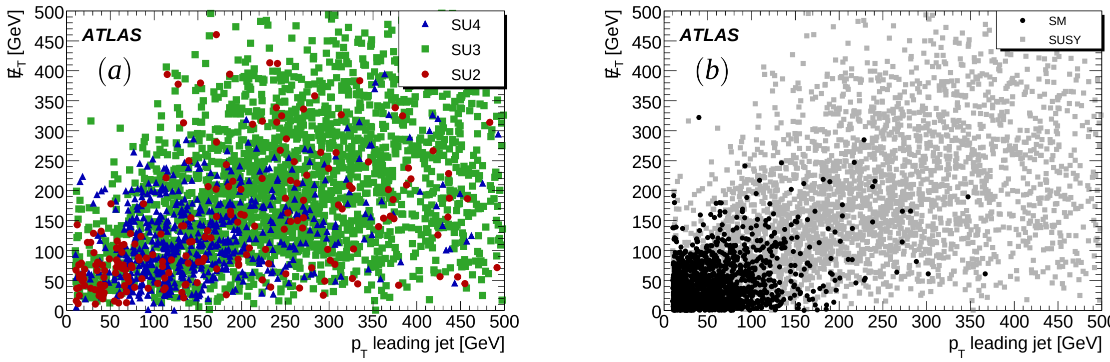

Figure 5.2: The $\not\!\!E_T$ vs p_T^{jet1} for SU2, SU3, SU4 trilepton events, *(a)*, and for both the SUSY events and SM background events, *(b)*.

nosity considered is 1 fb^{-1}, whereas a higher integrated luminosity of 10 fb^{-1} is considered for the exclusive analysis, due to the intrinsically lower statistics associated with that channel. The event selection outlined for the inclusive and exclusive analyses below has been optimised using the signal significance $S/\sqrt{B}$. A further discussion of choice of signal significance is presented in Section 7.2.

5.2 Inclusive Trilepton Analysis

In Section 5.1, it was seen that the presence of significant hadronic activity and/or of large $\not\!\!E_T$ in the event could be used to separate the inclusive trilepton SUSY signal from the SM background. However, events that are characterised by a high-p_T jet are typically associated with large $\not\!\!E_T$, as the rest of the event recoils against the jet. This suggests a correlation between the $\not\!\!E_T$ of an event and the p_T of the leading jet, which is clearly seen in Figure 5.2(a) for the three SUSY samples and Figure 5.2(b) for both the SUSY and SM trilepton events. The presence of such a correlation implies that if a hard cut on the p_T threshold of the leading jet in the event is made then any additional selection using the $\not\!\!E_T$ may be unnecessary (and vice versa).

There is now the possibility of developing an inclusive trilepton analysis that could rely on either the $\not\!\!E_T$ of the event or the p_T of the leading jet. Yet, for an early physics programme when the $\not\!\!E_T$ systematics may not be fully understood, it would be sensible to minimise reliance on the $\not\!\!E_T$ variable and instead rely on the presence of high-p_T jets in the final state. In addition to p_T^{jet1} possibly being a safer variable for use for early data than $\not\!\!E_T$, it is also seen to be more effective

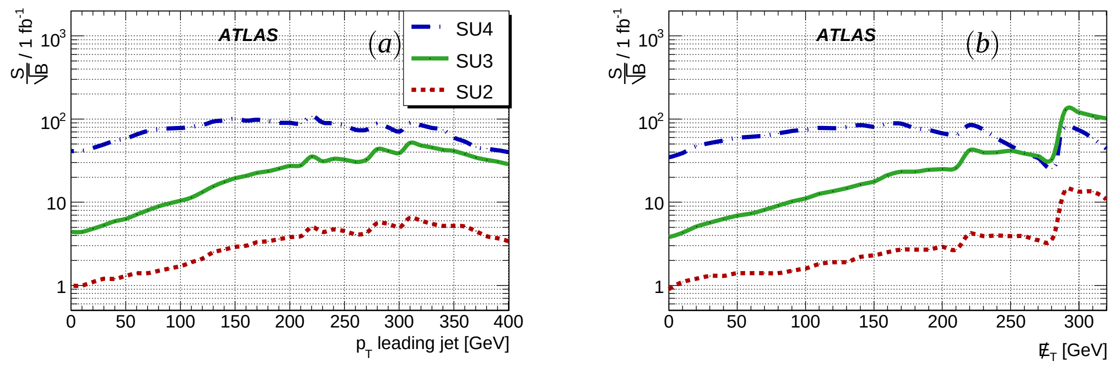

Figure 5.3: Signal Significance $S/\sqrt{B}$ vs the p_T^{jet1} cut on the leading jet transverse momentum, *(a)*, and vs the cut on $\not{E}_T$, *(b)*, for SU2 (*dashed*), SU3 (*solid*) and SU4 (*dash-dotted*), normalised to 1 fb^{-1} of data.

at removing SM backgrounds.

The signal significances $S/\sqrt{B}$ as a function of the cuts on p_T^{jet1} and $\not{E}_T$ for the SUSY samples separately are plotted in Figure 5.3(a) and Figure 5.3(b) respectively. In both plots it is seen that for very hard cuts of $p_T^{jet1} \sim 250$ GeV, or $\not{E}_T \sim 200$ GeV, the statistics for all samples studied becomes rather limited, which causes the fluctuations in the $S/\sqrt{B}$ graphs in all SUSY scenarios. The large fluctuations seen in $S/\sqrt{B}$ at high $\not{E}_T$ in Figure 5.3(b) are due to a very small number of events surviving in the $t\bar{t}$ sample. Although a selection requiring a high $\not{E}_T$ improves the signal significance for all three SUSY scenarios, the maximal $S/\sqrt{B}$ reached are all slightly lower than those for a selection based on a high-p_T jet. As the p_T^{jet1} threshold is raised, $S/\sqrt{B}$ is seen to increase gently for all three SUSY samples in Figure 5.3(a). The $S/\sqrt{B}$ curves for SU2 and SU3 both show slow increases up to around $p_T^{jet1} \sim 300$ GeV, whereas SU4 reaches a plateau by ~ 150 GeV. As a sensible compromise, a common cut at $p_T^{jet1} > 200$ GeV is chosen for all three SUSY points. For completeness a complementary selection has also been investigated, where a $\not{E}_T$ cut is used with the trilepton requirement as the main selection criterion, and the results of this study are presented in Section 7.4.

Despite the observed correlation between p_T^{jet1} and $\not{E}_T$, the possibility of an additional cut on $\not{E}_T$ has also been explored. In Figure 5.4(a) the $\not{E}_T$ distributions are plotted for SUSY and SM backgrounds after the $p_T^{jet1} > 200$ GeV cut has been applied. At this stage of the analysis, there is no obvious $\not{E}_T$ selection that would reduce the remaining background contamination without also reducing the signal statistics significantly. This observation is reinforced by the significance

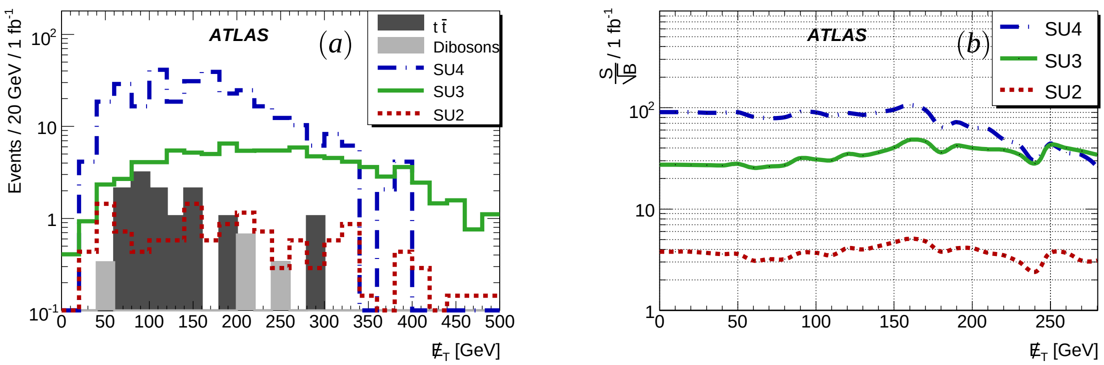

Figure 5.4: The $\not{E}_T$ distribution *(a)*, after the $p_T^{jet1} > 200$ GeV cut is applied to the leading jet p_T in the inclusive trilepton analysis. A possible $\not{E}_T$ requirement is investigated in *(b)* for SU2 (*dashed*), SU3 (*solid*) and SU4 (*dash-dotted*), where the $S/\sqrt{B}$ is shown as the threshold on $\not{E}_T$ is varied. All plots are normalised to 1 fb^{-1}.

graphs in Figure 5.4(b), where the ratio $S/\sqrt{B}$ is shown as a function of the potential $\not{E}_T$ cut, after the cut on p_T^{jet1} has been applied.

In conclusion, a very simple inclusive trilepton selection can be defined here that relies only on the presence of three isolated leptons and a high-p_T jet in the final state. The results from this analysis are presented in Section 6.1, and a discussion of systematics can be found in Chapter 7.

5.3 Exclusive Trilepton Analysis

If nature gives us a SUSY scenario where all coloured sparticles (possibly including the gluino) are beyond the reach of the LHC, leptonic decays of directly produced gauginos could become one of the preferred modes to search for SUSY. The exclusive trilepton SUSY selection presented here is principally aimed at selecting the direct gaugino pair component of the signal in the focus point region of the parameter space, but can be easily generalised to other scenarios where the strongly interacting sparticles are too heavy to be abundantly produced at LHC energies. In this analysis the SUSY component from direct gaugino production (“SU2 $\tilde{\chi}\tilde{\chi}$”) has been separated from the total of the SU2 SUSY events (“SU2 All”) using MC generator level information. In Section 5.1, it was seen that the trilepton SU2 $\tilde{\chi}\tilde{\chi}$ events are associated with low hadronic activity and lower than average $\not{E}_T$, in contrast with the inclusive trilepton analysis presented in Section 5.2. A selection is presented here for the exclusive trilepton channel that exploits the isolation of the leptons and invokes a jet veto to suppress SM backgrounds.

After the requirement of at least three leptons in the event, $t\bar{t}$ and Zb are the dominating SM backgrounds to the SU2 $\tilde{\chi}\tilde{\chi}$ trilepton signal. Direct gaugino production and decay to three leptons involves a neutralino decaying via a virtual Z boson to a "Same Flavour Opposite Sign" (SFOS) lepton pair, as seen in Figure 3.2. SM backgrounds involving leptonic Z boson decays will also result in SFOS lepton pairs, however, backgrounds such as $t\bar{t}$ will produce leptons from independent decays and have no preference towards lepton flavour-sign. To remove backgrounds that produce opposite sign lepton pairs of any flavour, a SFOS lepton pair is required to be present amongst the three leptons. This selection only has an effect on the $t\bar{t}$ background, which is reduced by a third.

All three leptons from direct gaugino production are expected to be very clean and isolated due to the lack of hadronic activity in the event. In contrast, at least one lepton from the $t\bar{t}$ or Zb SM backgrounds will be from a b-quark decay, which will be less isolated due to the proximity to a jet, or from a misidentified jet, which should also display worse isolation. Lepton isolation in the calorimeter has already been demanded in the reconstruction of electrons and muons, as discussed in Section 4.1. In addition to the calorimeter isolation for leptons, track isolation is investigated here as a powerful way to discriminate against leptons originating from b-quark decay. The method implemented here was originally developed for the ATLAS $H \rightarrow 4\ell$ analysis [49].

For each of the three leptons, the highest p_T track p_T^{track} is found in a $\Delta R = 0.2$ cone around the lepton track. The highest p_T^{track} amongst the three leptons is defined as p_T^{max} and can be seen in Figure 5.5(a)-(b) for electrons and muons separately. Effects such as bremsstrahlung that induce isolation differences between the lepton flavours can clearly be seen when comparing the p_T^{max} distributions for electrons and muons. Any event with at least one lepton from b-quark decay (or even a misidentified jet) will result in a large value of the variable p_T^{max}, whether the other leptons are well isolated or not. This is confirmed by the long tails seen in the $t\bar{t}$ and Zb distributions in Figure 5.5(a)-(b). Since the SUSY signal events have three well isolated leptons, the p_T^{max} distribution tends towards low p_T^{max} values. The significance ratio $S/\sqrt{B}$ as a function of the upper limit on p_T^{max} is shown in Figure 5.5(c) for electrons and muons. Excellent background rejection can be achieved by demanding p_T^{max} to be smaller than 1 GeV for muons and 2 GeV for electrons. This stringent lepton track isolation reduces the $t\bar{t}$ background by a factor of four and Zb by a factor of three, while retaining almost 90% of the SUSY signal.

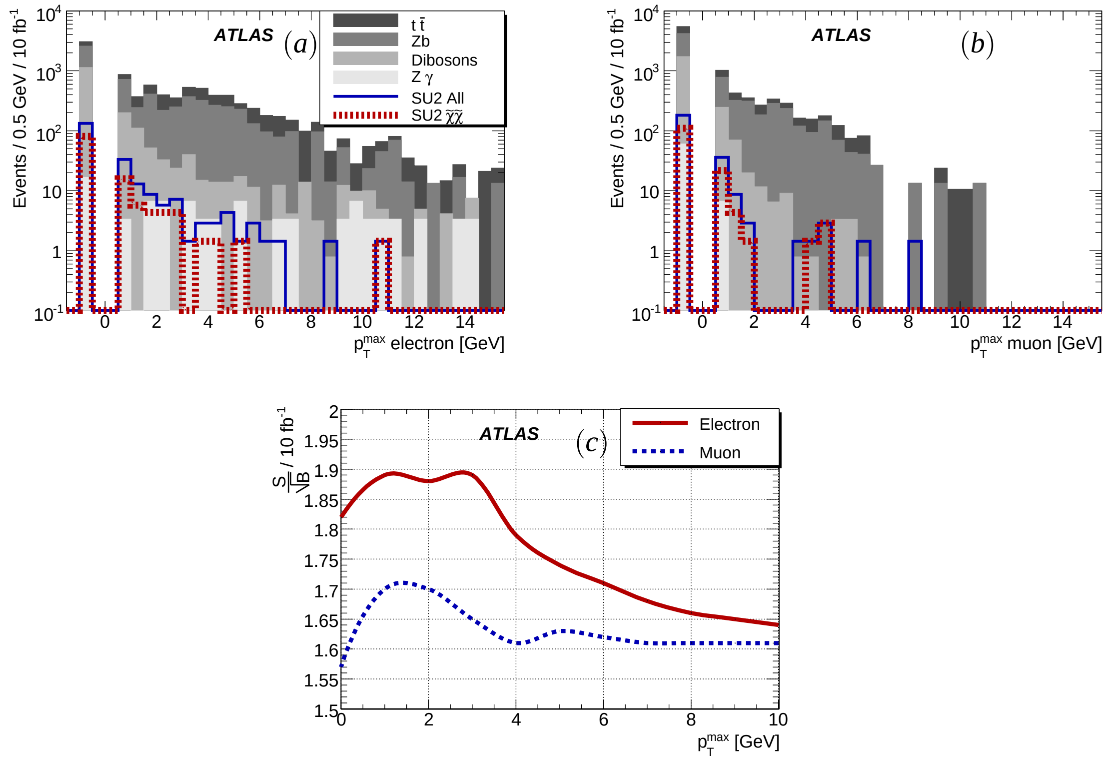

Figure 5.5: Lepton track isolation, p_T^{max}, for electrons *(a)* and muons *(b)*. Entries in the $p_T^{max} = -1$ GeV bin correspond to cases where no other track was found around the lepton tracks in the event. The $S/\sqrt{B}$ as a function of the p_T^{max} threshold is shown in *(c)*. All distributions are normalised to 10 fb^{-1}.

At this stage of the analysis, it is the diboson processes that dominate the SM background. The leptons from diboson processes are all well isolated and so the level of these backgrounds remains high, even after stringent lepton track isolation is required. One approach to discriminate against SM backgrounds is to consider the source of the SFOS lepton pair in the trilepton events. In SU2 $\tilde{\chi}\tilde{\chi}$ events, the SFOS pair originates from a neutralino decay. Thus, the invariant mass of the SFOS lepton pair (M_{SFOS}) in signal events will be less than or equal to the mass difference of the lightest two neutralinos (for SU2, see Table 3.2). However, in Z boson SM background events, the SFOS pair originates directly from the Z boson. The invariant mass of SFOS lepton pairs from a Z boson should cluster around the Z boson mass of 91.2 GeV.

The invariant mass of all the SFOS lepton pair combinations in each event is plotted in Figure 5.6 where a distinct peak is observed around the Z boson mass. The peak is principally the Zb and diboson SM backgrounds, whereas the M_{SFOS} distribution for SUSY signal events is seen

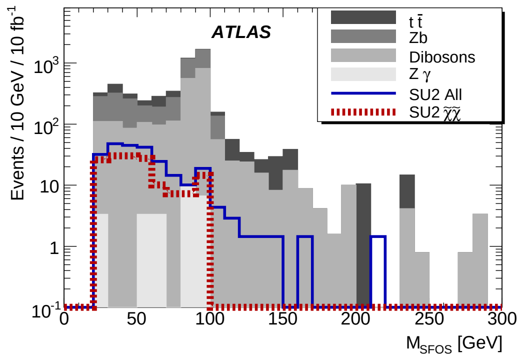

Figure 5.6: The invariant mass M_{SFOS} of SFOS lepton pairs in trilepton events, after the lepton track isolation cut has been applied. All distributions are normalised to 10 fb^{-1}.

to be bounded at $\sim$ 100 GeV. Clearly, Z boson SM background events can be flagged as events that have a SFOS lepton pair with invariant mass around the Z boson mass. Therefore, events are rejected that have a SFOS lepton pair with invariant mass that falls within a 10 GeV window of the Z boson mass ($|M_{SFOS} - M_Z| > 10$ GeV). This stage of the selection dramatically decreases the SM backgrounds, with the diboson and Zb backgrounds reduced by a factor of six, $Z\gamma$ by a factor of four, while about 80% of the SUSY signal is retained.

By applying stringent track isolation and restricting the invariant mass of the SFOS lepton pair to outside a 10 GeV window of the Z boson mass, good SM background event rejection has been achieved, yet significant amounts still remain. Typically, a SUSY selection will require large $\not{E}_T$ in the event in order to select SUSY events with very massive escaping LSPs from SM events that will (at most) have escaping neutrinos (in the absence of detector effects). However, in the case of direct gaugino production, the final state LSPs tend to be produced almost back-to-back in the transverse plane, as seen at generator level in Figure 5.7(b). When the two LSPs are roughly back-to-back in the transverse plane, they balance out one another, resulting in a lower than average $\not{E}_T$ distribution.

The $\not{E}_T$ distribution is seen in Figure 5.7(a) after lepton track isolation and the Z boson mass window removal have been applied. The SUSY signal and $t\bar{t}$ $\not{E}_T$ distributions are seen to be rather similar and so a selection requiring large $\not{E}_T$ is not so useful in this analysis. Nevertheless, it is also noted that backgrounds such as ZZ and $Z\gamma$ tend towards even lower $\not{E}_T$ values than the SUSY signal, since these processes cannot simultaneously decay to three leptons and produce $\not{E}_T$ in the form of neutrinos. The significance ratio $S/\sqrt{B}$ is shown in Figure 5.7(c) as a function of the cut on $\not{E}_T$, where it is seen that demanding just a small amount of $\not{E}_T$ in the event will improve

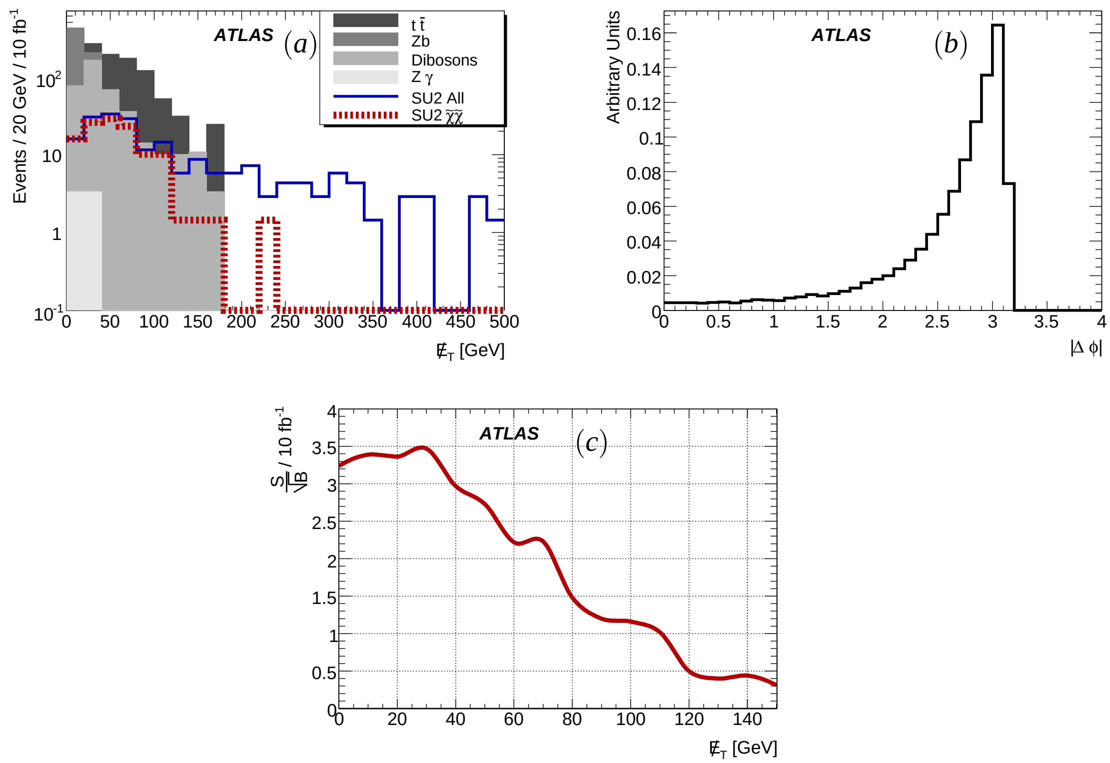

Figure 5.7: The distribution of the total missing transverse energy $\not{E}_T$,*(a)*, after the Z mass window requirement has been applied and the $|\Delta\phi|$ distribution between the two generator level LSPs in direct gaugino production events, *(b)*. The significance ratio $S/\sqrt{B}$ for SU2 direct gaugino production is shown in *(c)* as a function of the $\not{E}_T$ cut. All distributions are normalised to 10 fb^{-1}.

the signal significance. A selection is made requiring $\not{E}_T$>30 GeV in the event which reduces the SM backgrounds by a factor of two and retains 80% of the direct gaugino SUSY signal.

Only the SFOS lepton pair and lepton track isolation requirements have thus far had any real success in reducing the $t\bar{t}$ and SUSY background (non-gaugino production) events, with the M_{SFOS} and $\not{E}_T$ requirements making very little further impact. In order to further suppress the remaining $t\bar{t}$ and SUSY backgrounds, a veto on the hadronic activity in the event has been implemented. Top pair production is associated with at least two high-p_T jets in the final state from the b-quarks and SUSY background events will usually produce a high-p_T jet from a squark/gluino decay into a neutralino (which then decays leptonically). Direct gaugino production and decay to three leptons is characterised by a lack of hadronic activity in the event, where the only final state jets should be soft as they will come from the underlying event. This is very different to many SUSY signatures, which usually require high-p_T jets in the final state, but the quiet hadronic

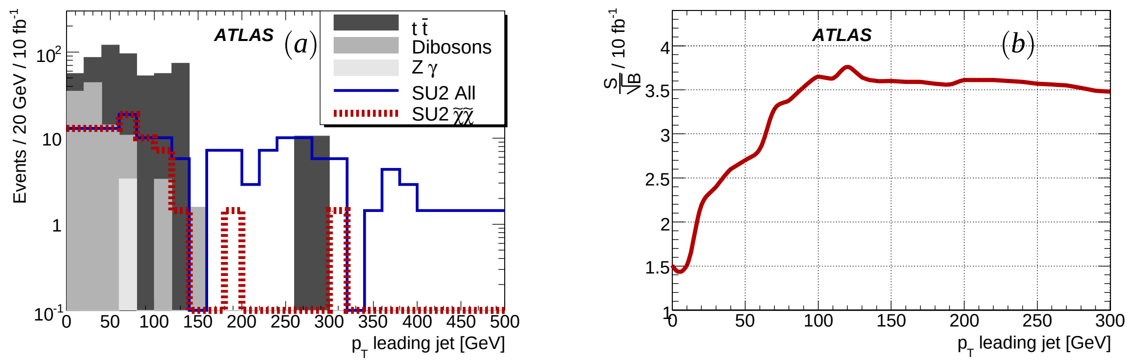

Figure 5.8: The p_T distribution of the leading jet in trilepton events *(a)*, after the $\not{E}_T$ requirement has been applied. The $S/\sqrt{B}$ is also shown as the cut on the jet p_T is varied *(b)*. All distributions are normalised to 10 fb^{-1}.

environment associated with trilepton events from direct gaugino production in the focus point is still useful for SM background discrimination.

The transverse momentum of the leading jet in the event, p_T^{jet1}, is shown in Figure 5.8(a) where it is seen that direct gaugino SUSY events have softer leading jets than other SUSY events and $t\bar{t}$. The signal significance ratio $S/\sqrt{B}$ as a function of the jet veto as shown in Figure 5.8(b), where it is seen that requiring no jet to have a p_T above 100 GeV is optimal for this analysis. Requiring the event to have a leading jet p_T <100 GeV reduces the $t\bar{t}$ background to approximately 70% of previous levels, retains approximately 90% of the signal from directly produced gaugino pairs and suppresses the non-gaugino SUSY component to a negligible level.

It should be noted here that a very harsh jet veto could be implemented here ($\sim$ 20 GeV) to reduce the $t\bar{t}$ background to the lowest possible level. This was done in [31] and successfully reduced the $t\bar{t}$ to 10% of previous levels. However, much of the signal is also lost in such an approach and, as seen in Figure 5.8(b), a harsh jet veto results in a low, non-optimal signal significance for the SU2 $\tilde{\chi}\tilde{\chi}$ trilepton channel. The method detailed below, which utilises the lepton impact parameter to reduce $t\bar{t}$ to minimal levels while retaining the bulk of the direct gaugino trilepton signal, is seen to be a preferable alternative to a hard jet veto.

The stringent lepton track isolation requirement suppresses trilepton events where leptons are in close proximity to a jet or are misidentified jets. The impact parameter d_0 of the lepton tracks with respect to the interaction point is also investigated here, to provide an additional method to identify leptons from b-quark decays. A lepton originating from the decay of a b-quark will have,

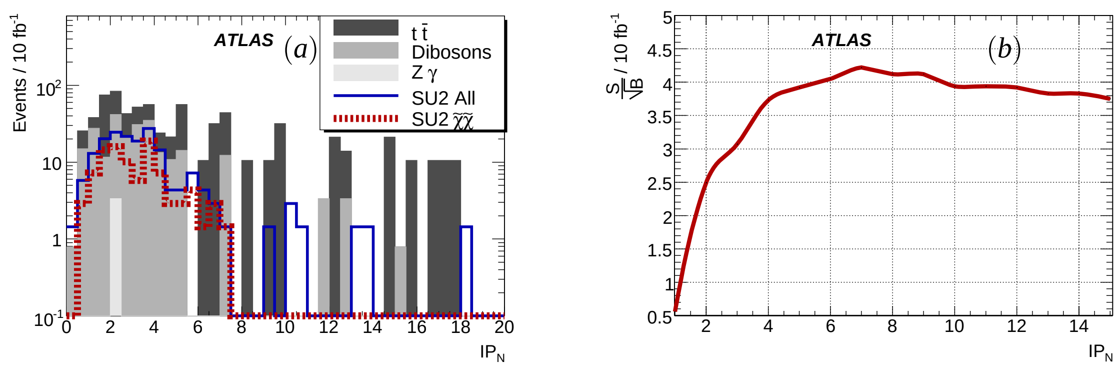

Figure 5.9: The distribution of the highest IP_N value for the three leptons in the event *(a)*, for events that pass the $\not{E}_T$ selection but before any jet veto cut is applied. The signal significance $S/\sqrt{B}$ as a function of the cut on IP_N is also shown *(b)*. All distributions are normalised to 10 fb^{-1}.

on average, a larger displacement d_0 from the interaction point than the prompt leptons in signal events. At least one of the leptons in $t\bar{t}$ trilepton events will be from a b-quark decay, whereas all three leptons from direct gaugino production will be prompt leptons. Thus, d_0 could be used in further background discrimination. For early data taking, the systematics for d_0 reconstruction may not be fully understood. However, the low statistics associated with the exclusive trilepton channel imply that the the d_0 variable should be fully understood by the time hadronically quiet channels become accessible.

Another option is to consider the lepton impact parameter normalised to its error, defined as $IP_N = d_0/\sigma_{d_0}$ [49]. The IP_N value is calculated for all three leptons and the largest value amongst the three is plotted in Figure 5.9(a) for events that pass the $\not{E}_T > 30$ GeV selection, but before the jet veto is applied. It is seen that the IP_N distribution for $t\bar{t}$ has longer tails than the SU2 $\tilde{\chi}\tilde{\chi}$ events. It should be noted here that the IP_N $t\bar{t}$ distribution in Figure 5.9(a) is affected by limited statistics and is scaled up by an order of magnitude for the normalisation to 10 fb^{-1}. In Figure 5.9(b), the signal significance as a function of the IP_N threshold is plotted after the $\not{E}_T$ requirement, but before any jet veto cut. The curve for $S/\sqrt{B}$ is seen to rise and reach a rough plateau around $IP_N < 6$. A selection requiring $IP_N < 6$ at this stage reduces the $t\bar{t}$ background to approximately 50% of previous levels, the SUSY background to approximately 85% of previous levels and retains approximately 94% of the signal from directly produced gaugino pairs.

The jet veto and impact parameter requirements serve to reduce the SUSY and $t\bar{t}$ backgrounds respectively, while both successfully retain the SUSY signal. If both cuts are to be included in the

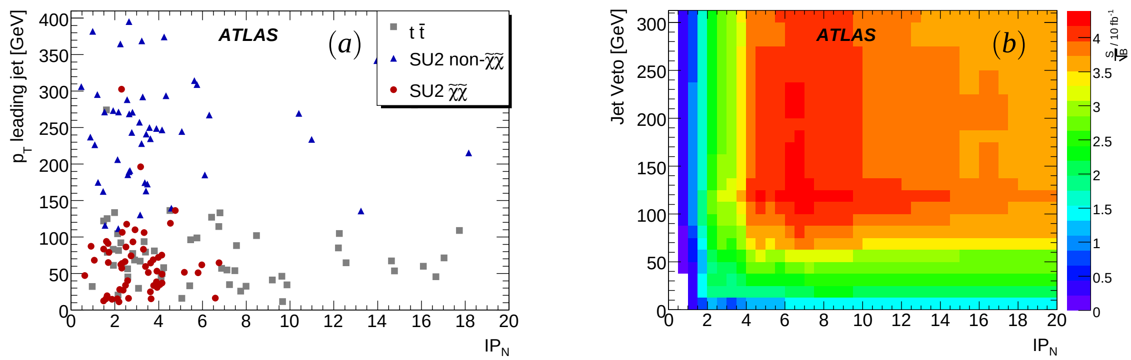

Figure 5.10: Scatter plot of the leading jet p_T vs the highest IP_N value among the three leptons, *(a)*, after the $\not{E}_T$ selection is applied. A 2-D contour of the signal significance $S/\sqrt{B}$ is also shown *(b)* as both the jet veto and the IP_N requirements are varied at the same time. All distributions are normalised to 10 fb^{-1}.

exclusive trilepton selection, it is important to investigate any correlation between the two that may exist. In Figure 5.10(a) the lepton IP_N is plotted against the leading jet p_T, after the $\not{E}_T$ cut has been applied. A combination of both a loose jet veto and a IP_N requirement is seen to remove almost all the SUSY background events, as well as suppressing much of the $t\bar{t}$ background. Most importantly, most of the SU2 $\tilde{\chi}\tilde{\chi}$ events would be retained by such a selection. This is confirmed in Figure 5.10(b), where the signal significance as a function of the IP_N and jet veto cut is plotted. A selection requiring a jet veto at 100 GeV and an impact parameter of $IP_N < 6$ give near-optimal results, in absence of other systematic effects not considered here.

The exclusive trilepton analysis has proved to be more complex than the simple inclusive trilepton analysis. Good background suppression is achieved through the application of stringent lepton track isolation, a jet veto and the removal of events with a Z compatible SFOS lepton pair. The final event selection and results for this analysis are presented in Section 6.2, and a discussion of systematics can be found in Chapter 7.

Chapter 6

Results from the Inclusive and Exclusive Trilepton Analyses

The results of the trilepton analyses presented in Chapter 5 are summarised and discussed in this chapter. In Section 6.1, the results of the inclusive trilepton analysis for a range of mSUGRA benchmark scenarios are presented, followed by the results of the exclusive trilepton analysis for the focus point region in Section 6.2. Object reconstruction and event variable definitions follow those outlined in Section 4.1 and the preselection described is applied before any event selection reported below is imposed. Results are presented in terms of the signal significance ratio $S/\sqrt{B}$ and of the signal-to-background ratio S/B. The results of a number of possible sparticle mass measurements that may be made using the kinematic endpoints of lepton-jet invariant mass distributions, are presented in Section 6.3. Finally, preliminary results of the inclusive trilepton analysis at a lower centre of mass energy of 10 TeV are shown in Section 6.4. Results from systematic studies that have been performed will be presented in Chapter 7.

6.1 The Inclusive Trilepton Analysis

The strategy for the inclusive trilepton analysis was discussed in Section 5.2 and aimed to maximise the discovery potential of SUSY across mSUGRA parameter space. In summary, the event selection for a SUSY inclusive trilepton signal is given by:

1. $N_\ell \geq 3$ with $p_T^{lep} > 10$ GeV;

	No Cut	N_ℓ	p_T^{jet1}
SU2	7111.7	35.0	13.0
SU3	27304.3	139.3	94.3
SU4	396445.5	1283.9	311.7
$t\bar{t}$	440657.9	444.0	10.6
Zb	159115.7	661.6	0.0
ZW	15672.0	192.7	1.3
ZZ	3820.2	58.9	0.0
WW	40051.7	3.3	0.0
$Z\gamma$	3283.2	9.4	0.0
$\frac{S}{\sqrt{B}}$	SU2	0.9	3.8
	SU3	3.8	27.3
	SU4	34.7	90.3
$\frac{S}{B}$	SU2	0.0	1.1
	SU3	0.1	7.9
	SU4	0.9	26.2

Table 6.1: Number of surviving events for all considered SUSY and SM samples as the inclusive trilepton selection cuts are applied. The ratios $S/\sqrt{B}$ and S/B are also given for the three benchmark SUSY scenarios. All values are normalised to 1 fb^{-1} of data.

2. $N_{jet} \geq 1$ and $p_T^{jet1} > 200$ GeV.

where N_ℓ is the number of leptons (electrons or muons), N_{jet} is the number of jets and p_T^{jet1} is the transverse momentum of the leading jet in the event. In Table 6.1, the number of SUSY and SM background events, as well as the $S/\sqrt{B}$ and S/B ratios as the event selection progresses is shown. It is immediately evident that the requirement of at least three leptons in the event heavily suppresses all the SM backgrounds considered for this analysis, while the high-p_T jet requirement serves to eliminate virtually all of the remaining Zb and diboson SM backgrounds. In fact, only a small number of $t\bar{t}$ events actually survive the inclusive trilepton selection and these are considered so few as to not require any further background discrimination.

The signal significance ratio $S/\sqrt{B}$ is shown in Figure 6.1 as a function of the integrated luminosity $\int \mathcal{L}dt$ for the three considered SUSY scenarios in the absence of any systematics not considered here. The inclusive trilepton signature is seen to be an excellent candidate for early discovery of new physics at ATLAS, particularly for the low mass scenario. Realistically, the quoted discovery potentials for the SUSY scenarios considered here will be worsened once the systematics, detector, trigger and reconstruction performance have been understood and taken into account.

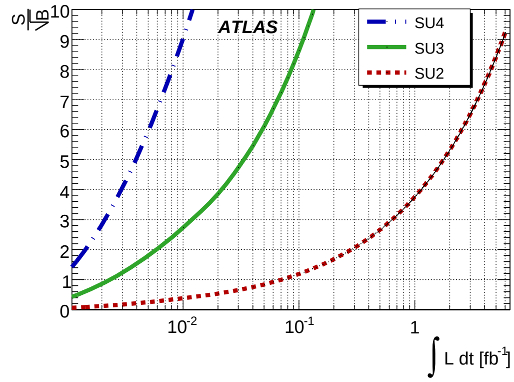

Figure 6.1: The final signal significances $S/\sqrt{B}$ of the inclusive trilepton analysis as a function of the integrated luminosity $\int \mathcal{L}dt$, for SU2 *(dashed)*, SU3 *(solid)* and SU4 *(dash-dotted)*.

6.2 The Exclusive Trilepton Analysis

The strategy for the exclusive trilepton analysis was discussed in Section 5.3 and aimed to maximise the discovery potential of direct gaugino production and decay to three leptons at the focus point. The event selection for the exclusive trilepton SUSY signal is given by:

1. $N_\ell \geq 3$ with $p_T^{lep} >$10 GeV;
2. ≥ 1 SFOS lepton pair;
3. Lepton track isolation (within $\Delta R = 0.2$): $p_T^{max} < 1,\ 2$ GeV (for $\mu,\ e$ respectively);
4. Veto on Z mass window: $|M_{SFOS} - M_Z| > 10$ GeV;
5. $\not{E}_T > 30$ GeV;
6. Jet veto: leading jet $p_T^{jet1} < 100$ GeV;
7. Lepton normalised impact parameter: maximum $IP_N < 6$.

In Table 6.2, the number of SUSY and SM background events, as well as the $S/\sqrt{B}$ and S/B ratios as the exclusive event selection progresses is shown. The results for the SUSY SU2 sample are separated into events from directly produced gaugino pairs ("SU2 $\tilde{\chi}\tilde{\chi}$") and all the other SU2 events ("SU2 non-$\tilde{\chi}\tilde{\chi}$") using MC information. With this in mind, the signal significance $S/\sqrt{B}$ and signal-to-noise ratio S/B are calculated for two assumptions. Firstly, that only SU2 $\tilde{\chi}\tilde{\chi}$ events are considered as signal and the SU2 non-$\tilde{\chi}\tilde{\chi}$ events are considered as background. And secondly, that all SU2 events, $\tilde{\chi}\tilde{\chi}$ and non-$\tilde{\chi}\tilde{\chi}$, are considered as signal and only the SM events as background. The results for both assumptions are presented in the last four rows of Table 6.2 and it is observed that once the jet veto is imposed, the SU2 non-$\tilde{\chi}\tilde{\chi}$ component vanishes and the two results converge.

As was seen for the inclusive trilepton analysis in Section 6.1, the trilepton requirement provides excellent suppression of the SM backgrounds. The random flavour-sign lepton combinations produced by $t\bar{t}$ events is exploited in the SFOS lepton pair requirement and reduces the $t\bar{t}$ trilepton contribution by a third. Non-prompt leptons or misidentified jets are rejected using a powerful tight lepton track isolation, which greatly diminishes both the $t\bar{t}$ and Zb backgrounds. Removing events with SFOS lepton pairs in the Z boson mass window results in a large reduction of all the SM backgrounds that contain a Z boson, and a small $\not{E}_T$ requirement removes the surviving Zb contribution. Finally, the jet veto and the lepton impact parameter constraint work together to not only significantly reduce the remainder of the $t\bar{t}$ background, but also completely separate the gaugino pair component of the signal from the rest of the SUSY events. After all event selection has been applied, ZW production remains as the irreducible SM background in the exclusive trilepton analysis. Of the ZW events that remain, the Z boson must be an off-mass-shell Z boson (due to the Z mass window constraint) and thus bears a genuine similarity to the signal process.

The second case, (ii), presented in Table 6.2, where both $\tilde{\chi}\tilde{\chi}$ and non-$\tilde{\chi}\tilde{\chi}$ SU2 events are considered as signal, could be regarded as another inclusive trilepton analysis. Looking at the signal significance for case (ii), it appears that such an inclusive analysis would benefit from the event selection stopping after the $\not{E}_T$ stage, with a final $S/\sqrt{B}$ of 6.8 for 10 fb^{-1} of data. Even so, this "3-lepton+$\not{E}_T$" inclusive analysis does not surpass the far simpler "3-lepton+jet" inclusive analysis at the focus point, discussed in Section 5.2, which would yield a much larger signal significance of 11.9 for 10 fb^{-1} of data.

The signal significance ratio $S/\sqrt{B}$ is shown in Figure 6.2 as a function of the integrated luminosity $\int \mathcal{L}dt$ for the exclusive trilepton analysis at the focus point. As a comparison, the signal significance for the inclusive trilepton analysis at the focus point is also plotted on the same graph. Despite not being an early physics channel, a 5σ discovery can be achieved for the exclusive trilepton channel with an integrated luminosity of few tens of fb^{-1}, in the absence of any systematics not considered here. As noted for the inclusive analysis, the quoted discovery potential will be worsened once the systematics, detector, trigger and reconstruction performance

		No cut	N_ℓ	SFOS	Track Isol.	Z-window	$\not{E}_T$	Jet Veto	IP_N
	SU2 $\tilde{\chi}\tilde{\chi}$	64036.6	186.4	177.7	153.2	119.9	98.3	86.7	80.9
	SU2 non-$\tilde{\chi}\tilde{\chi}$	7080.5	163.3	127.2	95.4	85.3	83.8	0.0	0.0
	$t\bar{t}$	4406578.8	4440.2	2812.2	634.3	507.5	475.7	327.7	179.7
	Zb	1591156.7	6616.1	6562.8	2422.8	386.0	0.0	0.0	0.0
	ZW	156719.6	1926.8	1910.1	1682.2	321.7	217.8	214.5	204.4
	ZZ	38201.8	589.4	579.9	475.8	56.8	13.4	11.8	11.0
	WW	400516.9	32.7	24.5	8.2	8.2	8.2	8.2	0.0
	$Z\gamma$	32832.3	93.9	90.6	26.8	6.7	3.4	3.4	3.4
(i)	$\tilde{\chi}\tilde{\chi} = S$	$S/\sqrt{B}$	1.6	1.6	2.1	3.2	3.5	3.6	4.1
	SM+non-$\tilde{\chi}\tilde{\chi} = B$	S/B	0.0	0.0	0.0	0.1	0.1	0.2	0.2
(ii)	All SU2$= S$	$S/\sqrt{B}$	3.0	2.8	3.4	5.7	6.8	3.6	4.1
	SM$= B$	S/B	0.0	0.0	0.0	0.2	0.3	0.2	0.2

Table 6.2: Number of surviving events for SU2 and considered SM backgrounds as the exclusive trilepton selection cuts are applied. Numbers for the SU2 sample have been separated into two components: events from directly produced gaugino pairs ("$\tilde{\chi}\tilde{\chi}$") and all the other SU2 events ("non-$\tilde{\chi}\tilde{\chi}$"). The ratios $S/\sqrt{B}$ and S/B are shown for (i) - where SU2 $\tilde{\chi}\tilde{\chi}$ events only are considered as the signal - and (ii) - where all SU2 events are considered as the signal. All values are normalised to 10 fb^{-1} of data.

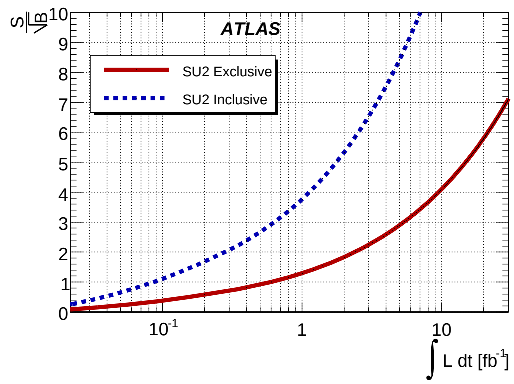

Figure 6.2: Signal significance $S/\sqrt{B}$ as a function of the integrated luminosity $\int \mathcal{L}dt$, for the exclusive SU2 analysis and, for comparison, for the SU2 inclusive analysis.

have been understood and taken into account.

6.3 Kinematic Endpoints

If SUSY, or any new physics, is discovered at the LHC, it will be vitally important to make many measurements in order to constrain the theory. Leptonic channels offer an opportunity to do this by measuring the kinematic endpoints/thresholds of certain invariant mass distributions. As seen in the dilepton SUSY searches [31], the invariant mass of the SFOS lepton pair in the event can be used to constrain the mass differences of the sparticles involved in the decay. These methods can also be implemented for the trilepton analyses, the results of which are presented below.

In the case of SU2 and SU4, the $\tilde{\chi}_2^0$ (and $\tilde{\chi}_3^0$ in SU2) undergoes a branched three-body decay to $\tilde{\chi}_1^0\ \ell^+\ell^-$ as seen in Figure 6.3(a), and so the invariant mass distribution of the SFOS leptons should display a kinematic endpoint at the value of the mass difference between the neutralinos. In SU3 the $\tilde{\chi}_2^0$ undergoes a sequential decay via a $\tilde{\ell}_R$ as seen in Figure 6.3(b), which has a direct effect on the position of the kinematic endpoint of the SFOS lepton invariant mass distribution. The expressions describing the kinematic endpoints and thresholds discussed here can be found in Appendix B. Expected values for this endpoint, known as m_{ll}^{edge}, can be found in Table 6.3, together with values for other thresholds and endpoints explained below.

Both $t\bar{t}$ and other (non-neutralino) SUSY decays, can also produce opposite sign lepton pairs in the final state. In such background processes, there is no preference towards particular flavour combinations, resulting in equal numbers of SFOS and OFOS ("Opposite Flavour Opposite Sign") lepton pairs. Therefore, this combinatorial background can be suppressed by

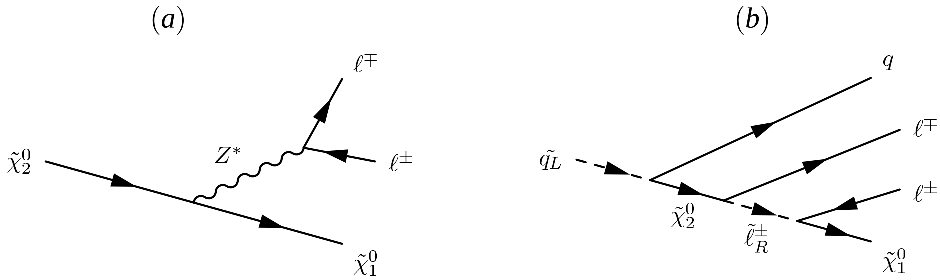

Figure 6.3: Branched three-body $\tilde{\chi}_2^0$ decay to charged leptons and $\tilde{\chi}_1^0$ *(a)*, typical of the SU2 and SU4 points, and the sequential decay chain of a squark to quark plus charged leptons and $\tilde{\chi}_1^0$, *(b)*, seen in the SU3 SUSY scenario (where $\tilde{q}_L$ denotes $\tilde{u}_L$, $\tilde{d}_L$, $\tilde{c}_L$, or $\tilde{s}_L$).

SUSY model	Kinematic Endpoint [GeV]				
	m_{ll}^{edge}	m_{llq}^{edge}	m_{llq}^{thr}	m_{lq}^{high}	m_{lq}^{low}
SU2	57, 77	–	–	–	–
SU3	100	500	249	420	324
SU4	53	–	–	–	–

Table 6.3: Theoretical values for the kinematic endpoints that could be obtained from the trilepton SUSY analyses. The two values for the SU2 m_{ll}^{edge} endpoint refer to the $\tilde{\chi}_2^0/\tilde{\chi}_3^0$ contributions to trilepton final states. Where $m_{\tilde{q}_L}$ is required in the calculation of an endpoint, the average of $m_{\tilde{u}_L}$, $m_{\tilde{d}_L}$, $m_{\tilde{c}_L}$, and $m_{\tilde{s}_L}$ is used.

considering flavour subtracted distributions of the dilepton invariant mass, where m_{ll} is plotted for the combination $(e^+e^- + \mu^+\mu^-) - (e^\pm\mu^\mp)$. In trilepton events that have an ambiguity in how the opposite sign lepton pair could be selected, all combinations are considered. For example, in $e^+e^-e^+$ events, the invariant mass of both the SFOS e^+e^- combinations would be included and in $e^+e^-\mu^+$ events, the invariant mass of the SFOS combination e^+e^- and the OFOS combination $e^-\mu^+$ would be included. In order to observe any excess in SFOS lepton pairs over OFOS lepton pairs in the m_{ll} distribution for the exclusive trilepton analysis, the SFOS requirement has not been included in the event selection.

The m_{ll} distributions for the inclusive and exclusive analyses can be seen in Figure 6.4. A kinematic edge at ~ 60 GeV can be seen in Figure 6.4(a) in the signal distribution of the SU2 exclusive trilepton analysis. Regrettably this is no longer observable when the SM background is included and a similar result can be observed for the inclusive SU2 distributions in Figure 6.4(b). In contrast, an endpoint is observed at ~ 100 GeV in Figure 6.4(c) for the SU3 inclusive trilepton analysis, which continues to be seen even after the SM backgrounds are taken into account. Similarly, in Figure 6.4(d) a relatively clean endpoint can be seen for SU4 at ~ 50 GeV. It should

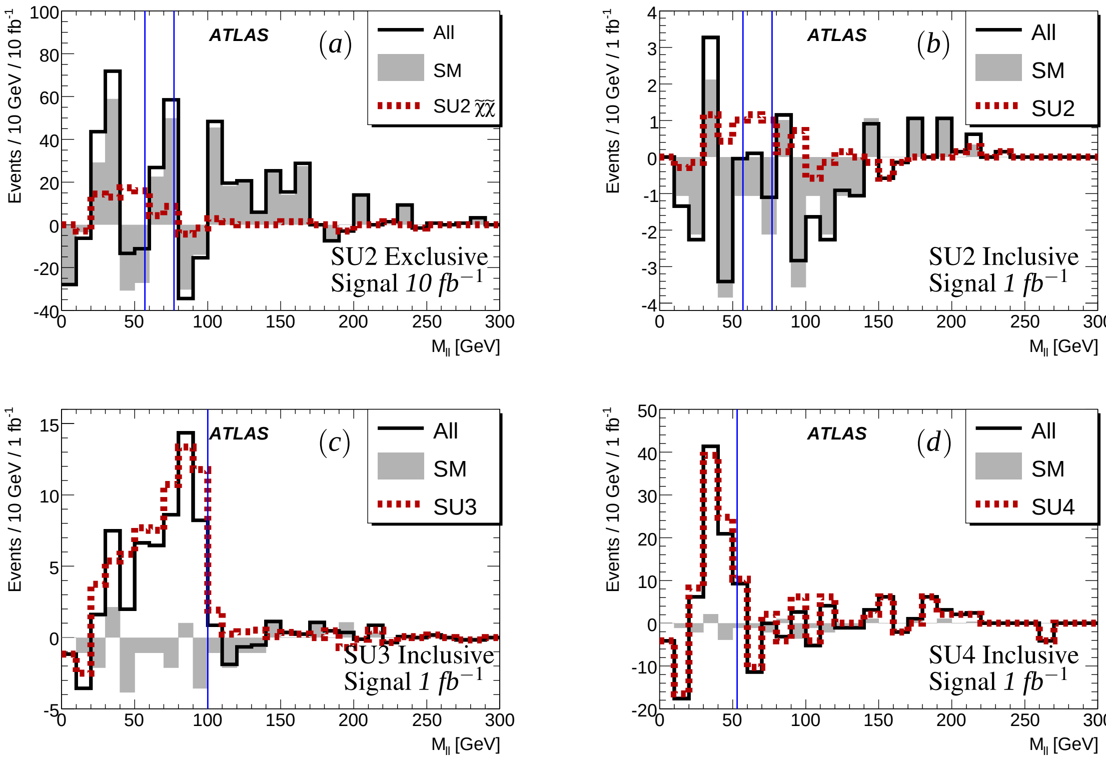

Figure 6.4: Flavour subtracted m_{ll} distributions for *(a)* the exclusive SU2 analysis and the inclusive *(b)* SU2, *(c)* SU3 and *(d)* SU4 analyses. Vertical lines correspond to the expected endpoints (m_{ll}^{edge}) in each distribution. Plots are normalised to 10 fb^{-1} for the exclusive analysis and to 1 fb^{-1} for the inclusive ones.

be noted that, for the inclusive SU2 and SU3 plots (normalised to 1 fb^{-1}), the distributions have been scaled down from the original integrated luminosity of the MC samples, according to the factors given in Table 3.9. The observed statistical fluctuations in the mass edge distributions are therefore less pronounced than those that would be seen in real data for the same normalisation.

When long SUSY decay chains involving squarks or gluinos are present in the event, an opportunity arises to use further invariant mass combinations to extract further constraints on sparticle mass differences. In SU3, long decay chains, such as that seen in Figure 6.3(b), will be relatively common due to the fact that all the sparticles are within easy reach of the LHC. The presence of high-p_T jets in addition to the SFOS lepton pair from these decays gives rise to four additional kinematic edges in the invariant mass distributions m_{llq}^{edge} , m_{llq}^{thr} , m_{lq}^{high} and m_{lq}^{low} , which are plotted from combinations of the leptons and jets.

The m_{llq} distributions are produced using the invariant mass of the SFOS leptons with each of

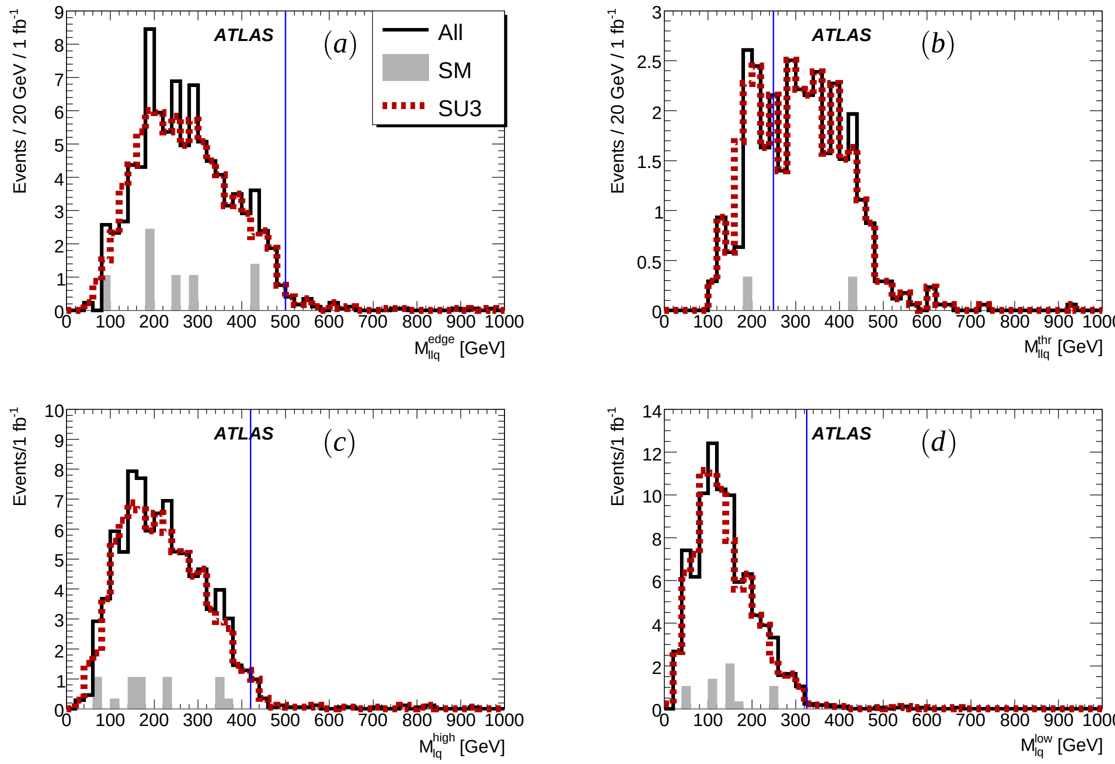

Figure 6.5: Lepton-jet invariant mass distributions for the SU3 inclusive trilepton analysis: m_{llq}^{edge} *(a)*, m_{llq}^{thr} *(b)*, m_{lq}^{high} *(c)* and m_{lq}^{low} *(d)*. All distributions are for 1 fb^{-1} of data.

the two hardest jets in the event. The combination with the smallest invariant mass is plotted for the m_{llq}^{edge} distribution to ensure that the value is below the edge even when the wrong combination has been selected. The theoretical m_{llq}^{edge} value of ~ 500 GeV is quite clearly seen in Figure 6.5(a). The jet-SFOS lepton combination with the higher m_{llq} value is then used to produce the m_{llq}^{thr} distribution. In order to raise the threshold away from zero, an additional requirement is imposed for this distribution, asking that only events satisfying $(m_{ll}^{edge}/\sqrt{2}) < M_{SFOS} < m_{ll}^{edge}$ are selected. It should be noted that the $1/\sqrt{2}$ factor adopted here is an empirical one, which could in principle still be optimised [50], [51]. Theoretically, the m_{llq}^{thr} should be ~ 250 GeV, and it is seen that the distribution in Figure 6.5(b) does in fact display a threshold but at a far lower value than expected. This is attributed to smearing effects such as the presence of squarks of different masses in contributing decay chains, where additional series of thresholds are produced from $\tilde{b}$ and $\tilde{t}$ contributions. For example, a decay as in Figure 6.3(b) involving the relatively lighter $\tilde{t}_1$ would theoretically produce a threshold in the m_{llq}^{thr} distribution at 162 GeV. Furthermore, there is uncertainty in the shape of the threshold and how it may be modified by detector effects.

The final distributions are produced from the invariant mass of each of the two SFOS leptons with each of the two leading jets, choosing the highest and the lowest of the values obtained for m_{lq}^{high} and m_{lq}^{low} respectively. The expected values for these two quantities are ~ 420 GeV and ~ 325 GeV and are roughly seen in Figures 6.5(c) and 6.5(d).

6.4 Preparing for the First ATLAS Data

The very first pp collisions at the LHC are planned for a centre of mass energy of 10 TeV and by the end of the first run around 200 pb^{-1} of data is expected. It was seen in Section 6.2, that the exclusive trilepton channel is not an early data channel, however, in Section 6.1 the inclusive trilepton analysis was seen to be an early data channel, particularly for the SU3 and SU4 benchmark scenarios. In order to be prepared for SUSY searches with the first ATLAS data, it is important to investigate how the results of the inclusive analysis are affected by the initial lower energy collisions. In this section, the trilepton inclusive analysis is repeated for a centre of mass energy of 10 TeV and integrated luminosity of 200 pb^{-1}.

New MC samples have been produced to study LHC physics at the lower centre of mass energy and the cross-sections for the samples used here are listed in Table 6.4. It was seen in Section 6.1 that only a few hundred pb^{-1} of data is required for a 5σ discovery potential for both SU3 and SU4, and so only these two benchmark scenarios are chosen for this lower E_{CM} study. The only SM process to be considered for this study is $t\bar{t}$, since it was the only SM background to survive the inclusive trilepton selection for a E_{CM} of 14 TeV. The MC samples used in this section were generated centrally within the ATLAS Collaboration as part of the the Monte Carlo 2008 (MC08) data challenge. The 14 TeV MC $t\bar{t}$ sample used a top quark mass of 175 GeV, however, an updated value of 172.5 GeV is used for the 10 TeV MC sample. Apart from the lower E_{CM}, the SU3 and SU4 MC samples remain unchanged. Further details concerning data samples and analysis procedure can be found in Appendix A.

The leading jet momentum distribution for SU3, SU4 and $t\bar{t}$ after the three lepton requirement has been made is shown in Figure 6.6(a), where the possibility of including a high-p_T jet requirement is seen again for this lower E_{CM}. The signal significance as a function of the cut on p_T^{jet1} is presented in Figure 6.6(c), where the $S/\sqrt{B}$ curve for SU4 is seen to increase slowly and

Process	σ_{LO} [pb]	$\sigma_{LO} \times \varepsilon_F$	k	$\sigma_{NLO} \times \varepsilon_F$ [pb]	$\int \mathcal{L}dt$ [fb^{-1}]
SU3	6.0	6.0	1.36	8.2	1.2
SU4	122.6	122.6	1.41	172.8	0.3
$t\bar{t}$	401.6	202.9	1.00	202.9	1.8

Table 6.4: The SU3, SU4 and $t\bar{t}$ samples used for the 10 TeV trilepton analyses. The LO total cross-sections, with and without taking into account the generator filter efficiency ε_F as well as the NLO k-factors used to rescale the cross-sections are shown (for the SUSY samples, both LO and NLO numbers are from Prospino 2.0.6). The NLO cross-sections with filter efficiency applied are shown in the $\sigma_{NLO} \times \varepsilon_F$ column. The integrated luminosities corresponding to the total statistics in each sample are given in the last column.

plateau at ∼100 GeV. In contrast, the $S/\sqrt{B}$ curve for SU3 reaches a maximum at a higher value of around 200 GeV. Above p_T^{jet1} ∼200 GeV, fluctuations arise in the $S/\sqrt{B}$ curves, due to limited statistics. A common selection using either p_T^{jet1} >150 GeV or even the original p_T^{jet1} >200 GeV could be used as a compromise for an inclusive trilepton analysis at an E_{CM} of 10 TeV.

The $\not{E}_T$ distribution is presented in Figure 6.6(b) for the SUSY signals and $t\bar{t}$ at the three lepton stage of the selection. An excess of SUSY events with large $\not{E}_T$ is observed, suggesting a $\not{E}_T$ selection could be used to discriminate against $t\bar{t}$ events. In Figure 6.6(d), the signal significance for SU3 and SU4 is plotted as a function of the cut on $\not{E}_T$. Although a $\not{E}_T$ requirement is seen to improve the signal significance for both SU3 and SU4, the maximum values reached before statistical fluctuations are observed are lower than can be achieved with a p_T^{jet1} selection. The additional issue of understanding $\not{E}_T$ systematics with early data make a $\not{E}_T$ requirement less attractive than a selection requiring high-p_T jet.

An inclusive trilepton selection for a E_{CM} of 10 TeV can be defined as at least three leptons and one high-p_T jet in the final state. The p_T^{jet1} requirement may either remain at 200 GeV as was the case for the 14 TeV analysis, or be lowered to 150 GeV to improve the signal significance for SU4. Table 6.5 shows the number of surviving events for signal and background as the event selection progresses, in addition to the $S/\sqrt{B}$ and S/B ratios. It can be seen that a lower p_T^{jet1} requirement favours the SU4 benchmark point and a higher value for p_T^{jet1} favours the SU3 benchmark point. Since the signal significance for SU4 is high for either choice of p_T^{jet1} threshold, it is concluded that the original inclusive trilepton selection requiring p_T^{jet1} >200 GeV is suitable for use with the very first ATLAS data.

The signal significance as a function of integrated luminosity for SU3 and SU4 at a E_{CM} of 10 TeV is plotted in Figure 6.7. For the original selection with p_T^{jet1} >200 GeV and in the absence

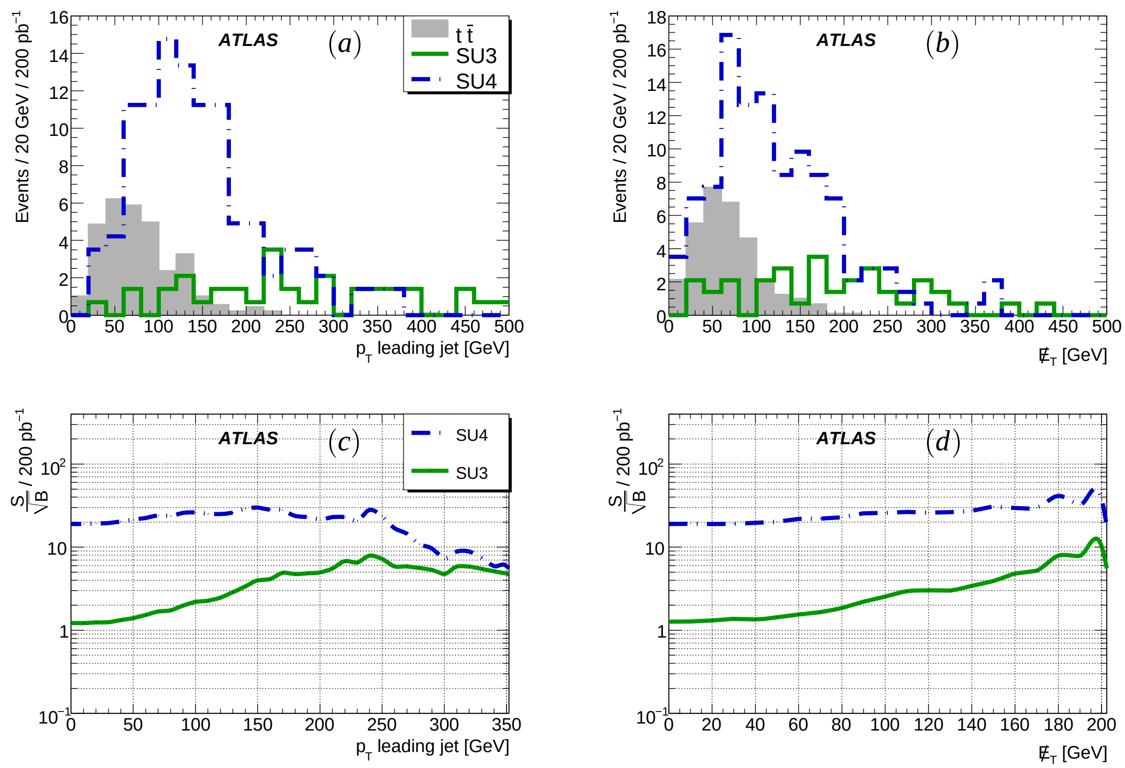

Figure 6.6: The leading jet transverse momentum distribution, *(a)*, and the $\not{E}_T$ distribution, *(b)* for SU3 (*solid line*), SU4 (*dash-dotted line*) and $t\bar{t}$ (*solid grey histogram*) after requiring three leptons in the event. The signal significance $S/\sqrt{B}$ is also shown as a function of the cut on the leading jet transverse momentum, *(c)*, and as a function of the cut on $\not{E}_T$, *(d)*. All distributions are normalised to 200 pb^{-1} of data.

of any systematics not considered here, both SU3 and SU4 achieve a 5σ signal significance within 200 pb^{-1} of data. For completeness, the same curves using the lower p_T^{jet1} >150 GeV threshold are also included, where the discovery potential of the SU3 scenario is seen to degrade. With the very first data from ATLAS, new physics could be discovered in the trilepton plus high-p_T jet channel.

With a general and robust strategy now developed for the trilepton analyses, and excellent reach achieved by both the inclusive and exclusive channels, the focus must now shift to the understanding of systematics and the development of data-driven techniques for SM background estimation. Both these issues will be addressed in the following chapters, where a discussion on systematics is presented in Chapter 7, and techniques to determine levels of $t\bar{t}$ background to a trilepton signal from data are presented in Chapter 8.

	No Cut	N_ℓ	p_T^{jet1} >150 GeV	p_T^{jet1} >200 GeV
SU3	1630.0	7.2	5.5	4.7
SU4	34568.0	107.5	41.4	20.4
$t\bar{t}$	40572.0	32.1	1.9	0.9
$\frac{S}{\sqrt{B}}$	SU3	1.3	4.0	5.0
	SU4	19.0	29.9	21.4
$\frac{S}{B}$	SU3	0.2	2.9	5.2
	SU4	3.3	21.6	22.5

Table 6.5: Number of surviving events for all considered SUSY and SM samples as the inclusive trilepton selection cuts are applied for a centre of mass energy of 10 TeV. Numbers for a lower p_T^{jet1} threshold are shown in addition to the original p_T^{jet1} >200 GeV threshold. The ratios $S/\sqrt{B}$ and S/B are also given. All values are normalised to 200 pb^{-1} of data.

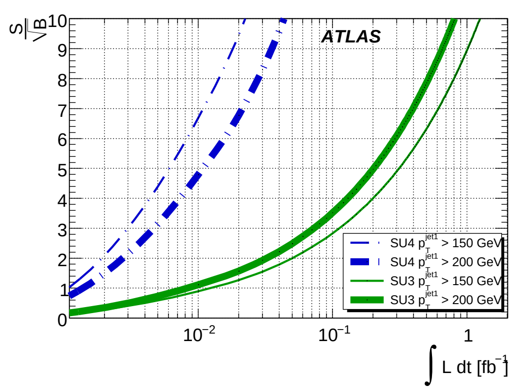

Figure 6.7: The final signal significances $S/\sqrt{B}$ of the inclusive trilepton analysis at a centre of mass energy of 10 TeV as a function of the integrated luminosity $\int \mathcal{L}dt$, for SU3 *(solid)* and SU4 *(dash-dotted)*. The original $p_T^{jet1} > 200$ GeV selection is shown *(thick lines)* in addition to a looser selection of $p_T^{jet1} > 150$ GeV *(thin lines)*.

Chapter 7

Systematic Studies

The dominant source of systematic uncertainties for new physics searches will be the limited knowledge of the SM backgrounds. To understand the SM background contributions to a SUSY signal, data-driven background estimation methods must developed and this has been done for the SUSY trilepton signal as presented in Chapter 8. Equally important will also be the determination from real data of quantities such as lepton identification and reconstruction efficiencies and fake rates. A detailed understanding of the jet energy scale, of the total missing transverse energy, as well as of lepton isolation and impact parameter will also be very important to establish. Full understanding of the systematics, detector, trigger and reconstruction performance of the ATLAS experiment is beyond the scope of this thesis. Although educated guesses may be freely made concerning these issues, they will be based on simulated data and are unlikely to accurately predict the true situation when ATLAS data taking begins. With this in mind, a number of systematic tests have been conducted to assess the effect on the final sensitivity of some of the analysis choices described in Chapter 5, the results of which are presented below. For all previous results quoted in Chapter 6, no systematic effects were taken into account.

7.1 Leptonic Triggers

The high luminosity at the LHC, as discussed in Section 2.2.6, will be far too high to possibly record each and every event. The ATLAS trigger system will be responsible for selecting "interesting" physics events, as defined by the "trigger menus", which is a flexible list of basic signatures that will be used to identify such interesting events. It is vital that the trilepton

Trigger	Event Filter	
	p_T threshold [GeV]	Rate [Hz]
e25i	25	40
mu20i	20	40

Table 7.1: Lepton p_T thresholds and expected trigger rates at 10^{33} cm^{-2}s^{-1} for single electron and muon triggers at EF level.

events and their SM backgrounds, as presented in Chapter 5, pass the trigger menu in place and at suitable rates.

The messy hadronic environment of the LHC makes leptonic triggers preferable in the very early stages of data taking, as high-p_T leptons will be clean, simple objects to trigger on. The basic ATLAS trigger menu contains a number of leptonic triggers - including those that will trigger on single lepton and dilepton events. The single electron and muon triggers are shown in Table 7.1, with the corresponding p_T thresholds and expected rates at Event Filter (EF) level for a luminosity of 10^{33} cm^{-2} s^{-1} [52].

The trigger efficiencies at the EF level have been studied for the trilepton signals and SM backgrounds at each stage of analysis and are presented below. Efficiencies presented are those at "event level", which is an estimation of the percentage of reconstructed events that will pass a given trigger, regardless of which physics object in the event is responsible for the trigger "pass". It is worth noting that an "object-based" study of the trigger, concerned with trigger pass rates of individual physics objects, will be very important for a precise estimation of SUSY trigger pass rates using SM processes for comparison studies. However, such an object based trigger study is not included in this thesis.

The event level trigger efficiency has been evaluated at each stage of the event selection for the isolated electron trigger (`EF_mu20i`), the isolated muon trigger (`EF_em25i`) and their OR-combination (`EF_mu20i` $\cup$ `EF_em25i`). The results for the inclusive and exclusive trilepton analysis, as described in Sections 6.1 and 6.2, are shown in Figure 7.1, where the trigger efficiencies are observed to increase and reach a rough maxima at the three lepton selection stage. Beyond the three lepton event selection stage, the efficiency values plateau, suggesting that the event selection requirements should not bias signal trigger efficiencies. For all the SUSY benchmark points studied, high trigger efficiencies are observed, supporting the view that the leptonic triggers currently in the trigger menu should be sufficient for a trilepton SUSY analysis.

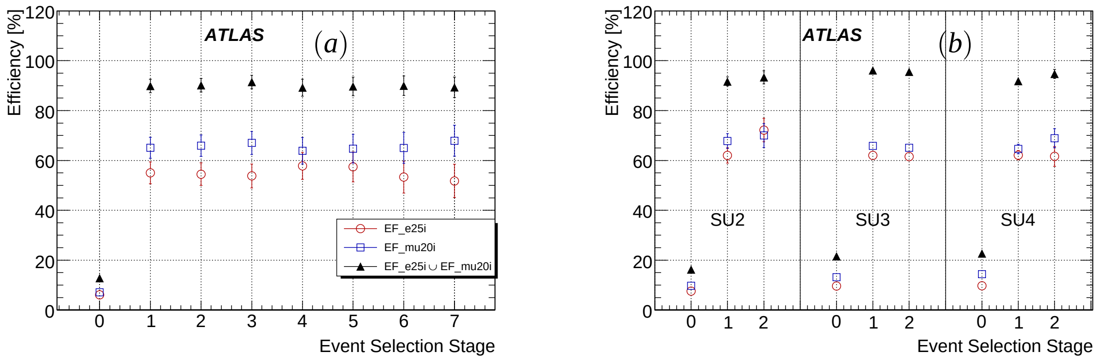

Figure 7.1: Signal trigger efficiencies for the three SUSY benchmark points, shown as a function of progressive selection stages of the exclusive (a) and inclusive (b) trilepton analyses.

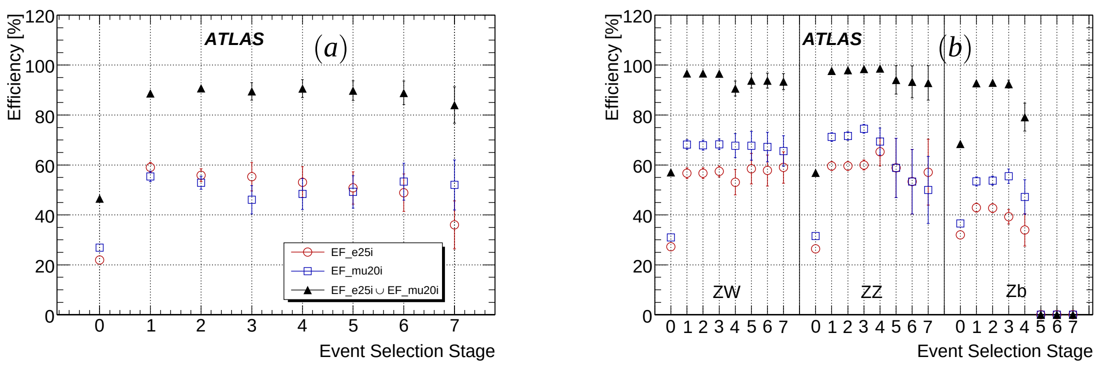

Figure 7.2: Dominant SM background trigger efficiencies, shown as a function of progressive selection stages of the exclusive trilepton analysis for (a) $t\bar{t}$ and (b) diboson and Zb backgrounds.

It is crucial that SM backgrounds also pass the ATLAS trigger with high enough rates to allow an understanding of SM background to a trilepton SUSY analysis. The trigger efficiency results for the dominant SM backgrounds as the exclusive trilepton event selection is applied are presented in Figure 7.2. It is clear that the individual `EF_mu20i` and `EF_em25i` trigger efficiencies are much lower in Figure 7.2(a) than for the SUSY signals in Figure 7.1, however, the OR-combination of the two triggers is seen to be relatively large. In Figure 7.2(b), the multiplicative effect of a more efficient muon trigger is seen from muon decays of the Z, as well as a drop in efficiency after the Z mass window requirement.

From this study of the event level trigger efficiency for the SUSY signals and the SM backgrounds it can be concluded the single isolated lepton triggers should work well for the trilepton analyses. It must be noted that the trigger efficiencies found here were not included in the calculation of the signal significances for the inclusive and exclusive trilepton analyses in Chapter 6. As the LHC increases the initial luminosity to the design luminosity, a large effort will be required to understand and control the ATLAS trigger rates by making changes in the flexible trigger menu. This may result in raising the p_T threshold of the lepton triggers to keep trigger rates down, driving the need for the study of combined triggers. A possibility relevant for the trilepton inclusive analysis could be a “lepton+jet” trigger where the lepton p_T threshold can remain low to maximise acceptance for certain physics scenarios. However, until such a scenario occurs, the isolated single electron and muon triggers are found to provide a simple and robust option for an early physics programme [53].

7.2 Signal Significance Definition

The signal significance is a defining quantity of an analysis and gives a measure of the results obtained occurring by chance. The general strategy and conclusions of an analysis should not depend heavily on the precise definition of the signal significance, providing a sensible definition is used.

The expected signal significance used in previous sections for optimising the inclusive and exclusive trilepton selections is:

$$Z_1 = \frac{S}{\sqrt{B}} \tag{7.1}$$

This definition, Z_1, is always valid in the Gaussian case, when both S and B are much greater than unity. However, in the Poisson case, Z_1 is an approximate formula and only valid in the limit $S \ll B$ and when S and B are assumed to be known exactly. It was seen in the inclusive trilepton analysis for the SU3 and SU4 points, the number of signal events far exceeds the number of background events, rendering the use of Z_1 unsuitable. A more general definition of the signal significance is clearly needed, since neither the number of signal or background events will be known exactly when dealing with “real” data.

For the more general case, when B can be small compared to S, the appropriate formula to use for signal significance in the Poisson limit [54] is:

$$Z_2 = \sqrt{2\left((S+B)\ln\left[1+\frac{S}{B}\right] - S \right)}\ . \tag{7.2}$$

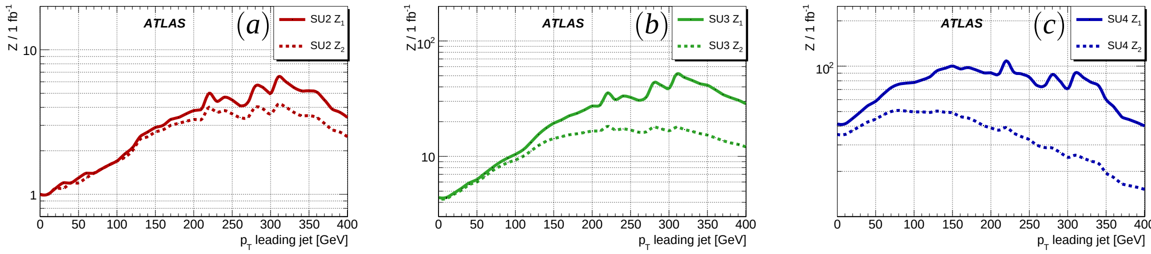

Figure 7.3: The effect of the definition of signal significance on the inclusive trilepton analysis. Z_1 and Z_2 are plotted as a function of the cut on the leading jet transverse momentum p_T^{jet1} for the SU2 *(a)*, SU3 *(b)* and SU4 *(c)* inclusive trilepton analyses. All plots are for an integrated luminosity of 1 fb^{-1}.

When $S \ll B$, as in the case of the exclusive trilepton analysis, Z_2 is well approximated by Z_1 and it makes little difference which of the two definitions is used. However, in the case of the inclusive trilepton analysis, where $S > B$, the two definitions of signal significance will take differing values, which may have important effects when optimising event selection or quoting the analysis discovery potential. In order to evaluate this effect, the selection requiring a high-p_T jet in the inclusive analysis presented in Sections 5.2 and 6.1 is revisited. The two calculations of signal significance, Z_1 and Z_2, are plotted as a function of p_T^{jet1} in Figure 7.3(a)-(c) for comparison. It is seen that the curves for Z_2 are much smoother than the curves for Z_1 and therefore less affected by statistical fluctuations in the SM backgrounds. Despite this observed difference in the Z_1 and Z_2 curves, the selection of a high-p_T jet remains unchanged. Generally, the signal significance curves are not greatly influenced by the new definition and a cut at $p_T^{jet1} > 200$ GeV is confirmed as a reasonable compromise between achieving optimal significance for each benchmark point and fine-tuning the event selection.

To assess the importance of the signal significance definition on the analysis discovery potential, both Z_1 and Z_2 are plotted as a function of integrated luminosity in Figure 7.4 for the exclusive and inclusive analyses. For the exclusive analysis at SU2, due to the low S/B ratio, Z_1 is a good approximation for Z_2 and the result that approximately 15-20 fb^{-1} would be needed for a 5σ discovery in that channel is confirmed. The expectation that the difference between the two definitions will be greater as S/B increases [54] is confirmed as Z_1 appears to underestimate the amount of data needed for a 5σ inclusive trilepton discovery (in absence of other systematic effects), an effect that is even more prominent for the high S/B scenarios SU3 and SU4. Nonetheless, the conclusions reached in previous sections remain sound, as it is observed that a

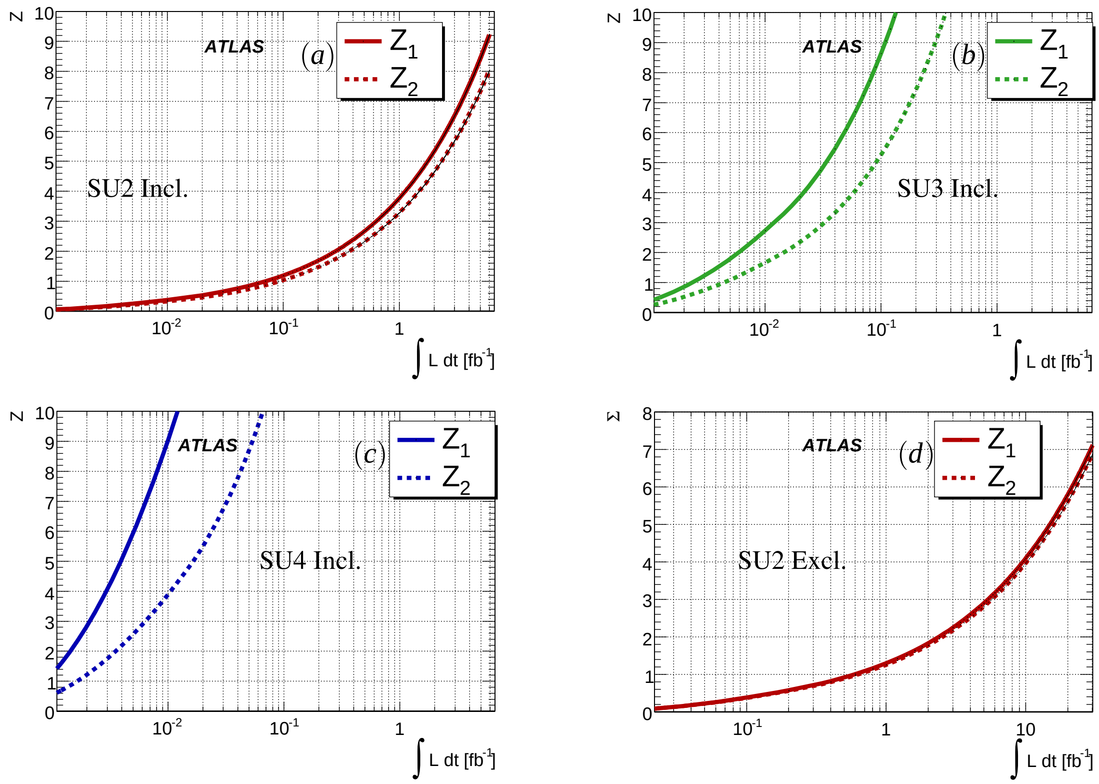

Figure 7.4: A comparison of the two definitions for signal significance, Z_1 and Z_2. Signal significance vs. integrated luminosity is shown for the SU2 inclusive (a), SU3 inclusive (b), SU4 inclusive (c), and SU2 exclusive (d) analyses.

5σ discovery could be made in the inclusive trilepton channel with between a few hundred pb^{-1} and a few fb^{-1} worth of data, depending on the SUSY benchmark scenario considered and in the absence of other systematic effects.

7.3 The lepton p_T threshold

In Section 5.1 it was noted that the leptons in the trilepton analyses appear, on average, to have lower p_T values than for other leptonic SUSY channels - a feature which is particularly true for the third lepton. This observation of softer p_T leptons drives the need for the 10 GeV lepton threshold used throughout these analyses, in contrast to the harder default values used in other SUSY analyses involving leptons [31].

To evaluate the effect that this lower lepton threshold has on the final signal significances of the analyses, the p_T threshold of each of the three leptons is systematically raised from 10 GeV to

p_T threshold [GeV]			Inclusive [1 fb^{-1}]						Exclusive [10 fb^{-1}]	
$1^{st}\ell$	$2^{nd}\ell$	$3^{rd}\ell$	SU2		SU3		SU4		$\tilde{\chi}\tilde{\chi}$	
			Z_1	Z_2	Z_1	Z_2	Z_1	Z_2	Z_1	Z_2
10	10	10	3.8	3.3	27.3	16.6	90.3	38.9	4.1	3.9
15	10	10	3.8	3.3	27.3	16.6	90.3	38.9	4.0	3.9
15	15	10	3.8	3.3	27.6	16.4	90.8	38.5	3.9	3.8
15	15	15	2.8	2.5	22.4	14.0	63.3	29.6	3.6	3.4

Table 7.2: The effect of raising the lepton p_T threshold from 10 GeV to 15 GeV on the final signal significance (both Z_1 and Z_2 are given) for the inclusive and exclusive trilepton analyses. Numbers are quoted for 1 fb^{-1} or 10 fb^{-1} for the inclusive or the exclusive analysis, respectively.

15 GeV and the results can be seen in Table 7.2. It is clearly seen that the final significance for all benchmark scenarios is only marginally affected by raising the p_T threshold for the leading two leptons to 15 GeV. However, when the p_T threshold for the third lepton is also raised to 15 GeV, the final signal significances are degraded substantially by up to $\sim 30\%$. This consequence seems to suggest that, should there be a need to raise the lepton p_T threshold for some reason, especially at the start of data-taking, it may be possible to do so for the two leading leptons without any major consequences on the analysis. On the other hand, maintaining the lower p_T threshold for the third lepton appears to be rather important, especially in a heavy SUSY scenario.

7.4 Varying the Inclusive Event Selection

A systematic study has been performed to understand the effect of the various possible event selection requirements and their combinations on the final signal significance of the inclusive analysis. In Section 5.2, it was seen that a potential event selection using $\not{E}_T$ instead of a high-p_T jet is feasible, however, a degradation in signal significance would be seen for the three SUSY scenarios considered. Despite this, an $\not{E}_T$ selection is investigated here, using a threshold of 150 GeV, which has been decided by looking at where the signal significance is maximal for all three SUSY scenarios in Figure 5.3(b). In Section 5.3, lepton track isolation was seen to be a powerful discriminant against $t\bar{t}$ and Zb SM backgrounds in the exclusive trilepton analysis. Therefore, the effect of including a stringent lepton track isolation in the selection has also been investigated.

Combinations of p_T^{jet1} threshold, $\not{E}_T$ and lepton track isolation have been applied in an attempt to assess the relative importance of an individual requirement as well as any correlation

Set	p_T^{jet1}	$\not{E}_T$	Track Isolation	Z_1			Z_2		
				SU2	SU3	SU4	SU2	SU3	SU4
1	√	×	×	3.8	27.3	90.3	3.3	16.6	38.9
2		√	×	2.3	17.7	81.0	2.1	13.0	40.7
3	×	×	√	1.2	4.6	36.4	1.2	4.4	30.4
4		√	√	2.6	21.2	82.7	2.3	13.5	36.1
5		√	×	4.7	40.4	95.8	3.6	18.2	32.3
6	√	×	√	4.5	35.9	107.1	3.6	17.5	36.6
7		√	√	4.2	38.6	79.0	3.2	16.5	26.5

Table 7.3: The signal significances Z_1 and Z_2 as different combinations of event selection requirements are applied for the inclusive analysis (√/× stands for applied/not applied). Numbers are normalised to 1 fb^{-1}.

between them. Both signal significance definitions discussed in Section 7.2, Z_1 and Z_2, are given in Table 7.3 for each combination of the three selection requirements. The first line (Set 1) corresponds to the default inclusive trilepton selection, as reported in Section 6.1, where just the three lepton and p_T^{jet1} requirements are applied. Sets 2-4 show combinations of cuts where no p_T^{jet1} requirement is applied, but requirements on $\not{E}_T$ and/or the lepton isolation requirement are applied. Finally, Sets 5-7 in Table 7.3 show combinations of cuts where the p_T^{jet1} requirement is applied along with the $\not{E}_T$ and/or the lepton isolation requirement.

Comparing Set 1 and Set 2 in Table 7.3 confirms the fact that an inclusive trilepton selection relying on the presence of a high-p_T jet is generally more powerful than one relying on $\not{E}_T$ alone, in particular for the SU2 and SU3 benchmark scenarios. Set 5 shows that the combination of a cut on p_T^{jet1} and $\not{E}_T$ yields a better significance for the SU2 and SU3 benchmark points, suggesting that the addition of a cut on $\not{E}_T$ to the baseline selection may be an interesting option to explore, but not until a time when the systematics on $\not{E}_T$ will have been fully understood. Similar conclusions can be drawn for lepton track isolation, which in Sets 6 and 7 is shown to improve the signal significance, if combined with cuts on p_T^{jet1} and/or $\not{E}_T$. Sets 3 and 4, however, show that the lepton track isolation performs badly on its own, or in combination with $\not{E}_T$ only, for all three SUSY points. It is important to note that adding extra cuts to the one chosen for the baseline selection, would not only complicate the estimation of systematic effects, but also further reduces the statistics of the MC samples used.

In conclusion, from Table 7.3 it can be reasoned that any cut combination that does not implement the high p_T jet selection is generally less effective than a selection applying a cut on the leading jet p_T alone, or in combination with other cuts. Indeed, the baseline selection described in Section 5.2 appears to be the best compromise between a simple and robust selection and achieving the best sensitivity for all considered SUSY scenarios.

7.5 Varying the Exclusive Event Selection

The effect of removing one or more cuts from the default selection for the exclusive analysis as presented in Section 6.2 has also been studied in a similar fashion to that for the inclusive analysis in Section 7.4. The final signal significances, Z_1 and Z_2, for different combinations of cuts are shown in Table 7.4. Due to the importance of the jet veto and IP_N selections in isolating the $\tilde{\chi}\tilde{\chi}$ pair component, different combinations of cuts in the table have been organised into groups (A to D), depending on which combination of the jet veto and/or of the IP_N cuts is applied. Additionally, within each group, sets of cuts have been numbered (e.g. A1 to A5), to indicate which cut is being removed from the selection. The default exclusive trilepton selection as presented in Section 6.2 corresponds to the first line in the table, Set A1.

By studying Table 7.4 a number of important observations can be made: firstly, that removing the jet veto does not impact the signal significance greatly, as long as the IP_N cut is kept in the selection, as seen when comparing Set A1 and Set C1. Indeed, there is a substantial drop in the significance if the IP_N cut is removed, even in the case when a jet veto is kept in the selection, which can be seen when Sets A1, C1 are compared with Sets B1, D1. This difference is attributed to the the fact that the IP_N selection is more effective at removing $t\bar{t}$ events than the jet veto is at removing SUSY background events.

From the comparison of Sets A5, B5, C5, D5 with the default Set A1 in Table 7.4, it is noted that when the $\not{E}_T$ cut is removed from the selection, irrespective of whether the jet veto and/or the IP_N cut are kept or not, the signal significance drops approximately by the same amount. In the same manner, removing the SFOS requirement (A2, B2, C2 and D2) has similar consequences on the signal significance, regardless of the choice made on the jet veto and, to some extent, the IP_N cut. This is attributed to the precise background targeting of these two cuts: the $\not{E}_T$ selection removes diboson events with little/no $\not{E}_T$ and the SFOS selection removes events with random lepton flavour-pair combinations. These background events are clearly not very well removed by any other selection in the analysis, indicating that there is a small correlation between the SFOS/$\not{E}_T$ selections and the rest of the exclusive trilepton selection.

	Set	SFOS	Track Isol.	Z-Window	$\not{E}_T$	Jet Veto	IP_N	Z_1	Z_2
	A1	√	√	√	√	√	√	4.1	3.9
	A2	×	√	√	√			3.8	3.7
Jet Veto + IP_N	A3	√	×	√	√	√	√	2.9	2.8
	A4	√	√	×	√			2.5	2.5
	A5	√	√	√	×			3.4	3.3
	B1	√	√	√	√			3.6	3.6
	B2	×	√	√	√			3.4	3.4
Jet Veto + No IP_N	B3	√	×	√	√	√	×	2.4	2.4
	B4	√	√	×	√			2.3	2.3
	B5	√	√	√	×			3.2	3.1
	C1	√	√	√	√			4.0	3.9
	C2	×	√	√	√			3.8	3.7
No Jet Veto + IP_N	C3	√	×	√	√	×	√	2.9	2.9
	C4	√	√	×	√			3.0	3.0
	C5	√	√	√	×			3.5	3.5
	D1	√	√	√	√			3.5	3.4
	D2	×	√	√	√			3.4	3.3
No Jet Veto + No IP_N	D3	√	×	√	√	×	×	2.4	2.3
	D4	√	√	×	√			2.8	2.8
	D5	√	√	√	×			3.2	3.2

Table 7.4: The signal significances Z_1 and Z_2 as different combinations of the exclusive event selection requirements are applied ($\surd/\times$ stands for applied/not applied). Numbers are normalised to 10 fb^{-1}.

The individual requirements in the exclusive trilepton event selection identified as having the most impact on the signal significance for the exclusive trilepton analysis are lepton track isolation (Sets A3, B3, C3 and D3) and the Z mass window (Sets A4, B4, C4 and D4) requirement. Clearly, both these requirements are responsible for the largest changes in signal significance, which is not so surprising considering the very large amounts of SM backgrounds they each remove.

7.6 Varying the Background Normalisation

As mentioned at the beginning of this chapter, the understanding of SM backgrounds is a crucial part of any new physics analysis. Indeed, the fact that the Monte Carlo background samples used in this analysis may not correctly model the rate of production nor the shape of the distributions must be acknowledged and addressed. A test is conducted to study the dependence of the final total significance on the overall background level, by increasing the MC SM backgrounds between one and three times their original levels. Although this test will not take into account the possibility that the shape of the background distributions may not be well reproduced by the MC or that the limited sample statistics could result in the overemphasis of the few surviving events, it will serve to check the robustness of the trilepton analyses to a rise in background levels. A detailed study into data-driven background estimation methods can be found in Chapter 8.

The final signal significance, Z_1, for the default inclusive and exclusive analyses is plotted in Figure 7.5 as a function of the overall level of the dominant SM backgrounds as the normalisations of the $t\bar{t}$ and ZW samples have been rescaled by a factor between one and three times their original levels. It is observed in Figure 7.5(a)-(c) that for the inclusive analysis, due to the very low number of surviving ZW events, the signal significance is not greatly impacted by changes in the diboson normalisation. However, a threefold increase in the overall level of the more dominant $t\bar{t}$ background would change the signal significance by almost a factor of two. The same plot for the exclusive trilepton analysis is seen in Figure 7.5(d), where both the ZW and $t\bar{t}$ backgrounds contribute almost in equal measure to the final background level. A threefold increase in normalisation of either the ZW or $t\bar{t}$ samples would result in a $\sim 30\%$ reduction in the final signal significance. Analogous plots for Z_2 are presented in Figure 7.6$(a)-(d)$, where, although the vertical scale is in general different between these plots and those in Figure 7.5, the overall trend is the same.

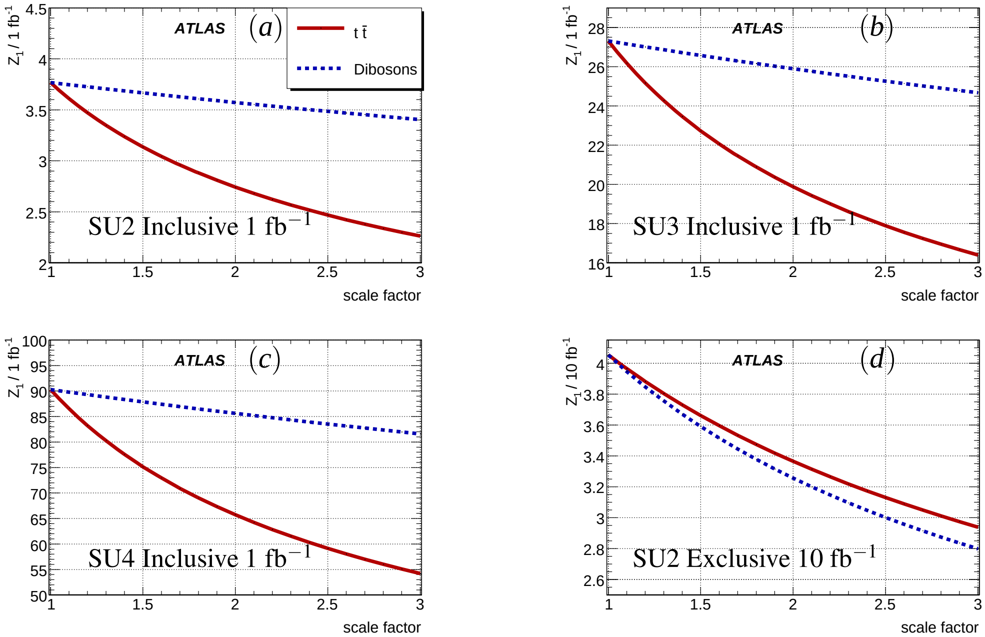

Figure 7.5: The change in the signal significance Z_1 for the inclusive *(a-c)* and the exclusive *(d)* selections, as the background level is rescaled to between one and three times its original level, for $t\bar{t}$ *(solid)* and dibosons *(dashed)* separately.

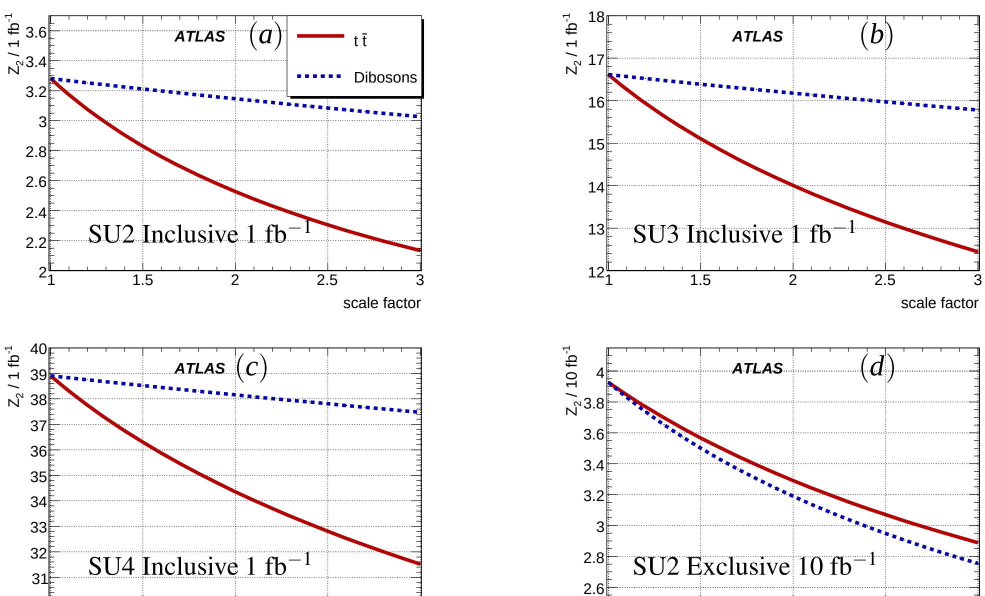

Figure 7.6: The change in the signal significance Z_2 for the inclusive *(a-c)* and the exclusive *(d)* selections, as the background level is rescaled to between one and three times its original level, for $t\bar{t}$ *(solid)* and dibosons *(dashed)* separately.

In summary, both the inclusive and exclusive trilepton analyses have been found to be robust to the various systematic tests performed here. The single leptonic triggers should select trilepton events with very good efficiency, while a more precise signal significance definition is seen to uphold the selection strategies developed and general conclusions reached. The option of raising the lepton p_T threshold for the trilepton analyses to 15 GeV is seen to be possible for the leading two leptons in the events, but not for the third, much softer lepton. The event selection for both the inclusive and exclusive analyses has been systematically varied where the impact of each individual cut has been assessed and correlations identified. Finally, the possibility of the SM backgrounds fluctuating up to three times of the MC predictions has been considered. A discussion of methods to determine the levels of the SM backgrounds from data instead of relying on (possibly inaccurate) MC predictions are discussed and explored in the following chapter.

Chapter 8

Data Driven Background Estimations

The current Monte Carlo simulations of physics processes at the LHC are unlikely to describe accurately what will be seen at the unprecedented centre of mass energies of the LHC. Not only will background rates need to be measured from data, the shapes of kinematic distributions will have to be understood in detail, especially in regions where they could impact the search for new physics. For every SUSY channel data driven methods will have to be developed to estimate individual background rates. The feasibility of several data driven methods to estimate SM backgrounds to a SUSY trilepton signal are investigated in this chapter. This work is still in its early stages and it is acknowledged that further, in depth studies will be needed in order to establish robust techniques to be implemented for ATLAS data. While work on these issues is anticipated to continue in the future, interesting preliminary studies have been obtained and are presented here.

It was seen in Chapter 6 that $t\bar{t}$ and ZW production are the dominant SM backgrounds for both the inclusive and exclusive trilepton analyses. Thus, methods to estimate these backgrounds have been investigated and are presented in what follows. For the exclusive analysis $t\bar{t}$ background estimation, two methods are presented: one that "reverses" the lepton track isolation requirements to obtain a control sample of $t\bar{t}$ background events, and a second method that aims to exploit the differences in lepton flavour and sign combinations between signal and background. Data driven $t\bar{t}$ background estimations for the inclusive trilepton analysis are comparatively more difficult because, due to the sheer simplicity of the analysis itself, it is more difficult than for other inclusive channels to define clear boundaries between "signal" and "background" regions (one reason being that the classic SUSY requirement on $\not{E}_T$ is not applied). However, a previously existing method has been adapted to the trilepton case that relies on solutions to top quark reconstruction algorithms. Finally, ideas for a data driven method to estimate the ZW background to an inclusive or exclusive trilepton SUSY signal are presented.

8.1 Estimates for the Exclusive Trilepton Analysis

Top pair production is a major background to the exclusive analysis presented in Section 6.2, which searches for trilepton final states from direct gaugino pair production. Two data driven methods to estimate levels from this source of background have been developed, which exploit the randomness of lepton flavour-sign combinations produced from $t\bar{t}$ decays. The reader will recall from Section 5.3 that, as part of the exclusive trilepton event selection, a SFOS lepton pair is demanded to be present among the three leptons, since two of the leptons in the SUSY signal are from a $\tilde{\chi}_2^0$ decay and must be SFOS. There is no such flavour constraint for the leptons in $t\bar{t}$ events. However, as both of the W bosons should be decaying leptonically, a OS lepton pair must still be present [55].

The possible trilepton flavour-sign combinations are listed in Table 8.1 for $t\bar{t}$ and the SUSY signal, where it can be seen that the expected relative rates of certain combinations is different. An OS lepton pair is expected from a $t\bar{t}$ trilepton event from the two leptonic W decays, while the third lepton of any sign or flavour would come from a leptonic b-quark or $\bar{b}$-quark decay. Thus, combinations 13 through to 20 obtained from data are not expected to originate from $t\bar{t}$ trilepton events. For the signal, a SFOS lepton pair is expected from the $\tilde{\chi}_2^0$ decay, so in principle, only combinations 5-12 are expected to contribute to trilepton $\tilde{\chi}\tilde{\chi}$ events. On the other hand, combinations 5-8 for $t\bar{t}$ have two candidates for the lepton from the b-quark decay and so their contributions must be doubled. The differing relative contributions within combinations 5-12 for the $\tilde{\chi}\tilde{\chi}$ signal reflect the charge asymmetry in pp interactions, where the cross-section for the production of $\tilde{\chi}_2^0\tilde{\chi}_1^+$ will be greater than $\tilde{\chi}_2^0\tilde{\chi}_1^-$. Since the gauginos are the supersymmetric partners of the SM gauge bosons, it is reasonable to assume the ratio of their cross-sections should follow $\sigma(pp \rightarrow ZW^+) \;/\; \sigma(pp \rightarrow ZW^-) \;\sim\; 1.6$ [31], hence the value of the weights.

As an initial cross check, the generator level information of the $t\bar{t}$, ZW and SU2 samples has been accessed and where three stable generator leptons (electrons or muons) from $W^{\pm}$, Z, τ or SUSY decays (and b-quark decays in the case of $t\bar{t}$) are present in the event, the lepton flavours

Combination			Relative contribution to σ_{3lep}	
			$t\bar{t}$	$\tilde{\chi}\tilde{\chi}$
With OS pair	1	$e^-\mu^+\mu^+$	1.0	0.0
	2	$\mu^-e^+e^+$	1.0	0.0
	3	$e^+\mu^-\mu^-$	1.0	0.0
	4	$\mu^+e^-e^-$	1.0	0.0
With SFOS pair	5	$e^+e^-\mu^-$	2.0	1.0
	6	$e^-e^+\mu^+$	2.0	1.6
	7	$\mu^+\mu^-e^-$	2.0	1.0
	8	$\mu^-\mu^+e^+$	2.0	1.6
	9	$e^+e^-e^-$	1.0	1.0
	10	$e^-e^+e^+$	1.0	1.6
	11	$\mu^+\mu^-\mu^-$	1.0	1.0
	12	$\mu^-\mu^+\mu^+$	1.0	1.6
With no OS pair	13	$e^+e^+e^+$	0.0	0.0
	14	$e^-e^-e^-$	0.0	0.0
	15	$\mu^+\mu^+\mu^+$	0.0	0.0
	16	$\mu^-\mu^-\mu^-$	0.0	0.0
	17	$e^+e^+\mu^+$	0.0	0.0
	18	$e^-e^-\mu^-$	0.0	0.0
	19	$\mu^+\mu^+e^+$	0.0	0.0
	20	$\mu^-\mu^-e^-$	0.0	0.0

Table 8.1: Possible lepton flavour-sign combinations in trilepton events. Expected weights for each combination are given for $t\bar{t}$ and $\tilde{\chi}\tilde{\chi}$ decays.

and signs are recorded. The obtained generator level lepton flavour-sign combinations found in trilepton events is shown in Figure 8.1, where the relative contributions predicted in Table 8.1 are confirmed within statistical uncertainties. The increased contributions from combinations 5-8 in the $t\bar{t}$ distribution is clearly seen, as is the lack of many events with combinations 13-20. The distribution for ZW trilepton event flavour-sign combinations is also shown in Figure 8.1. ZW has been treated in this case as a "signal-like" sample with higher statistics, to be compared to the SUSY direct gaugino events. Both ZW and SU2 $\tilde{\chi}\tilde{\chi}$ trilepton events are dominated by combinations 5-12, and the relative differences in combinations 6,8,10,12 compared to combinations 5,7,9,11 agrees reasonably well with the prediction from $\sigma(pp \to ZW^+)$ / $\sigma(pp \to ZW^-)$. The handful of SU2 direct gaugino events with combinations 13-20 are comprised of $\tilde{\chi}_4^0\tilde{\chi}_2^\pm$ events that decay via long chains of neutralinos, charginos, W bosons, Z bosons and τ leptons, resulting in rare same-sign three lepton final states.

The lepton flavour-sign combinations of trilepton events are now well understood for the

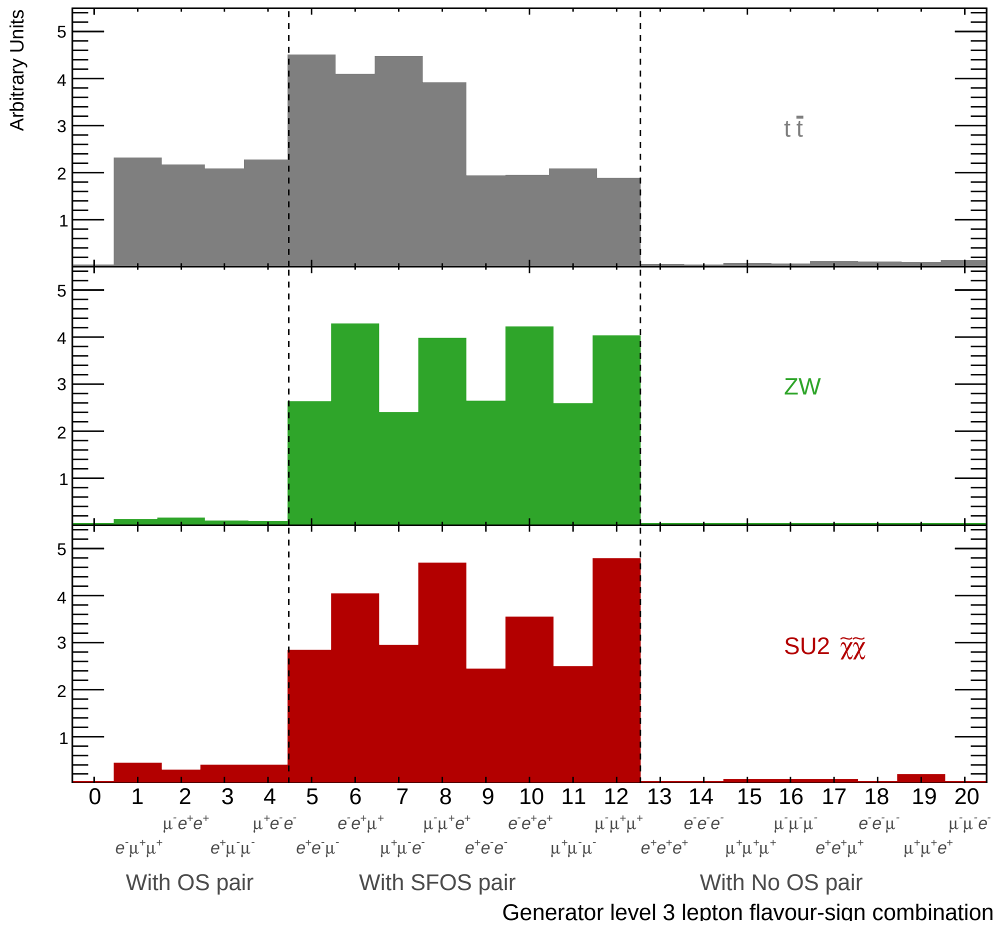

Figure 8.1: The trilepton flavour-sign combinations as found using generator level information in for $t\bar{t}$, ZW and SU2 signal. The dashed vertical lines separate the "signal" region from the "control" region. All distributions are normalised to arbitrary values.

direct-gaugino SUSY signal and the $t\bar{t}$ background. The presence of $t\bar{t}$ trilepton events with combinations 1-4 (with OS lepton pair), and the relative lack of SUSY signal events with these combinations creates a control region which may be used for background estimation. The exclusive trilepton analysis selection includes the requirement of a SFOS lepton pair in the event, leading to combinations 5-12 becoming the signal region in which to estimate the background contribution. Since the relative contributions of lepton flavour-sign combinations of $t\bar{t}$ events are understood, the events in the control region can be counted and used to predict the number of events in the signal region. Using generator level information only, the number of $t\bar{t}$ events in the signal region should be three times that in the control region.

The picture changes dramatically when lepton identification and reconstruction are taken into

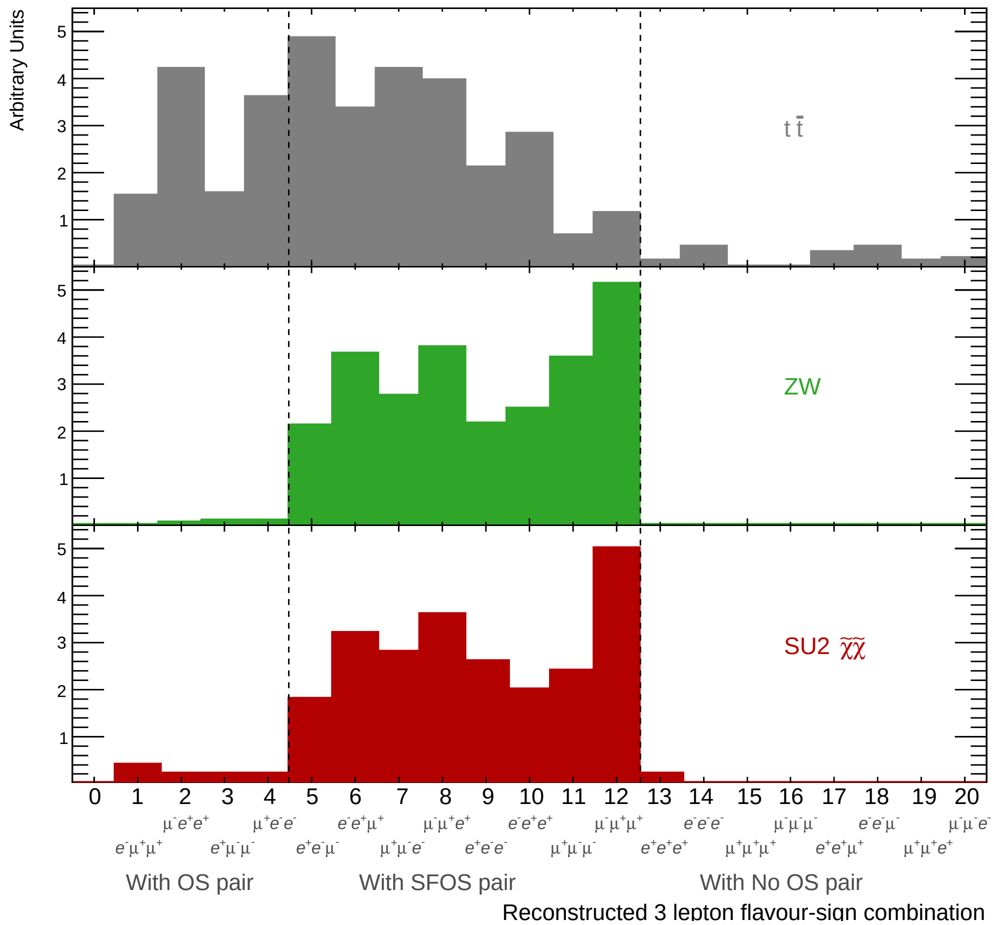

Figure 8.2: The trilepton flavour-sign combinations as found using fully reconstructed events for $t\bar{t}$, ZW and SU2 signal. The dashed vertical lines separate the "signal" region from the "control" region. All distributions are normalised to arbitrary values.

account, as shown in Figure 8.2, where the fully reconstructed lepton flavour-sign combinations are plotted for $t\bar{t}$, ZW and SU2 $\tilde{\chi}\tilde{\chi}$ trilepton events. Intrinsic differences in electron and muon reconstruction change the relative contributions of each lepton flavour-sign contribution compared to that seen at generator level. Indeed, the higher electron fake rate compared to that of muons, seen in Table 4.3, will tend to increase the contribution from combinations containing electrons. Simultaneously, the lower electron reconstruction efficiency compared to that of muons will tend to reduce the contribution from combinations containing electrons. The overall number of observed leptons will be determined by the combined effect of these two competing tendencies.

8.1.1 Reversing the Lepton Track Isolation

As part of the exclusive trilepton analysis in Section 5.3 it was seen that the requirement of strict lepton track isolation was excellent at discriminating against the $t\bar{t}$ background. Indeed, only 23 % of $t\bar{t}$ events survive the lepton track isolation requirement, suggesting that lepton track isolation may be a suitable variable with which to create a control region for background estimation. However, the lepton track isolation requirement also removes much of the Zb background, and so a control region based solely on events that fail this requirement would be comprised not only of $t\bar{t}$ events, but also an overwhelming number of Zb events. Any Zb (or other SM background) contamination in the control region may be reduced by considering only trilepton events that have passed the Z mass window, $\not{E}_T$, jet veto and lepton impact parameter requirements for the background estimation, where the only major surviving backgrounds are ZW and $t\bar{t}$ itself.

The $t\bar{t}$ events may be distinguished from the other SM events that fail the lepton track isolation requirement by exploiting the lepton flavour-sign combinations, since a SFOS lepton pair is expected to be present in the three leptons from SM events containing a Z boson. A relatively pure control sample of $t\bar{t}$ events may be isolated by requesting that no SFOS lepton pair is present amongst the three leptons, and by reversing the lepton track isolation ($p_T^{max} > 1,\ 2$ GeV for $\mu,\ e$ respectively). The signal region can be defined as the events that pass the SFOS and lepton track isolation requirements. The events that pass only one and fail the other of the SFOS and lepton track isolation requirements may be used as normalisation regions. In Figure 8.3, the method for defining the signal and control regions for this $t\bar{t}$ background estimation is shown, where each region has been labelled A to D.

Trilepton $t\bar{t}$ events with no SFOS pair should display the same lepton track isolation distribution as those with a SFOS lepton pair, since there is no intrinsic difference in the origin of the leptons. In Figure 8.4, the distributions for both electron and muon track isolation are plotted for $t\bar{t}$ trilepton events with and without a SFOS lepton pair that have passed the Z mass window, $\not{E}_T$, jet veto and lepton impact parameter requirements. It can be seen that the shapes of the lepton track isolation distributions are the same for events with and without a SFOS lepton pair. Since the distributions follow the same shape, then the ratio of the number of events on either side of the p_T^{max} cut should also be equal. By comparing the ratios of events with each cut combination, then the number of $t\bar{t}$ events that passed both the SFOS and lepton track isolation requirements may be found.

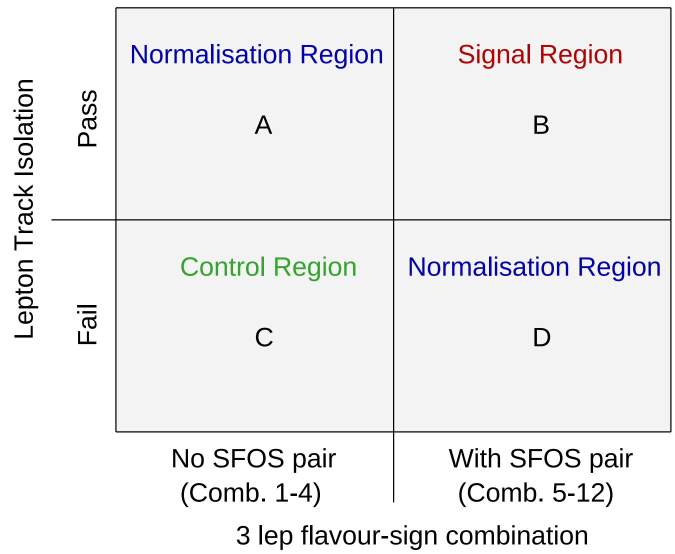

Figure 8.3: The definition of the control region, signal region and normalisation regions using lepton track isolation and lepton flavour-sign combinations for the estimation of the $t\bar{t}$ background to the exclusive trilepton signal, as described in the text.

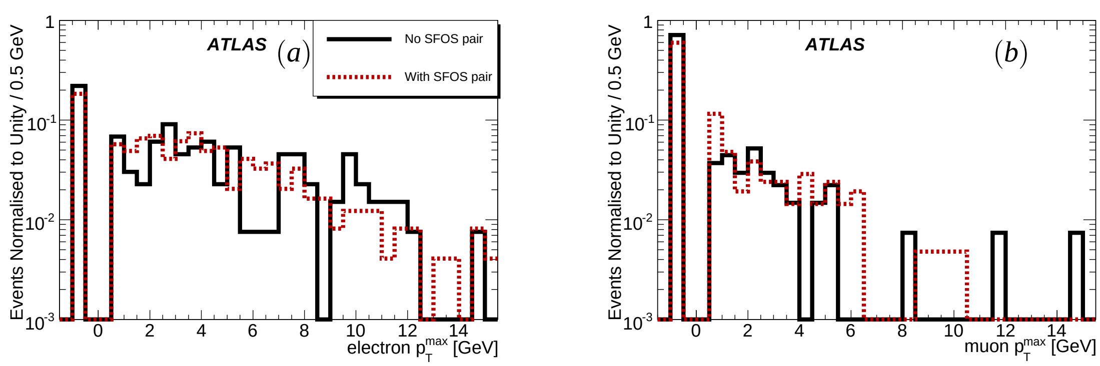

Figure 8.4: Lepton track isolation, p_T^{max}, for electrons *(a)* and muons *(b)* in $t\bar{t}$ trilepton events that have passed the Z mass window, $\not{E}_T$, jet veto and lepton impact parameter requirements and either failed or passed the SFOS lepton pair requirement. Entries in the $p_T^{max} = -1$ GeV bin correspond to cases where no other track was found around the lepton tracks in the event. All distributions are normalised to unity.

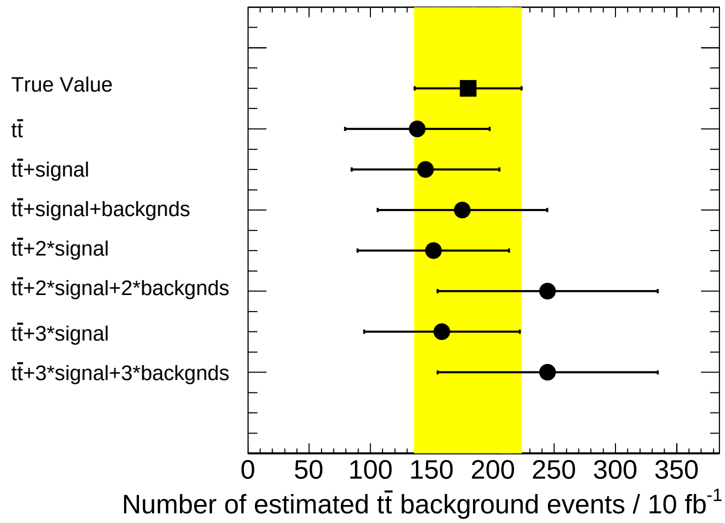

Figure 8.5: Estimation of the $t\bar{t}$ background to the exclusive trilepton signal using a reversal of the lepton track isolation and SFOS requirements, including contaminations from the SUSY signal and other SM backgrounds. All results are normalised to 10 fb^{-1} of data.

The number of events in the signal region (B) can be estimated using the number of events in the control region (C) and the normalisation regions (A and D), by assuming the ratio of events in A and C is the same as the ratio of events in B and D. Thus:

$$N_B = \frac{N_A}{N_C} \times N_D, \tag{8.1}$$

where N_B is the number of events that pass both the SFOS and lepton track isolation requirement; N_A is the number of events that fail the SFOS requirement but pass the lepton track isolation requirement; N_C is the number of events that fail both the SFOS and lepton track isolation requirement; and N_D is the number of events that pass the SFOS requirement but fail the lepton track isolation requirement, as depicted in Figure 8.3.

The results for the estimation of the $t\bar{t}$ background to the exclusive trilepton signal using reversed lepton track isolation and SFOS lepton requirements are shown in Figure 8.5, where the true value is plotted along with estimations with varying levels of contamination present. Only trilepton events that have passed the Z mass window, $\not{E}_T$, jet veto and lepton impact parameter requirements have been considered for this method. The positive and negative event weights associated with the $t\bar{t}$ and Zb samples have been taken into account here, by finding the fraction of unweighted events in each region (A-D) and applying this to the weighted events. The number of $t\bar{t}$ events in the signal region has been predicted using Equation 8.1, and is seen to be in very good agreement with the true value. The additional presence of one to three times the original levels of SUSY signal and other surviving SM backgrounds still results in a measurement that is compatible with the true value, within errors. This technique to estimate the $t\bar{t}$ background for the exclusive trilepton analysis has here proved to be a successful method to obtain a prediction for the number of $t\bar{t}$ events from real data.

In the following section, a method that uses only lepton flavour-sign combinations to define a control region is investigated as an alternative to the background estimation presented here.

8.1.2 Interchanging Lepton Flavour

The fact that $t\bar{t}$ trilepton events have different flavour-sign lepton combinations compared to $\tilde{\chi}\tilde{\chi}$ SUSY signal events can be used to estimate the $t\bar{t}$ background to the exclusive trilepton signal. In this section, the control region is defined as trilepton events with lepton flavour-sign combinations 1 to 4, and the signal region is defined as trilepton events with lepton flavour-sign combinations 5 to 12. One method to extrapolate $t\bar{t}$ events from the control region to the signal region is to interchange lepton flavour in lepton combinations in the control region, to obtain combinations that are compatible with the signal region. To do so, it is necessary to match the combinations in each region by their third lepton from the b-quark decay. Since combinations 5-8 have two possible candidates for the b-quark lepton, they are each separated into two distinct combinations (labelled a and b in the following) to take this into account. In Figure 8.6, the method for comparing control region combinations to their signal region counterparts is shown, where each control region combination may be used to estimate three signal region combinations by replacing electrons with muons or vice versa. For example, with combination 1 $e^-\mu^+\mu^+$, where the b-quark lepton must be one of the μ^+ (because the e^- is needed to form the OS pair), the act of replacing the e^- with a μ^-, or the μ^+ with a e^+, or both, results in combinations 12, 6a or 8b respectively.

When comparing two combinations with the same flavour lepton from the b-quark decay, the dominating factor in their relative rates will come from the reconstruction of the two OS leptons. Consider two combinations, where one has $e^+\mu^-$ as its OS pair and another has e^+e^-, and both have the same flavour-sign third lepton from b-quark decay. Their relative rates will depend on how well the μ^- can be reconstructed in comparison to the e^-. It was seen in Section 4.2 that

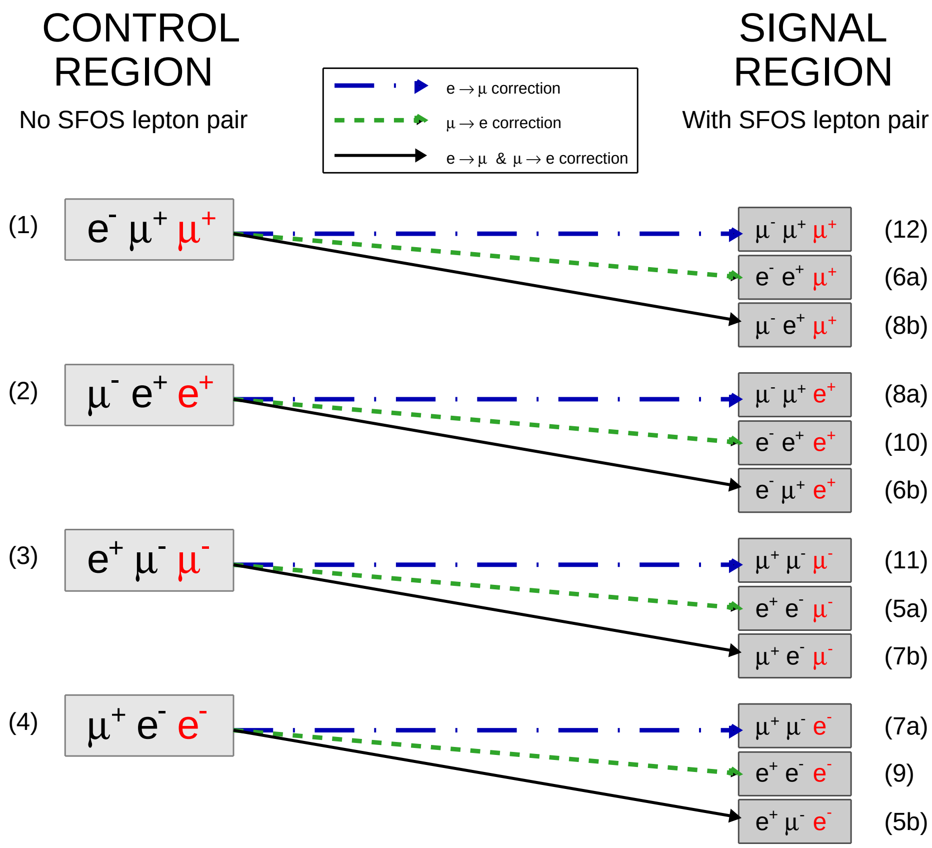

Figure 8.6: Method for extrapolating $t\bar{t}$ background events from the control region to the signal region using lepton flavour-sign combinations and corrections for replacing one lepton flavour with another. Leptons from b-quark decay are shown in red and leptons from $W^{\pm}$ decay are shown in black. See text for lepton replacement correction details.

muon reconstruction efficiency is higher than the electron reconstruction efficiency. Thus, the combination with $e^+\mu^-$ is expected to have a higher rate in comparison to e^+e^-, defined by the ratio of muon to electron reconstruction efficiency. It was also observed in Section 4.2 that the fake rate for muons is lower than for electrons. The ratio between muon and electron fake rates will also affect the relative rates of the two combinations $e^+\mu^-$ and e^+e^-, driving the rate of the latter up in relation to the former. If the differences in the reconstruction of electrons and muons are well understood and can be accurately measured, then the relative rate between the two combinations can also be known. Thus, the first combination with $e^+\mu^-$ as its OS pair may be used to estimate the combination with e^+e^- as its OS pair, by replacing the μ^- with a e^- and correcting for differences in electron/muon reconstruction.

By matching lepton flavour-sign combinations in trilepton events using the b-quark lepton, the only difference between the control and signal region combinations is now the lepton flavours from the W^+ or W^- decay. Correction factors can be implemented when replacing electrons with muons (or vice versa), which will have to be estimated from efficiencies and fake rates of leptons from heavy decays such as the W boson. Clearly, the key to extrapolating background levels from the control region to the signal region will be the understanding of lepton efficiencies and fake rates in $t\bar{t}$ events.

Calculation of Correction Factors

The correction factors that are used to take into account the replacement of a muon with an electron or vice versa include lepton efficiency and fake rate effects. The correction to replace an electron with a muon ($e \to \mu$) is defined as

$$C_{e\to\mu} = P_e^f \left[\frac{f_\mu}{f_e}\right] + (1 - P_e^f)\left[\frac{\varepsilon_\mu}{\varepsilon_e}\right], \tag{8.2}$$

and the correction to replace a muon with an electron ($\mu \to e$) is defined as

$$C_{\mu\to e} = P_\mu^f \left[\frac{f_e}{f_\mu}\right] + (1 - P_\mu^f)\left[\frac{\varepsilon_e}{\varepsilon_\mu}\right], \tag{8.3}$$

where, taking $X = e, \mu$, P_X^f is the probability of the lepton being fake and is calculated using the number of fake leptons divided by the total number of leptons; ε_X is the lepton efficiency; and f_X is the lepton fake rate as defined in Equation 4.1 and Equation 4.2, respectively. The two parts of each correction are designed to evaluate whether the lepton in question is a real lepton or has been faked by a jet, and the efficiency or fake rate ratios respectively are applied for each case.

In Section 4.2, it was seen that lepton efficiencies and fake rates are dependent on the p_T and η of the lepton, therefore, it would seem appropriate to take these dependencies into account when estimating backgrounds. Hence, the lepton efficiencies and fake rates are split into p_T and η bins. Due to small sample statistics, this is done in one-dimensional bins for p_T and η separately, and then, for a particular two dimensional bin, the product of the two factors is taken. This is then normalised to the corresponding "global" (integrated over p_T and η) factor, for example by taking the ratio $[\varepsilon_e(p_T) \times \varepsilon_e(\eta)]$ / [global ε_e] for the efficiency $\varepsilon_e(p_T, \eta)$.

Using p_T and η dependent efficiencies and fake rates, the correction factors for lepton replacement, seen in Equation 8.2 and Equation 8.3, can be defined to take into account the p_T and η of the lepton being replaced. In the following, p_T and η dependent lepton replacement corrections will be referred to as "topological" corrections, $C^{TOPO}_{e\rightarrow\mu}$ and $C^{TOPO}_{\mu\rightarrow e}$. Lepton replacement corrections using global lepton efficiencies and fake rates will be referred to as "flat" corrections, $C^{FLAT}_{e\rightarrow\mu}$ and $C^{FLAT}_{\mu\rightarrow e}$.

When ambiguity exists in the choice of the lepton from the b-quark decay, as for combination 1, the lowest p_T candidate is chosen, a choice that is correct in ~87 % of the cases. Further methods involving lepton impact parameter, isolation or mixtures of the three have been tried but all proved to be less effective in identifying the lepton from b-quark decay than using the p_T alone. The error associated with the misidentification of the lepton from the b-quark decay has not been included in the errors presented here, and its use could in future provide some improvements of the results obtained here.

The lepton efficiencies and fake rates used in the correction factors have been calculated from the generator level information in a subset of ~ 100,000 $t\bar{t}$ events. Electron and muon efficiencies and fake rates as seen in Section 4.2 were found and applied to the rest of the $t\bar{t}$ sample.

Estimation using Generator Level Lepton Performance

Global and topologically dependent (in η and p_T) efficiencies and fake rates are calculated using ~100,000 events in the $t\bar{t}$ sample, according to the prescriptions described in Section 4.2. These efficiencies and fake rates are then used to calculate the flat and topological lepton corrections, $C^{FLAT}_{e\rightarrow\mu}$, $C^{FLAT}_{\mu\rightarrow e}$, $C^{TOPO}_{e\rightarrow\mu}$ and $C^{TOPO}_{\mu\rightarrow e}$. These lepton corrections so obtained are finally used in a non-overlapping sample of ~500,000 $t\bar{t}$ events to extrapolate background levels from the control region to the signal region. Results for the $t\bar{t}$ background estimation to the exclusive trilepton

Combination	True	Estimated	
		Flat	Topo
5	5.0±2.2	5.9±2.4	6.1±2.5
6	1.0±1.0	6.0±2.4	4.5±2.0
7	7.0±2.6	6.0±2.5	5.7±2.4
8	2.0±1.4	6.1±2.5	5.1±2.1
9	3.0±1.7	3.0±1.7	3.2±1.9
10	1.0±1.0	4.9±2.2	4.2±2.0
11	0.0±0.0	3.0±1.8	2.8±1.6
12	0.0±0.0	1.0±1.0	0.8±0.8
TOTAL	19.0±4.4	35.9±10.4	32.5±9.6

Table 8.2: The estimated $t\bar{t}$ background in the signal region using flat lepton corrections and topological lepton corrections found from generator level information in the $t\bar{t}$ MC sample. Numbers quoted are the number of events in the sample used for estimation and are not scaled in any way.

signal (after all the selection cuts have been applied) can be seen in Table 8.2 and Figure 8.7. In these, flat and topological lepton corrections have been made separately. In this estimation, the positive and negative event weights associated with the $t\bar{t}$ MC have been ignored for simplicity. The method generally appears to overestimate the $t\bar{t}$ background, particularly when flat lepton corrections are used. Trilepton combinations 5, 7, 9 and 12 are well estimated, however, the other combinations in the signal region are overestimated. The lack of statistics in the signal region must be noted at this point, which could be accountable to some extent for the less than favourable results for this background estimation method. Using flat lepton corrections gives an overall estimation for the $t\bar{t}$ background that is too high compared to the true value, even when errors are considered, suggesting the use of flat lepton performance is too simple to describe the lepton replacement. Using topologically dependent lepton corrections to estimate the $t\bar{t}$ background gives, within errors, a result that has a slightly better agreement with the true value, but still not fully satisfactory.

To assess how robust this background estimation is to contamination in the control region, varying levels of signal and other SM backgrounds have been added to the original $t\bar{t}$ events. The results of the $t\bar{t}$ background estimation using lepton corrections from generator level information is shown in Figure 8.8, where the effect of the presence of one to three times the levels of $\tilde{\chi}\tilde{\chi}$ signal and other surviving SM backgrounds has been taken into account for 10 fb^{-1} of data. It is seen that the presence of signal and other SM backgrounds worsens the estimation of the $t\bar{t}$ background, and can change the original estimation by over 20%.

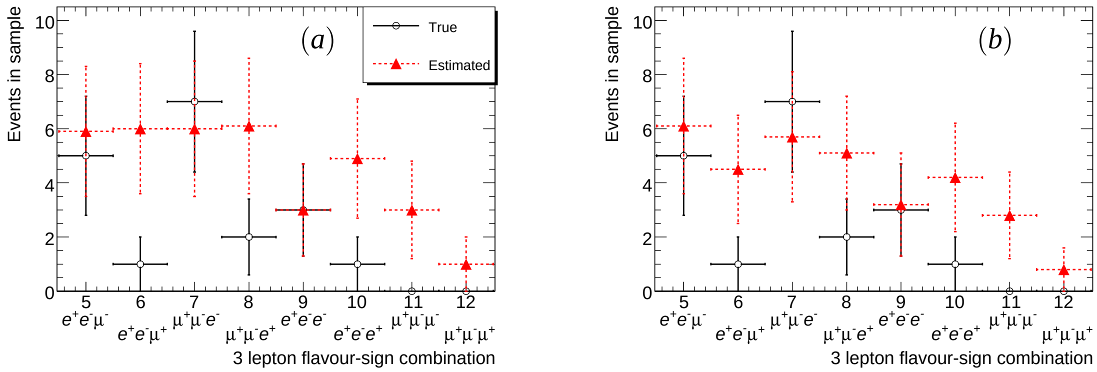

Figure 8.7: The estimated $t\bar{t}$ background in the signal region using flat lepton corrections (a) and topological lepton corrections (b) found from generator level information in the $t\bar{t}$ MC sample. The true $t\bar{t}$ background levels are shown in open black circles while the estimated levels are in solid red triangles.

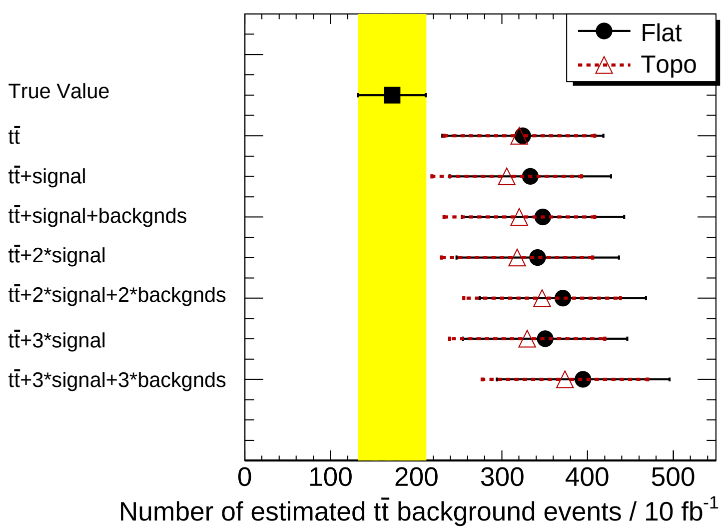

Figure 8.8: Estimation of the $t\bar{t}$ background to the exclusive trilepton signal using lepton corrections from generator level information in the $t\bar{t}$ MC sample, including contaminations from the SUSY signal and other SM backgrounds. Results using flat corrections are shown in solid black circles and topological corrections in open red triangles. All results have been normalised to 10 fb^{-1} of data.

This second method appears to be less successful than the first method presented in Section 8.1.1 for estimating the $t\bar{t}$ background to the exclusive trilepton signal. Possible causes of the worse performance for this method could lie in the definition of the lepton replacement correction factors $C_{e\to\mu}$ and $C_{\mu\to e}$, or in the errors associated with the identification of the lepton from the b-quark decay. Furthermore, lepton fake rates in trilepton events may not be well described by the lepton fake rate definitions implemented here. Finally, the small number of $t\bar{t}$ events for each of the four lepton flavour-sign combinations in the control region are unlikely to be enough to robustly test this background estimation method.

8.2 Investigation for the Inclusive Trilepton Analysis

A satisfactory method has been found for estimating the $t\bar{t}$ background to the exclusive trilepton signal, as presented in Section 8.1, but it is important that a method also be found for the inclusive trilepton signal. In Section 6.1, it was seen that the only surviving background to an inclusive trilepton signal is a small number of $t\bar{t}$ events. Due to the simplicity of the inclusive trilepton event selection, where only three leptons and a high-p_T jet are demanded to be present, a method that reverses two of the requirements in the selection, as presented in Section 8.1.1, is not suitable here. Furthermore, a method that interchanges lepton flavour, as presented in Section 8.1.2, is also unsuitable as the inclusive trilepton analysis does not incorporate a SFOS lepton pair selection. If such a SFOS lepton pair requirement was to be included in the inclusive trilepton selection, an unacceptable contamination in the control region from SUSY events is foreseen.

In attempts to estimate the $t\bar{t}$ background to SUSY dilepton events, the so-called "top-box" method was used [31], which reconstructed the t-quark and $\bar{t}$-quark masses using the dilepton $t\bar{t}$ event kinematics. Since there are two escaping neutrinos, an analytical solution must be used here to find the momentum of the neutrinos [56].

The kinematics of the three leading jets, the two OS leptons, the $\not{E}_T$ of the event and the nominal W boson and t-quark masses are used to form two polynomial equations with the two neutrino momenta as unknowns. The two polynomial equations are reduced to one quartic equation, for which solutions may be found for the neutrino momenta. The number of real solutions found per event may be used to select $t\bar{t}$ trilepton events from SUSY trilepton events. Top pair production events should display a higher number of solutions than SUSY events, since they are

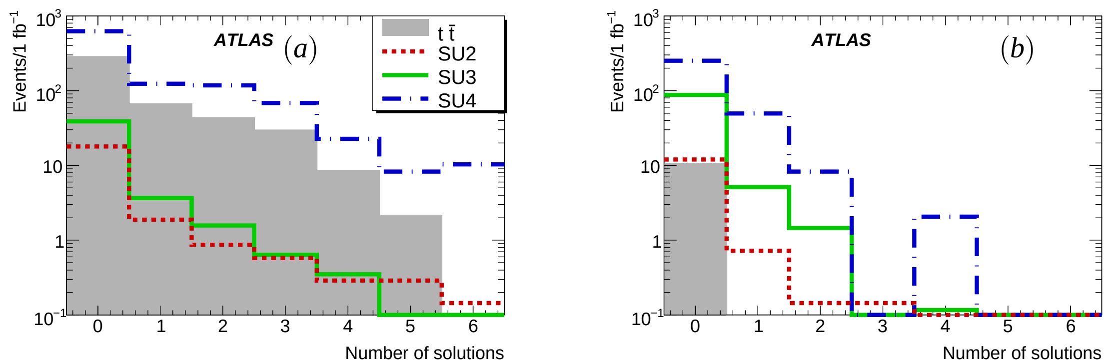

Figure 8.9: The number of solutions for the two neutrino momenta obtained using $t\bar{t}$ dilepton equations, for SUSY and $t\bar{t}$ trilepton events with $p_T^{jet1} < 200$ GeV, *(a)*, and with $p_T^{jet1} > 200$ GeV, *(b)*. All distributions are normalised to 1 fb^{-1} of data.

the event topology the method aims to reconstruct.

The number of analytical solutions obtained using $t\bar{t}$ dilepton equations for the SUSY benchmark scenarios and $t\bar{t}$ are shown in Figure 8.9 for events with p_T^{jet1} <200 GeV (control region) and with $p_T^{jet1} > 200$ GeV (signal region). In dilepton events [31], the SUSY events were seen to dominate in the low multiplicity solution bins, an effect which is only true for the SU4 trilepton events seen here. Any control region created using a reversal of the p_T^{jet1} requirement and demanding a high number of solutions would result in a large contamination from a trilepton signal at the SU4 point. More importantly, by comparing the $t\bar{t}$ distribution in Figure 8.9(a) to that in Figure 8.9(b), it is clear that the shapes of the distributions are very different. The large tails seen in the $t\bar{t}$ distribution of events that failed the p_T^{jet1} requirement are not observed in the distribution of events that passed the p_T^{jet1} requirement, suggesting the $t\bar{t}$ events that survive the inclusive trilepton selection have a genuine similarity to the SUSY signal. The lack of events in high multiplicity solution bins for $t\bar{t}$ in Figure 8.9(b) could also be due to a lack of statistics in the $t\bar{t}$ MC sample, where only 15 positively weighted and 5 negatively weighted events survive the event selection. In conclusion, any selection made on the number of solutions in an event will result in a non-consistent ratio of events in the two distributions.

Unfortunately, a successful method for the estimation of the $t\bar{t}$ background to the inclusive trilepton SUSY signal has yet to be found. The sheer simplicity of the selection has resulted in fewer options for background estimation than for more complex selections such as the exclusive trilepton signal. If a combination of a high-p_T jet and a large $\not{E}_T$ requirement are used to select

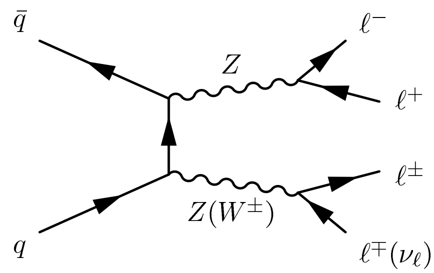

Figure 8.10: Fully leptonic ZW events may be modelled using $ZZ \rightarrow \ell^+\ell^-\ell^+\ell^-$ events and replacing a lepton with a neutrino.

SUSY trilepton events, as investigated in Section 7.4, then a method that reverses both selections to define a control region may be possible, however, contamination from the other surviving SM backgrounds will certainly be an issue.

8.3 Ideas to Estimate the ZW Background

Although $t\bar{t}$ is clearly the most dangerous background for a SUSY trilepton analysis, non-negligible levels of ZW also remain after the event selection, particularly for the exclusive analysis. A well established method that uses ZZ events to estimate ZW events already exists within ATLAS that could be adopted here estimate the ZW background from data. This method could not be implemented by the time of writing, due to limited MC sample statistics, and therefore only a broad overview of the method is given here.

In Figure 8.10, the Feynman diagram is shown for both ZZ and ZW fully leptonic final states ($ZW \rightarrow \ell^+\ell^-\ell\nu$ and $ZZ \rightarrow \ell^+\ell^-\ell^+\ell^-$), where it is clear that the only difference in final states is the presence of either a fourth charged lepton or a neutrino.

With enough statistics collected (1 fb^{-1} corresponds to ~15 reconstructed four lepton events from ZZ), the $ZZ \rightarrow \ell^+\ell^-\ell^+\ell^-$ events could be selected from the ATLAS data by requesting four leptons, where the two SFOS lepton pairs both have invariant masses consistent with the nominal Z boson mass. The replacement of one of the four leptons in the $ZZ \rightarrow \ell^+\ell^-\ell^+\ell^-$ final state with a neutrino (which would be added to the $\not{E}_T$ of the event) results in the same final state as a fully leptonic ZW decay. Then, correcting for differences in $\sigma(pp \rightarrow ZZ)$ and $\sigma(pp \rightarrow ZW)$, differences in m_Z and m_W, in addition to any possible differences in angular distributions, $ZW \rightarrow \ell^+\ell^-\ell\nu$ events could be fully modelled. Different cross-section corrections would need to be applied depending on whether a ZW^+ or ZW^- event is being modelled, as $\sigma(pp \to ZW^+) > \sigma(pp \to ZW^-)$. Four ZW events could be modelled for every ZZ event found, since there are four leptons that could each be replaced by a neutrino. The inclusive or exclusive trilepton selection could then be applied to estimate how many ZW events would contribute to a trilepton signal. Unfortunately, no four lepton events in the ZZ MC sample used in this analysis survive either the exclusive or inclusive trilepton event selection, making a background estimation impossible at this stage. As discussed in Chapter 3 the ZZ MC sample used in this analysis is unlikely to accurately reconstruct the tails in distributions like p_T^{jet1}. In the ATLAS data, it is fully expected that there will be four lepton ZZ events passing the trilepton selections with which a data driven background estimation can be made. It is intended that in the near future a proof of principle of this method will be verified using fast simulations, which can provide much larger statistics on a reasonable time scale.

8.4 Summary

Methods have been presented in this chapter for possible data driven background estimations of both the $t\bar{t}$ and ZW backgrounds to a trilepton SUSY signal. Since $t\bar{t}$ is a dominant background for both the inclusive and exclusive trilepton analyses, the onus has been on developing data driven methods to estimate $t\bar{t}$, however, an idea to use ZZ events to estimate the ZW background to a trilepton signal has been also been discussed.

A data driven background estimation method for the inclusive trilepton signal has been investigated, which uses the number of analytical solutions for the two neutrino momenta obtained using $t\bar{t}$ dilepton equations. Unfortunately, it is found to be unsuitable due to striking differences in the shape of the number of solutions distribution for $t\bar{t}$ events that pass or fail the p_T^{jet1} requirement. It appears that the simplicity of the inclusive trilepton selection prohibits a straightforward definition of a background control sample, however, future efforts in this area will be directed towards finding an alternative solution.

A method to estimate the $t\bar{t}$ background to the exclusive trilepton analysis has been examined that uses both lepton flavour-sign combinations and lepton track isolation to define the signal and control regions and normalise between them. This data driven approach is found to estimate the $t\bar{t}$ background accurately and reliably, even with contamination in the control region.

A second method exploiting the lepton flavour-sign combinations in $t\bar{t}$ trilepton events has also been used to estimate the $t\bar{t}$ background to the exclusive trilepton signal. Extrapolation from the control region to the signal region was performed using flat and topological corrections calculated from lepton performance obtained using generator level information from the $t\bar{t}$ sample. Although flat lepton corrections are found to overestimate the $t\bar{t}$ background, topological corrections result in a background estimation that is compatible with the true value, within errors. Regrettably, this method of $t\bar{t}$ background estimation appears to be rather sensitive to the presence of any SUSY signal or other SM background events, which can worsen the measurement and give incompatible results with the true value. This method may be improved in a number of ways, the first being an increase in statistics to obtain a reasonable number of events for each trilepton combination in the signal region. ATLFASTCorrectors [57] could be used as a fast simulation of the ATLAS detector that includes parameterisations of lepton efficiencies and fake rates (found from full simulation), to produce the large statistics required. Secondly, a very careful study of how lepton efficiencies and fake rates may be obtained from ATLAS data and applied to this method is vital.

With the first proton collisions at the LHC expected in 2009, the search for evidence of SUSY (or any other new physics) will soon begin. Using data driven methods for background estimation like the ones discussed in this chapter will minimise the reliance on MC simulations, which is vital when exploring physics at a new energy scale.

Chapter 9

Conclusions

The failure of the Standard Model to successfully describe particles and their interactions at high energies suggests new physics could be found at the TeV scale. By proposing the existence of new massive particles at high energies, Supersymmetry provides a natural and elegant extension to the Standard Model. The ATLAS experiment at the Large Hadron Collider is dedicated to the search for the Higgs boson and new physics at high energies. The ATLAS detector incorporates multiple precision subsystems with coverage over a large pseudorapidity range to maximise the discovery potential of any new physics produced in the high energy pp collisions.

The production of SUSY particles at the LHC and their subsequent decays to trilepton final states has been studied in this thesis. In Chapter 5, strategies to search for SUSY in the inclusive and exclusive trilepton channels with the ATLAS detector were developed for a range of mSUGRA scenarios. The strategies for both trilepton channels appear to be robust with respect to the variety of systematic studies performed in Chapter 7. Additionally, the combination of basic single electron and muon triggers should guarantee high trigger efficiencies for trilepton final states.

The inclusive trilepton SUSY analysis requires the presence of three leptons and one high-p_T jet in the final state and yields an early SUSY discovery channel for ATLAS. In absence of systematic effects not considered here, the inclusive trilepton selection achieves a 5σ discovery with an accumulated statistics of between a few hundred pb^{-1} and a few fb^{-1}, depending on the considered benchmark scenario. Furthermore, the inclusive trilepton strategy has been shown to be suitable for physics searches with the very first, lower centre of mass energy data from ATLAS.

The exclusive trilepton SUSY analysis has been performed for the focus point region of mSUGRA parameter space, where direct gaugino production is particularly important. In contrast to the inclusive channel, direct gaugino production is associated with little hadronic activity, and so a strategy was developed to include stringent lepton track isolation and upper limits on both lepton track impact parameter and leading jet momentum. In addition, the exclusive trilepton selection requires a small amount of missing transverse energy and vetoes events with same flavour opposite sign lepton pairs with invariant mass consistent with the Z boson mass. In the absence of systematic effects, a 5σ discovery can be achieved for the exclusive trilepton channel with an integrated luminosity of few tens of fb^{-1}.

Methods for data-driven background estimations for the inclusive and exclusive trilepton analyses were investigated in Chapter 8. Two possible methods were presented that use lepton flavour-sign combinations, either alone, or in addition to lepton track isolation to estimate the $t\bar{t}$ background to the exclusive trilepton signal. A method relying on the kinematics of $t\bar{t}$ events to estimate the $t\bar{t}$ background to the inclusive trilepton signal was also explored and an idea to estimate the ZW background for both channels was discussed.

A possible extension to the work presented in this thesis may be to include hadronically decaying taus as well as electrons and muons in the definition of a trilepton signal. The development of further data-driven methods to estimate $t\bar{t}$ background levels will be essential, particularly for the inclusive trilepton analysis. The importance of trilepton channels in the search for SUSY has been firmly established in this thesis and the analysis strategies developed here could yield early SUSY discovery signals at the LHC.

Appendix A

Data Samples and Analysis Procedure

A.1 Data Samples for E_{CM}= 14 TeV

The following ATLAS samples were used for the E_{CM}= 14 TeV trilepton analysis described in this thesis:

```
trig1_misal1_csc11.005402.SU2_jimmy_susy.merge.AOD.v12000605
trig1_misal1_csc11.005403.SU3_jimmy_susy.merge.AOD.v12000605
trig1_misal1_csc11.006400.SU4_jimmy_susy.merge.AOD.v12000605
trig1_misal1_mc12.005200.T1_McAtNlo_Jimmy.recon.AOD.v12000604
trig1_misal1_mc12.005178.Zb_acer_pythia.recon.AOD.v12000605
trig1_misal1_csc11.005985.WW_Herwig.merge.AOD.v12000605
trig1_misal1_csc11.005986.ZZ_Herwig.merge.AOD.v12000605
trig1_misal1_csc11.005987.WZ_Herwig.merge.AOD.v12000605
trig1_misal1_csc11.005900.PythiaZPhoton25.merge.AOD.v12000604
```

A list of the Monte Carlo generators used to produce each sample is given in Table 3.9. All data samples used are official centrally produced samples that fully simulate the ATLAS detector using GEANT4 [43] and analysed with the ATLAS analysis framework, Athena (release 12.0.6).

A.2 Data Samples for E_{CM}= 10 TeV

The following ATLAS samples were used for the E_{CM}= 10 TeV trilepton analysis described in this thesis:

`mc08.105403.SU3_jimmy_susy.recon.AOD.e352_s462_r541`

`mc08.106400.SU4_jimmy_susy.recon.AOD.e352_s462_r541`

`mc08.105200.T1_McAtNlo_Jimmy.recon.AOD.e357_s462_r541`

The Monte Carlo generators used to produce each sample are the same as those used for the E_{CM}= 14 TeV samples and are given in Table 3.9. All data samples used are official centrally produced samples that fully simulate the ATLAS detector using GEANT4 [43] and analysed with the ATLAS analysis framework, Athena (release 14.2.10).

A.3 Analysis Procedure

Full simulation data is available in AOD (Analysis Object Data) format, where particles are loosely reconstructed and recorded in containers. In principle, a particle may be loosely reconstructed by more than one algorithm and be recorded in multiple containers. This overlap must be removed to avoid double counting of objects. The official AODs, stored at Tier-2 Grid sites worldwide, are processed within the Athena framework to produce private ntuples using ATLAS Distributed Analysis Tools [58]. The resulting custom-made user ntuples are then stored on Tier-2 Grid sites as a user dataset and are usually transferred to a local cluster for further analysis.

Appendix B

Formulae for Mass Edges

The formulae used to calculate the expected mass edges for the distributions shown in Section 6.3 are given below [50], [51]. The assumed mass hierarchy is $m_{\tilde{\chi}_1^0} < m_{\tilde{\ell}_R} < m_{\tilde{\chi}_2^0} < m_{\tilde{q}_L}$, like in the case of the SU3 benchmark point. Where $m_{\tilde{q}_L}$ is required, the average of $m_{\tilde{u}_L}$, $m_{\tilde{d}_L}$, $m_{\tilde{c}_L}$, and $m_{\tilde{s}_L}$ is used.

The SFOS dilepton mass edge is given by:

$$m_{ll}^{edge} = \sqrt{\frac{(m^2_{\tilde{\chi}_2^0} - m^2_{\tilde{\ell}_R})(m^2_{\tilde{\ell}_R} - m^2_{\tilde{\chi}_1^0})}{m^2_{\tilde{\ell}_R}}}. \tag{B.1}$$

The dilepton+jet mass edge and threshold positions are obtained from:

$$m_{llq}^{edge} = \max \{ \sqrt{A},\ \sqrt{B},\ \sqrt{C} \} \tag{B.2}$$

where:

$$A = \frac{(m^2_{\tilde{q}_L} - m^2_{\tilde{\chi}^0_2})\ (m^2_{\tilde{\chi}^0_2} - m^2_{\tilde{\chi}^0_1})}{m^2_{\tilde{\chi}^0_2}}\,; \tag{B.2a}$$

$$B = \frac{(m^2_{\tilde{q}_L} - m^2_{\tilde{\ell}_R})\ (m^2_{\tilde{\ell}_R} - m^2_{\tilde{\chi}^0_1})}{m^2_{\tilde{\ell}_R}}\,; \tag{B.2b}$$

$$C = \frac{(m^2_{\tilde{q}_L} m^2_{\tilde{\ell}_R} - m^2_{\tilde{\chi}^0_2} m^2_{\tilde{\chi}^0_1})\ (m^2_{\tilde{\chi}^0_2} - m^2_{\tilde{\ell}_R})}{m^2_{\tilde{\chi}^0_2}\ m^2_{\tilde{\ell}_L}}\,. \tag{B.2c}$$

and:

$$m^{thr}_{llq} = \sqrt{\frac{X - Y}{Z}} \tag{B.3}$$

where:

$$X = 2\, m^2_{\tilde{\ell}_R}\ (m^2_{\tilde{q}_L} - m^2_{\tilde{\chi}^0_2})\ (m^2_{\tilde{\chi}^0_2} - m^2_{\tilde{\chi}^0_1}) + (m^2_{\tilde{q}_L} + m^2_{\tilde{\chi}^0_2})\ (m^2_{\tilde{\chi}^0_2} - m^2_{\tilde{\ell}_R})\ (m^2_{\tilde{\ell}_R} - m^2_{\tilde{\chi}^0_1})\,; \tag{B.3a}$$

$$Y = (m^2_{\tilde{q}_L} - m^2_{\tilde{\chi}^0_2})\sqrt{(m^2_{\tilde{\chi}^0_2} + m^2_{\tilde{\ell}_R})^2\ (m^2_{\tilde{\ell}_R} + m^2_{\tilde{\chi}^0_1})^2 - 16\, m^2_{\tilde{\chi}^0_2}\ (m^2_{\tilde{\ell}_R})^2\ m^2_{\tilde{\chi}^0_1}}\,; \tag{B.3b}$$

$$Z = 4\, m^2_{\tilde{\ell}_R} m^2_{\tilde{\chi}^0_2}\,. \tag{B.3c}$$

Furthermore, the “high” and “low” lepton+jet mass edges are given by:

$$m^{high}_{lq} = \max\left\{ \sqrt{\frac{(m^2_{\tilde{q}_L} - m^2_{\tilde{\chi}^0_2})\ (m^2_{\tilde{\chi}^0_2} - m^2_{\tilde{\ell}_R})}{m^2_{\tilde{\chi}^0_2}}},\ \sqrt{\frac{(m^2_{\tilde{q}_L} - m^2_{\tilde{\chi}^0_2})(m^2_{\tilde{\ell}_R} - m^2_{\tilde{\chi}^0_1})}{m^2_{\tilde{\ell}_R}}} \right\}, \tag{B.4}$$

and:

$$m^{low}_{lq} = \min\left\{ \sqrt{\frac{(m^2_{\tilde{q}_L} - m^2_{\tilde{\chi}^0_2})\ (m^2_{\tilde{\chi}^0_2} - m^2_{\tilde{\ell}_R})}{m^2_{\tilde{\chi}^0_2}}},\ \sqrt{\frac{(m^2_{\tilde{q}_L} - m^2_{\tilde{\chi}^0_2})\ (m^2_{\tilde{\ell}_R} - m^2_{\tilde{\chi}^0_1})}{2\, m^2_{\tilde{\ell}_R} - m^2_{\tilde{\chi}^0_1}}} \right\}. \tag{B.5}$$

Bibliography

[1] B. R. Martin and G. Shaw, *Particle Physics*. John Wiley and Sons, second ed., 1997.

[2] F. Halzen and A. Martin, *Quarks and Leptons: An Introductory Course in Modern Particle Physics*. John Wiley and Sons, 1984.

[3] L. H. Ryder, *Quantum Field Theory*. Cambridge University Press, second ed., 1996.

[4] C. Amsler *et. al.*, “Review of Particle Physics”, *Phys. Lett.* **B667** (2008) 1.

[5] Y. Fukada *et. al.*, “Evidence for oscillation of atmospheric neutrinos”, *Phys. Rev. Lett.* **81** (1998) 1562–1567.

[6] The SNO Collaboration, “Independent Measurement of the Total Active ^{8}B Solar Neutrino Flux Using an Array of ^{3}He Proportional Counters at the Sudbury Neutrino Observatory”, *Phys. Rev. Lett.* **101** (2008).

[7] The Super-Kamiokande Collaboration, “Solar neutrino measurements in Super-Kamiokande-II”, *Phys. Rev.* **D78** (2008).

[8] S. L. Glashow, “The Status of the Electroweak Sector of the Standard Model”, *Nucl. Phys.* **22** (1961) 579.

[9] A. Salam and J. C. Ward, “Electromagnetic and Weak Interactions”, *Phys. Lett* **13** (1964) 168.

[10] S. Weinberg, “A Model of Leptons”, *Phys. Rev. Lett* **19** (1967) 1264.

[11] N. Cabibbo, “Unitary Symmetry and Leptonic Decays”, *Phys. Rev. Lett.* **10** (1963) 531.

[12] P. W. Higgs, “Broken symmetries and the masses of gauge bosons”, *Phys. Rev. Lett.* **13** (1964) 508–509.

[13] C. Lee, B. W. Quigg, and H. Thacker, “Strength of weak interactions at very high energies and the higgs boson mass”, *Phys. Rev. Lett.* **38** (1977) 883.

[14] ALEPH, DELPHI, L3 and OPAL Collaborations, “Search for the Standard Model Higgs Boson at LEP”, *Phys. Lett.* **B565** (2003) 61.

[15] The LEP Collaborations, "A Combination of Preliminary Electroweak Measurements and Constraints on the Standard Model." arXiv:hep-ex/0511027v2, 2005.

[16] The Tevatron New-Phenomena and Higgs Working Group, "Combined CDF and DØ Upper Limits on Standard Model Higgs Boson Production at High Mass (155-200 GeV/c^2) with 3 fb^{-1} of data." arXiv:hep-ex/0808.0534v1, 2008.

[17] J. Wess and B. Zumino, "A Lagrangian Model Invariant Under Supergauge Transformations", *Phys. Lett.* **B49** (1974) 52.

[18] S. P. Martin, "A Supersymmetry Primer." arXiv:hep-ph/9709356v4, 1997.

[19] The Super-Kamiokande Collaboration, "Search for Proton Decay via $p \to e^+\pi^0$ in a Large Water Cherenkov Detector", *Phys. Rev. Lett.* **81** (1998) 3319–3323.

[20] H. P. Nilles, "Dynamically Broken Supergravity and the Hierarchy Problem", *Phys. Lett.* **B115** (1982) 193.

[21] G. F. Giudice and R. Rattazzi, "Theories with Gauge-Mediated Supersymmetry Breaking", *Phys. Rept* **322** (1999) 419–499.

[22] L. Randall and R. Sundrum, "Out Of This World Supersymmetry Breaking", *Nucl. Phys.* **B557** (1999) 79–118.

[23] E. Komatsu *et. al.*, "Five-Year Wilkinson Microwave Anisotropy Probe (WMAP) Observations: Cosmological Interpretation." arXiv:astro-ph/0803.0547v2, 2008.

[24] B. C. Allanach *et. al.*, "The Snowmass Points and Slopes: Benchmarks for SUSY Searches", *Eur. Phys. J* **C25** (2002) 113–123.

[25] J. Ellis, K. A. Olive, Y. Santoso, and V. C. Spanos, "Supersymmetric Dark Matter in Light of WMAP", *Phys. Lett.* **B565** (2003) 176–182.

[26] The ATLAS Experiment at CERN, http://atlas.ch.

[27] The ATLAS Fact Sheet, http://atlas.ch.

[28] A. D. Martin, R. G. Roberts, W. J. Stirling, and R. S. Thorne, "Uncertainties of predictions from parton distributions. II: Theoretical errors", *Eur. Phys. J* **C35** (2004) 325–348.

[29] The ATLAS Collaboration, "The ATLAS Experiment at the CERN Large Hadron Collider", *JINST* **3** (2008) S08003.

[30] W.Beenakker, R.Hoepker, and M.Spira, "PROSPINO: A Program for the Production of Supersymmetric Particles in Next-to-leading Order QCD." arXiv:hep-ph/9611232v1, 1996.

[31] The ATLAS Collaboration, "Expected Performance of the ATLAS Experiment, Detector, Trigger and Physics." CERN-OPEN-2008-020, Geneva, 2008.

[32] H. Baer, F. Paige, S. Protopopescu, and X. Tata, "Simulating Supersymmetry with ISAJET 7.0/ ISASUSY 1.0." arXiv:hep-ph/9305342v1, 1993.

[33] The CDF Collaboration, “Search for Supersymmetry in $p\bar{p}$ Ccollisions at $\sqrt{s}$ =1.96 TeV Using the Trilepton Signature for Chargino-Neutralino Production”, *Phys. Rev. Lett.* **101** (2008) 251801.

[34] The DØ Collaboration, “Search for associated production of charginos and neutralinos in the trilepton final state using 2.3 fb^{-1} of data.” `arXiv:hep-ex/0901.0646v1`, 2009.

[35] B. P. Kersevan and I. Hinchliffe, “A Consistent Prescription for the Production Involving Massive Quarks in Hadron Collisions”, *JHEP* **0609** (2006) 033.

[36] T. Sjostrand, S. Mrenna, and P. Skands, “PYTHIA 6.4 Physics and Manual”, *JHEP* **0605** (2006) 026.

[37] G. Corcella *et. al.*, “HERWIG 6.5: and event generator for Hadron Emission Reactions With Interfering Gluons (including supersymmetric processes)”, *JHEP* **0101** (2001) 010.

[38] S. Moretti, K. Odagiri, P. Richardson, M. H. Seymour, and B. R. Webber, “Implementation of supersymmetric processes in the HERWIG event generator”, *JHEP* **0204** (2002) 028.

[39] J. M. Butterworth, J. R. Forshaw, and M. H. Seymour, “Multiparton Interactions in Photoproduction at HERA”, *Z. Phys* **C72** (1996) 637–464.

[40] S. Frixione and B. R. Webber, “Matching NLO QCD computations and parton shower simulations”, *JHEP* **0206** (2002) 029.

[41] S. Frixione, P. Nason, and B. R. Webber, “Matching NLO QCD and parton showers in heavy flavour production”, *JHEP* **0308** (2003) 007.

[42] B. P. Kersevan and E. Richter-Was, “The Monte Carlo Event Generator AcerMC 2.0 with Interfaces to PYTHIA 6.2 and HERWIG 6.5.” `arXiv:hep-ph/0405247v1`, 2004.

[43] S.Agostinelli *et. al.*, “Geant4 - a simulation toolkit”, *Nucl. Instrum. and Meth.* **A506** (2003) 250–303.

[44] The ATLAS Collaboration, “ATLAS computing: Technical Design Report.” ATLAS-TDR-017, CERN-LHCC-2005-022, 2005.

[45] W. Lampl *et. al.*, “Calorimeter Clustering Algorithms: Description and Performance.” ATL-LARG-PUB-2008-002, 2008.

[46] S. Hassani *et. al.*, “A muon identification and reconstruction procedure for the ATLAS detector at the LHC using the MUONBOY, STACO and MuTag reconstruction packages”, *Nucl. Instrum. Meth.* **A572** (2007) 77.

[47] The ATLAS Electron Reconstruction Software, Release 12.0.6, `http://alxr.usatlas.bnl.gov/lxr-stb/source/atlas/Reconstruction/egammaRec/src/EMPIDBuilder.cxx?v=release_12_0_6`.

[48] The D0 Collaboration, “Measurement of the shape of the boson rapidity distribution for $p\bar{p} \to$ Z/gamma* $\to$ e+e- +X events produced at $\sqrt{s}$ of 1.96 TeV”, *Phys. Rev* **D76** (2007) 012003.

[49] O. Linossier and L. Poggioli, "H to ZZ* to 4 leptons channel, in ATLAS signal reconstruction and reducible backgrounds rejection." ATL-PHYS-97-101, ATL-GE-PN-101, 1997.

[50] C. Lester, M. A. Parker, and M. White, "Three body kinematic endpoints in SUSY models with non-universal Higgs masses", *JHEP* **0710** (2007) 0051.

[51] B. Allanach, C. Lester, M. Parker, and B. Webber, "Measuring sparticle masses in non-universal string inspired models at the LHC", *JHEP* **0009** (2000) 004.

[52] The ATLAS Collaboration, "ATLAS High-Level Trigger, Data Acquisition and Controls: Technical Design Report." ATLAS-TDR-016, CERN-LHCC-2003-022, 2003.

[53] A. De Santo, "Trigger strategies for SUSY searches at the LHC." `arXiv:hep-ex/0710.4161`, 2007.

[54] G.Cowan (ATLAS Statistics Forum), Private Communication.

[55] G.Polesello (ATLAS SUSY Working Group), Private Communication.

[56] L. Sonnenchein, "Analytical solution of ttbar dilepton equations", *Phys. Rev* **D73** (2006) 054015.

[57] S.Asaim, A. Gupta, N. Kanaya, Y. Kataoka, and O. Jinnouchi., "AtlfastCorrectors: Parametrizations of jet transfer function and lepton identifications for enhancement of ATLFAST I results." ATL-COM-PHYS-2008-138, 2008.

[58] A. Barr *et. al.*, "Usage of the Distributed Analysis Tools in The ATLAS Supersymmetry Working Group." ATL-SOFT-INT-2007-005, ATL-COM-SOFT-2007-011, CERN-ATL-COM-SOFT-2007-011, 2007.